Charge and Spin Wave Transport in Hybrid Magnetic Multilayers

Master's thesis

Elisabeth Meidinger

Supervisor: Prof. Dr. Rudolf Gross

Advisors: Dr. Matthias Althammer and Prof. Dr. Mathias Weiler

Garching – July 26, 2021

Technische Universität München

Walther-Meissner-Institut

Bayerische Akademie der Wissenschaften

Contents

1. Introduction

Faster, higher, stronger is not only the motto of the Olympic Games [1], a well-known slogan in the world of work [2] and the title of several books of different genres, but paraphrases also the striving for evolution in the field of technology. Researchers all over the world seek for solutions in order to process and store the steady growing quantity of information. So far, data is encoded magnetically in hard-disk drives which allows the storing of zettabytes (10^{21} bytes) of information [3]. A few years ago, the semiconductor industry finally faced the limits of Moore's Law [4]. It states that the number of transistors on a microprocessor chip doubles every two years, together with its performance. This rule is restricted by the heat accumulated in the chip circuit and by quantum effects e.g. the tunneling of electrons. Both limits become more and more important when the length scales are reduced and result in a need of alternative information processing schemes [5].

The discovery of the giant magnetoresistance [6] over three decades ago opened up the field of spintronic as a promising candidate to overcome the limits of Moore's Law. Spintronic utilizes the close relationship between charge transport and the magnetic structure and thereby, a spotlight is put onto interfaces and layered structures [7, 8]. The naming originates from the words spin and electronics and is based on the two spin channel concept proposed by Mott [9] and deals with spin dependent transport [10]. Spin angular momentum can be carried by electrons, but also spin waves enable the transport of spin information in magnetically ordered systems. The spin waves are conceptually proposed by Bloch [11] almost one hundred years ago and the quanta of spin waves, the magnons, are introduced. The related research field of magnonics aims at the realization of alternative spin wave based information technology. A promising candidate of a storage bit is a chiral spin configuration in form of a whirling spin texture, a so-called skyrmion. So far, it is anticipated to be the building block of a novel generation of non-volatile magnetic memory and logic devices with low power consumption and high storage density. The skyrmion is named after the nuclear physicist Tony Skyrme [12] who developed a model for hadrons describing particles that are stable due to their topological protection [13]. Skyrmions were first experimentally observed in 2009 in a solid state environment [14] and can behave as particles as they can be created, annihilated and moved. They are of small size and robust against external perturbations. Nanoscale magnetic skyrmions are presumably even the smallest spin textures in magnetic thin films in nature [3] and thus a perfect candidate for technical applications as an ultradense memory [15].

The chiral interaction stabilizing the skyrmion is induced by an inversion symmetry breaking, for example at interfaces of magnetic thin films. A thin film is defined as thin, when

its thickness is comparable to the width of the magnetic domain wall [16]. A configuration hosting several symmetry breakings can be realized by multilayer stacks which are composed of ultrathin magnetic layers in contact with heavy-metal thin films, allowing the formation of skyrmions even at room temperature [16, 17]. The properties of the magnetic layers can be investigated by charge and spin transport [7] and therefore, by using these techniques, we gain deeper insight into the skyrmion formation and the spin wave propagation [18].

In order to use skyrmions as storage bits, basic functions to store and process information are needed. The writing process is governed by the nucleation of individual skyrmions, the processing part means displacing, creating and annihilating them, whereas the readout is achieved by electrical detection [19]. A promising skyrmion-based storage device is a skyrmion racetrack memory. The information is encoded by a sequence of individual skyrmions in a magnetic track [20]. The decrease of the track width allows an increase of the information density [21] and the skyrmions are detected by standard tunnel magnetoresistance devices [22]. Another auspicious next generation application are skyrmion-based logic devices. These are realized by duplicating or merging skyrmions to perform basic logic operations [23].

In this thesis, we investigate hybrid magnetic multilayers by means of charge and spin wave transport in the spirit of fundamental research. These results pave the way towards low-energy consuming, high-density, non-volatile storage and logic devices of a next generation. The thesis is structured as following:

In Chapter 2, we introduce multilayers and hybrid multilayers, as well as their detailed compositions used in this thesis. Its fabrication process via optical and electron lithography is presented for the two different experimental parts of this thesis.

In Chapter 3, we investigate the charge transport inside the multilayer, focusing on two magnetoresistance effects, namely the spin Hall magnetoresistance and the anisotropic magnetoresistance in textured thin films.

It is followed up by spin wave transport experiments in Chapter 4, with an analysis of the ferromagnetic resonances and propagating spin wave resonances.

In Chapter 5, we sum up our findings and take a look beyond to possible future investigations based on the work presented in this thesis.

In the Appendix, in Sec. A.1 an overview over all fabricated and analyzed samples is given, in Sec. A.2 details on the theoretical derivation of the anisotropic magnetoresistance in textured thin films are presented. In Sec. A.3 and A.4 the fabrication schemes for samples investigated via charge and spin wave transport are listed. Finally, in Sec. A.5 the Mathematica code of the simulation of an in-plane propagating spin wave resonance in a $20\,\text{nm}$ thick $Co_{25}Fe_{75}$ ferromagnetic thin film is provided.

2. Methods

The field of nano-magnetism is based on state-of-the-art nanostructuring processes of a multitude of novel materials and their associated phenomena such as magnetoresistance effects and magnetization dynamics at the nanoscale. Magnetoresistance measurements allow studying the orientation of the magnetization in nanostructures with electrical means, providing a pathway towards spintronic applications. Magnetization dynamics can be investigated by RF techniques using e.g. ferromagnetic resonance (FMR) and reveal numerous parameters of the magnetic system, allowing to systematically investigate it. In general, nano-magnetism enables on one hand enlargement of data storage densities and on the other hand downsizing material thicknesses to only a size comparable to an atomic layer and study their magnetic properties. These ultrathin layers can be incorporated in magnetic heterostructures, which add even further functionality to the materials and can stabilize exotic magnetic phases like for instance topological spin textures (so called skyrmions) in nanostructures. A promising candidate to stabilize such topological spin textures at room temperature is a magnetic multilayer (ML), which is composed of stacks of ultrathin magnetic layers in contact with heavy-metal thin films [17]. These heterostructures develop magnetic properties different from its separate building blocks [24]. The investigation of such ML thin film heterostructures was the main part of this thesis. The specific composition of the ML structure and its fabrication process are explained in Sec. 2.1. In more detail, we first describe the sputter deposition process and the technique of optical lithography in Sec. 2.2 to pattern the ML structures. Finally, we present the obtained measurement structures suitable to either study charge or spin wave transport in Sec. 2.2.1 and 2.2.2.

2.1. Magnetic Multilayers

A presently highly investigated field of nano-magnetism deals with very small-scale structures of ultrathin films with a thickness of a few atomic layers [7]. In this thickness regime interface effects play an important role and can greatly affect the properties of these ultrathin materials. Thus ML structures with ultrathin magnetic films, adjacent to heavy-metal films, allow obtaining dramatically different magnetic properties than in bulk magnetic materials [25]. The choice of the single materials in the ML determines the magnetic properties, for example the damping or the type of interaction between the layers. In this thesis the main stack of the ML is a trilayer consisting of the heavy-metal Platinum (Pt), the itinerant ferromagnet $Co_{25}Fe_{75}$ (CoFe) and the heavy-metal Iridium (Ir). This trilayer is repeated N

times (see Fig. 2.1.1a) and leads to skyrmion formation due to the Dzyaloshinskii-Moriya-interaction. CoFe is used as the ferromagnetic material due to its beneficial damping characteristics. It approaches the low Gilbert damping regime of insulating ferromagnets with slight enhanced damping induced by additional electron-phonon-scattering events [26–28]. The trilayer is deposited onto a set of seed layers of Tantalum (Ta), Pt and Copper (Cu) on top of a Si(100)-substrate, with an $1\,\mu m$ thick thermally grown SiO_2 layer. The Ta film serves for enhanced substrate adhesion and induces a suitable crystallinity [29] whereas the Pt thin film allows stabilizing the growth of CoFe films with fcc-(111)-texture and induces an overall (111)-texturing of the ML [30]. Cu is chosen in order to reduce the damping of the ML caused by the Pt seed layer [31]. On top of the repeated trilayer, the structure is covered with a set of cap layers to prevent it from oxidation. The used materials are Ruthenium (Ru) and Ta. A further development of the ML structure is achieved by evolving it to a hybrid ML structure, as sketched in Fig. 2.1.1a. On top of the N-times repeated trilayer an additional layer of CoFe is deposited. The additionally introduced ferromagnetic layer (FM) is separated from the ML by a spacer layer. It is made of Ru allowing to adjust the static interlayer exchange coupling between ML and FM. The hybrid structure can be investigated regarding general magnetic properties and the relation to its single components ML and FM. Not only the number of repetitions of the trilayer influence the magnetic properties, but also the thickness of each ultrathin film layer. It is denoted in nm in parenthesis for the respective material and a possible stack sequence is e.g. Ta(1.5)/Pt(4)/Cu(2)/[Pt(0.75)/CoFe(1.0)/Ir(0.45)]$_7$/Ru(0.9)/CoFe(5)/Ru(2)/Ta(2). Here presented is a hybrid ML system consisting of a ML with seven repeated trilayers and a $5\,nm$ thick FM. All used sample sequences are listed in the appendix in Tab. A.1.1.

The deposition of ultrathin film layers is done by using a magnetron sputter deposition process performed by the SUPERBOWL facility at the WMI (see Fig. 2.1.1b). This technique enables coating of substrates with different materials in ultrahigh vacuum to achieve high quality thin film samples with enhanced interface cleanliness [32]. The principle of sputtering involves a controlled release of material atoms towards the substrate. In detail, positively charged ions of a gas plasma are accelerated towards a high purity target material in Argon atmosphere, causing a collision cascade inside the target and allowing the leave of secondary electrons, surface atoms and maybe even clusters of atoms. The target atoms travel towards the substrate placed face-down above the target and the target material is coating the substrate surface as a thin film. To enhance the path the incoming Argon ions can travel before they collide inside the target, the deposition pressure is typically in the low $10^{-3}\,mbar$ range. Operation at such low gas pressures leads to a reduced density of gas atoms to be ionized which equals a reduction of sputtered material. To overcome this issue, the targets are mounted inside a magnetron with an outer anode ring and a center cathode. Magnets beneath the magnetron enable trapping of electrons close to the target to enhance the probability of gas ionization [26]. The SUPERBOWL facility allows to sputter different magnetic and non-magnetic materials with very short time periods between the
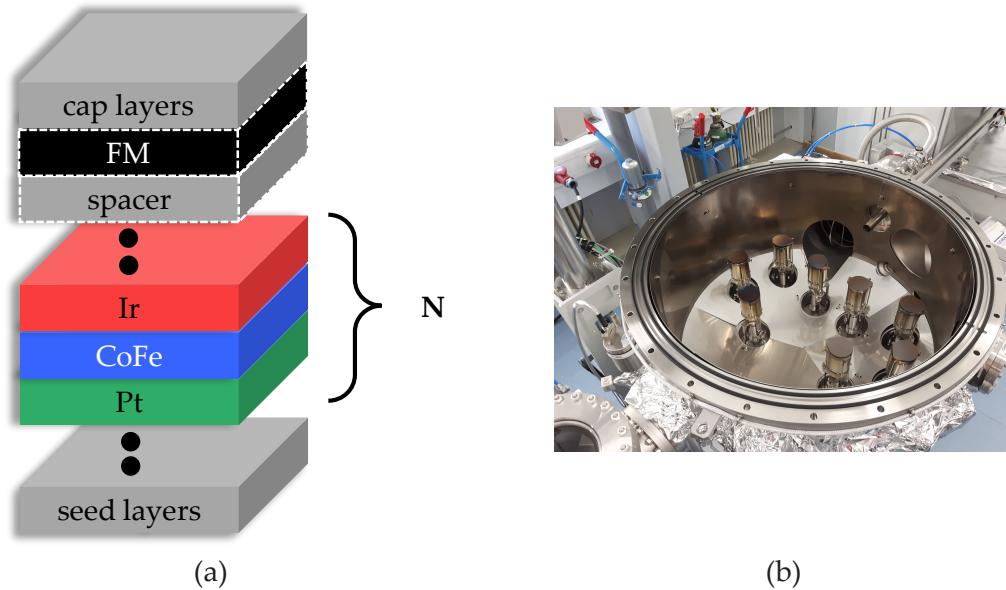
Figure 2.1.1.: ML components and fabrication (a) A sketch of a hybrid ML consisting of a ML and a FM. Dashed layers evolve a ML to a hybrid ML. N denotes the number of repetitions of the trilayer of Pt, CoFe and Ir. (b) The opened SUPERBOWL chamber with eight magnetrons. The photo is taken by M. Althammer.

different material deposition processes. This allows to prevent an oxidation of underlying recently sputtered films and to provide a large flexibility during the sputter process [32]. The thin films can be sputtered in sub-nm thicknesses determined by tuneable deposition rates.

2.2. Lithography

The sputter deposited ML and hybrid ML are the samples to be investigated regarding charge and spin wave transport. In order to apply a magnetic field, dc or ac currents and to record the induced signals, the MLs are structured into mesa structures with electrical connection possibilities. Two different sample designs are used in this thesis. Magneto-transport measurements (see chapter 3) are performed with Hall bar samples whereas spin wave propagation (see chapter 4) is investigated by spin waveguides with coplanar waveguides (CPW) antennas. Both involve structure sizes in the low µm range and therefore need techniques for precise micropatterning. The ML are patterned by either direct laser or electron beam lithography. Both techniques are described in the following.

A sketch of the laser and electron beam lithography process is given in Fig. 2.2.1. The process starts with preparing the SiO_2 substrate. In an ultra-sonic bath, Aceton and Isopropanol is used to clean the substrate. Afterwards, it is dried with nitrogen gas. As the sample is treated in surrounding air, water molecules can adsorb onto the surface of the substrate. By heating the substrate, the molecules can be desorbed. An optional adhesion

promoter is used to modify the substrate surface for optimal resist wetting and resist adhesion [33]. Using a spin coater, a homogeneous layer of positive resist is dispensed onto the substrate. Positive resist allows a direct relation between the exposed areas and the final metal structures. Remaining solvents are removed by baking the sample, in the so-called softbake process step [34]. In both, laser and electron lithography processes the respective beam "writes" the desired structures into the resist by exposing the areas of the pattern. Exposing causes a change in the chemical composition of the resist to increase the solubility when treating the sample with a developer solution. An additional baking step, the post exposure bake, can be introduced to enhance the resistance of the exposed areas against solvents in further process steps. Subsequent developing dissolves the exposed areas. The substrate is sputter deposited with different metallic thin films. The last fabrication step reveals the written structure. The so-called lift-off with Aceton removes the resist structures together with unwanted deposited thin film metals. Exposed patterns are also covered with metals but lack the underlying resist. Therefore they are not removed in the lift-off process and remain as metal structures directly on top of the substrate surface [35].
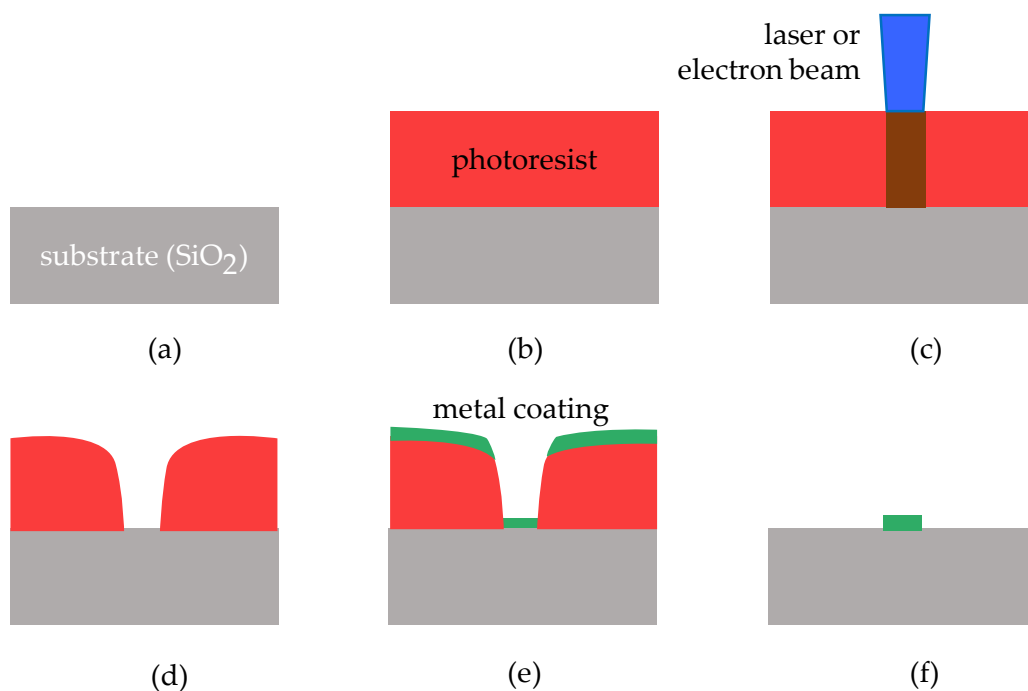
Figure 2.2.1.: Lithography process. The figure is adapted from [26]. (a) The SiO_2 substrate is cleaned and pretreated. (b) Resist is applied by spin coating and the sample is treated with heat. (c) A laser or electron beam exposes parts of the resist in order to "write" the desired structure. (d) The development shows the modification of the resist. (e) Material is deposited. (f) The lift-off dissolves the resist and reveals the fabricated metal structure.

Whether laser or electron beam lithography is chosen, depends on the smallest size of structures to write [36] and their complexity. This enhances the time efficiency of the fabrication

process. Hall bar structures with smallest parts of $1\,\mu m$ are fabricated via laser lithography. The Hall bar is written in one lithography step and the technique allows a straight-forward structure design and writing process. The CPW structures are patterned by electron beam lithography. As several writing steps are needed and structures of sizes smaller than $1\,\mu m$ have to be fabricated, this technique is favorable.

2.2.1. Charge Transport

Charge transport is investigated by samples patterned into Hall bar mesa structures via laser lithography. Only one lithography step is needed, as the whole Hall bar is consisting of the respective ML and no further metal parts are used for electrical current application or voltage detection. Several Hall bars are written on one substrate (see Fig. 2.2.2a) in case of malfunctioning of some of them. The contact pads around the horizontal ML strip are electrically connected to a chip carrier (yellow) by Aluminum wire wedge bonding. By bonding on top of the cap layer, we assume the current to flow, inter alia, inside the ML. As visible in Fig. 2.2.2b, the contact pads on the left and right of the ML allow to drive a current along the strip, whereas the contact pads either both above or below are for recording the induced longitudinal voltage differences. The ML strip is of the width $b = 30\,\mu m$ and the distance between the transverse Hall bar contacts is $l = 99\,\mu m$.

(a)   (b)   (c)
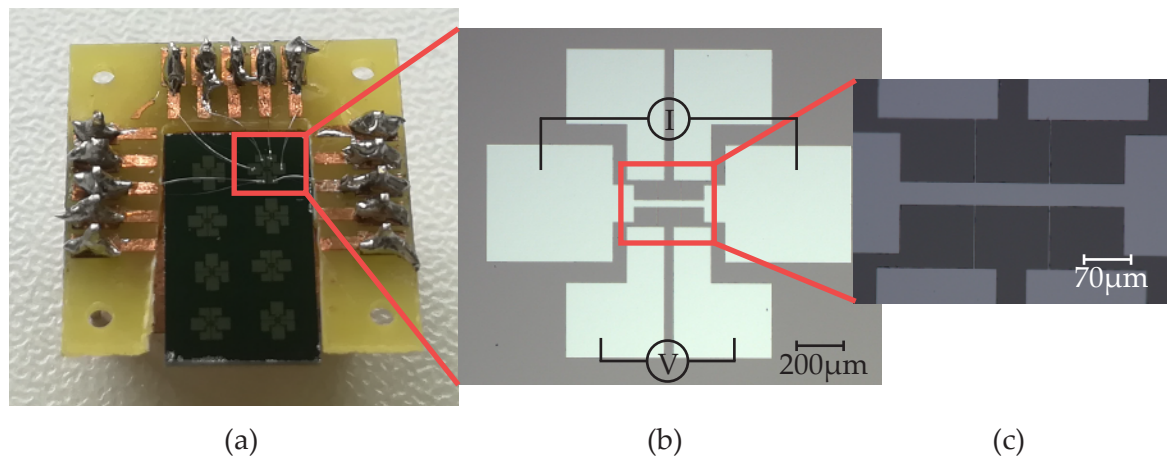
Figure 2.2.2.: Fabricated Hall bars (a) A sample with several Hall bars is glued on a chip carrier (yellow). The contact pads of a Hall bar are electrically connected to pins (silver and brown) on the chip carrier by bond wires. (b) Microscopy image of a Hall bar with a horizontal ML strip as current line (contact pads left and right). The four contact pads above and below are connected via narrow conduction lines. The longitudinal voltage is exemplary measured between the lower two contact pads. (c) A magnified microscopy image with visible fine vertical conduction lines.

The samples were measured at room temperature, but in a temperature stabilizing setup to avoid thermal drifts. The magnetic field to cause changes in the resistivity of the ML is applied via electromagnets.

2.2.2. Spin Wave Transport

The spin wave propagation is strongly dependent on the dimensions and geometry of the magnetic medium in which the spin wave travels. In the following experiments, the spin wave is propagating in a CPW structure under the restriction of full saturation of the magnetization in the ML. The choice of using waveguides relies on their favorable properties. Waveguides allow for measurements over a broad frequency range as well as a wide range of wavelengths [37]. They further enhance the transmission efficiency of the spin wave and enable defining the mainly excited wave vector of the propagating spin wave by the dimensions of the CPW antenna [38].
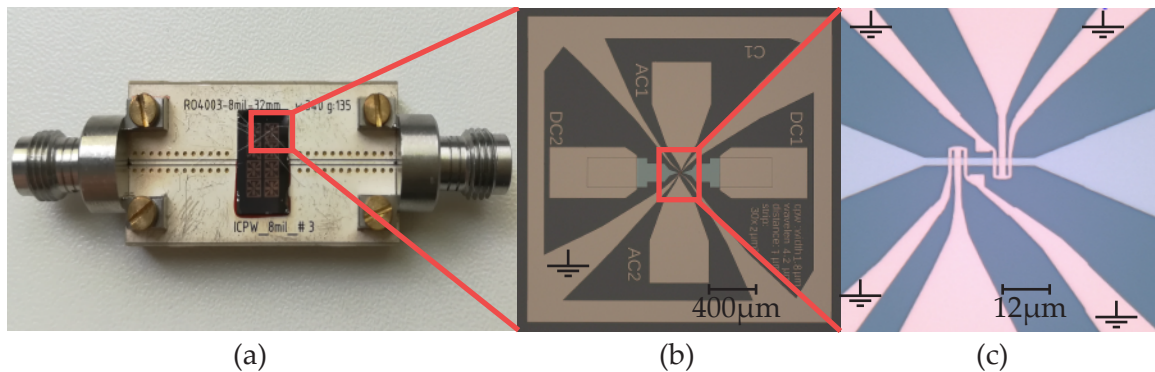

<div style="text-align:center">(a)   (b)   (c)</div>

Figure 2.2.3.: Fabricated spin wave propagation sample (a) A sample with several structures is glued onto a CPW. The antenna structure is bonded to the transmission line of the CPW and the ground. (b) A microscopy image of one structure. The horizontal (dark grey) ML strip is covered with two grounded antennas (brown). The ground is marked. (c) A magnified microscopy image of the ML strip with two antennas.

The fabrication process of these structures is more complicated than the process of the previously presented Hall bars as several individual lithography steps are taken. The first step allows to pattern the ML into a strip visible as grey horizontal line in Fig. 2.2.3b and c. The next steps place a CPW antenna structure on top of the ML allowing to electrically connect it (see brown/golden parts in Fig. 2.2.3b and c). The antenna structure is reaching from the actual antenna on top of the ML to a ground pad at the other end. The outer two parts of each antenna are connected to the ground "frame" around the written structure. Several lithographed samples are written on one substrate which is glued onto a CPW (white area around the substrate in Fig. 2.2.3a). The conduction line of the CPW is the horizontal line framed by dots (ground) in which the micro wave is propagating. The pattern design enables several types of measurements, but only an ac measurement is used in this thesis. Therefore, the contact pads above and below the $2\,\mu m$ thick ML strip are connected to the conduction line of the CPW and the outer "frame" of each structure is connected to the ground of the CPW. The conduction line of the CPW ends in the grounded center pins of the silver endlaunches (see Fig. 2.2.3a). The whole measurement setup is explained in chapter 4.1.3.

3. Charge Transport

Designing spin-dependent transport properties of magnetic materials form the basis of engineering spintronic devices as e.g. magnetic sensors and data storages [8]. Their electrical conductance mainly depends on their magnetization configuration which is expressed by the magnetoresistance effects [39] and displays the magnetotransport inside the magnet. In the following, theory on spin currents in Sec. 3.1.1 and a related magnetoresistance effect, the spin Hall magnetoresistance in Sec. 3.1.2 is given. The theory is completed by the anisotropic magnetoresistance in Sec 3.1.3. Measurements about magnetotransport begin with angle resolved investigations in Sec. 3.2 including the description of AMR in textured thin films in Sec. 3.2.1 and the parallel resistor model in Sec. 3.2.2. This magnetotransport chapter is then concluded by field resolved measurements in Sec. 3.3.

3.1. Theoretical Concepts

Magnetoresistance in general describes the behavior of the electrical resistance of a material depending on an external applied magnetic field [40, 41]. This chapter, we take a closer look at two different magnetoresistance effects, the spin Hall magnetoresistance and the anisotropic magnetoresistance. We start with a brief overview of charge and spin currents in Sec. 3.1.1, followed up by an explanation of the spin Hall effect (SHE), the spin Hall magnetoresistance (SMR) in Sec. 3.1.2 and the anisotropic magnetoresistance (AMR) in Sec. 3.1.3 as underlying principles of the presented measurements. Most importantly, we focus on the AMR in (111)-textured ferromagnetic thin films as a special case of the general AMR behavior in ferromagnetic materials.

3.1.1. Spin Currents

Mobile charge carriers in an electrical conductor possess both, a charge and an angular-momentum degree of freedom, the so-called spin. Therefore, a flow of charge carriers allows for charge current transport and spin current transport [42]. A simple model to describe both charge and spin transport, utilizes a two-spin channel model [43], accounting for two different spin orientations up ($\uparrow$) or down ($\downarrow$) of the electrons both contributing to the charge and spin transport. In this two-spin channel model, the total charge current density $\mathbf{j}_q$ is expressed by the sum of two spin-dependent contributions

$$\mathbf{j}_q = \mathbf{j}_\uparrow + \mathbf{j}_\downarrow \,. \tag{3.1}$$

Here, $\mathbf{j}_\uparrow / \mathbf{j}_\downarrow$ is the charge current density of the spin-up/-down electrons. In similar manner, the spin current density can be written in units of the reduced Planck constant $\hbar$ per unit area and per second

$$\mathbf{j}_s = \frac{\hbar}{2e}(\mathbf{j}_\uparrow - \mathbf{j}_\downarrow). \tag{3.2}$$

Referring to this model, a pure charge current bears the same number of spin-up and spin-down electrons moving in the same direction and transporting a finite amount of charge, but no spin momentum [44]. In contrast, a pure spin current is the net flow of equally numbered spin-up and spin-down electrons in opposite direction without transporting any charge [45]. Interestingly, spin currents can flow in electrical conductors via mobile charge carriers as well as in magnetically ordered materials via quantized magnetic lattice excitations [42].

An instance of the interconnection of spin transport and charge transport is the SHE effect [45] which will be addressed in the next section. It was already first described in 1971 [46] and is now an established method to create pure spin currents.

3.1.2. **Spin Hall Effect and Spin Hall Magnetoresistance**

SHE is the conversion of electrical current into a transverse spin current due to spin-dependent transverse velocities. This velocity is attained by mobile charge carriers while traversing a material with finite spin-orbit interaction (SOI). It is caused by extrinsic scattering effects and intrinsic bandstructure effects [16] and is sufficiently enhanced in heavy metals [47]. The inverse spin Hall effect (iSHE) is the reciprocal conversion from an injected spin current into a transverse electrical current. iSHE is now an common method to detect spin currents [45]. In SHE and iSHE the electric current flow $\mathbf{J}_q$, spin current flow $\mathbf{J}_s$ and spin current polarization $\boldsymbol{\sigma}$ of conduction electrons are orthogonal to each other [10]

$$\mathbf{J}_s = \alpha_{\mathrm{SH}}\left(-\frac{\hbar}{2e}\right)\mathbf{J}_q \times \boldsymbol{\sigma}. \tag{3.3}$$

The efficiency of SHE is expressed by the material specific spin Hall angle α_{SH} [48].

In detail the relevant processes in SHE can be retraced in Fig. 3.1.1a. Starting with applying a charge current density $\mathbf{j}_q$ to a normal metal (NM), the equally numbered spin-up and spin-down electrons move in the same direction along the sample. Due to spin-dependent transverse velocities, the respective type of electrons are deflected in opposite direction, creating a spin current density $\mathbf{j}_s$ transverse to the $\mathbf{j}_q$. The spin polarization $\boldsymbol{\sigma}$ is orientated perpendicular to both currents densities. In the case of an open spin current circuit boundary condition, where $\mathbf{j}_s = 0$ is met at the edges of the NM, the $\mathbf{j}_s$ results in a spin accumulation on the transverse sides of the sample, creating a gradient in the spin-dependent electrochemical potential $\boldsymbol{\mu}_s$. This gradient creates a diffusive spin current backflow compensating the via SHE induced spin current. Therefore, in a steady state configuration, there is no net transverse spin current flow. We briefly consider the opposite case of a

short-circuited boundary condition. Here the $\boldsymbol{\mu}_s = 0$ is given at the sample edges, allowing $\boldsymbol{\mu}_s$ to be shorted. This results in a $\mathbf{j}_s$ to flow through the lateral faces of the sample and the effective path of the electrons is enhanced. Taking a look at the longitudinal resistivity ρ_{long} which can be extracted here, ρ_{long} is increased in this case. The different boundary conditions result in a change in the ρ_{long}.

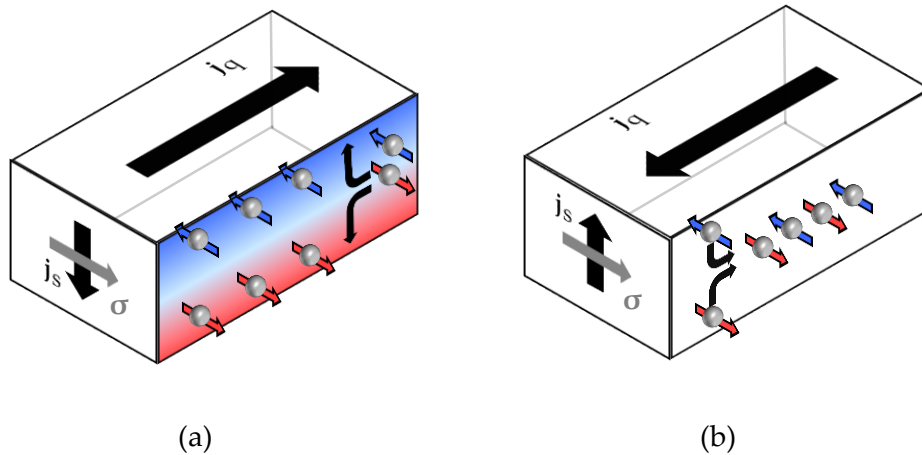(a)   (b)

Figure 3.1.1.: Sketch of SHE and iSHE inside a sample. The figure is adapted from [42]. (a) SHE: A charge current is applied along the sample. Due to spin-dependent transverse velocities, a spin current is transversely induced with a perpendicular orientated spin polarization. In steady state and open circuit configuration, spin is accumulated at the sample edges and the net transverse spin current flow vanishes. (b) iSHE: A spin current leads to a transverse charge current and a spin polarization oriented $\perp \mathbf{j}_j, \mathbf{j}_q$.

The inverse mechanism iSHE depicted in Fig. 3.1.1b, is created via an applied spin current with the same number of spin-up and spin-down electrons moving in opposite direction. The spin-dependent transverse velocities force the electrons in the same direction resulting in a charge current transverse to $\mathbf{j}_q$ and $\boldsymbol{\sigma}$.

Combining the SHE and iSHE effect allows to explain the processes taking place in SMR [45]. The involved basic principles will be addressed in the following. SMR was detected in material systems with magnetically ordered insulators adjacent to a NM. It influences the resistance of the NM depending on the orientation of the magnetic order parameter of the magnetically ordered material (MO) [42]. The heterostructure consisting of NM and MO is depicted in Fig. 3.1.2. It allows to switch gradually between the two cases of an open or closed spin current circuit boundary condition of the SHE by progressive changes of the magnetization orientation in the MO with respect to the spin polarization $\boldsymbol{\sigma}$ of the adjacent NM. Sketched in Fig. 3.1.2a, a $\mathbf{j}_q$ flowing through the NM induces $\mathbf{j}_s$ in the NM via the SHE in the direction across the NM/MO interface. $\boldsymbol{\sigma}$ is perpendicular to both flows. Directly at the interface, $\mathbf{j}_s$ exerts at torque on the magnetic order parameter of the MO [49]. The relevant interface property to determine the transport across the interface is the so-called spin mixing conductance [50]. If $\mathbf{M}$ of the MO is not parallel (noncollinear) to $\boldsymbol{\sigma}$, spin

angular momentum $\mathbf{j}_\mathrm{s}$ transfers from NM to MO. The spin current can then be absorbed by the MO.

In Fig. 3.1.2b $\mathbf{M}$ is perpendicular to $\mathbf{j}_\mathrm{q}$ and thus collinear to $\boldsymbol{\sigma}$. The spin current cannot be absorbed by the magnetization, but is reflected at the NM/MO interface and spin is accumulated. The third configuration in which $\mathbf{M}$ is pointing towards the interface can be handled in the same way as in 3.1.2a: the magnetization is noncollinear to $\boldsymbol{\sigma}$ and can absorb $\mathbf{j}_\mathrm{s}$. The absorption of spin current in general leads to a reduction of the spin accumulation at the interface, acting as additional loss channel. Consequently, the resistivity of the NM increases, whereas a reflection of $\mathbf{j}_\mathrm{s}$ at the interface results in a decrease of the resistivity. In short, this can be expressed as $\rho_{\mathbf{M}\perp\boldsymbol{\sigma}} > \rho_{\mathbf{M}\|\boldsymbol{\sigma}}$ [51].

(a) (b)
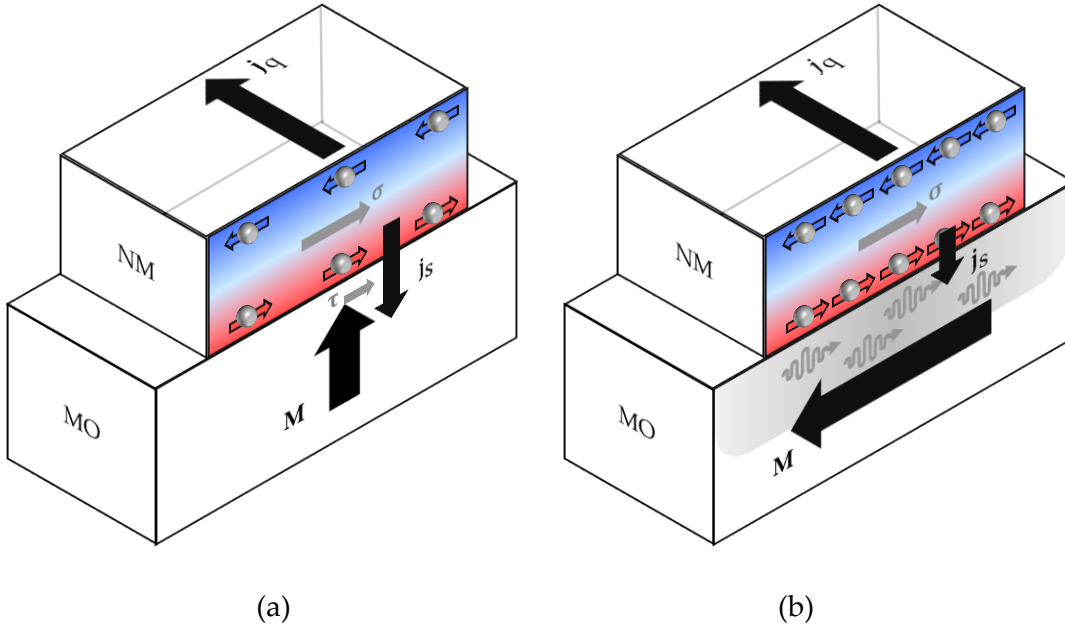
Figure 3.1.2.: Scetch of the SMR effect. The figure is adapted from [42]. (a): M is noncollinear to σ, resulting in a transfer of spin current across the interface into the MO. (b): M is collinear to σ, resulting in a spin accumulation at the interface and no transfer into the MO.

In order to quantitatively describe the SMR, one can express the longitudinal resistivity as a function of the magnetization direction of the MO [52]. The calculations are based on a spin-diffusion approximation in the NM layer in presence of SOI and quantum mechanical boundary conditions at the interface between NM and MO [45]. The SMR expression is then modulated by the magnetization direction via the spin transfer [53]. A simplified expression is given in the following

$$\rho_\mathrm{long} = \rho_0 + \rho_1\left(1 - m_\mathrm{t}^2\right), \tag{3.4}$$

with components of the magnetization orientation $\mathbf{m} = (m_\mathrm{j}, m_\mathrm{t}, m_\mathrm{n})$ denoting their projection of the magnetic order parameter onto the direction of the current $\mathbf{j}$, the transverse

direction $\mathbf{t}$ and the surface normal direction $\mathbf{n}$ [54] (see Fig. 3.2.1). Overall, $\mathbf{m}$ is related to the magnetization $\mathbf{M}$ via $\mathbf{m} = \mathbf{M}/M_{\mathrm{s}}$ [51] by means of the saturation magnetization M_{s} and we further use the relation $m_{\mathrm{j}}^2 + m_{\mathrm{t}}^2 + m_{\mathrm{n}}^2 = 1$ [55]. ρ_0 is accounting for the field in-dependent part of the resistivity, ρ_1 displays the change in modulation of the amplitude of the resistivity.

For our ML system, we employ CoFe as alternative to an insulating MO. As SMR is based on a flowing spin current through the interface controlled by the magnetization orienta-tion of the MO, the material combination with metals instead of insulating MO is equally possible to investigate SMR. As seen in further research, SMR could already be detected in weakly conducting magnetic materials [56] and metallic bilayers [57].

3.1.3. Anisotropic Magnetoresistance

SMR allows to obtain valuable information on the spin configuration inside the sample via electrical transport measurements [49]. Another equally suitable technique is to measure the AMR. Whereas the resistivity in SMR depends on the angle between $\mathbf{M}$ of the MO and $\boldsymbol{\sigma}$ in the NM, AMR in contrast is defined via the angle between the direction of the magnetization and the direction of the charge current [51]. Firstly detected by Thomson in 1857, it paved the way to several sensor technologies [58].

(a)   (b)   (c)
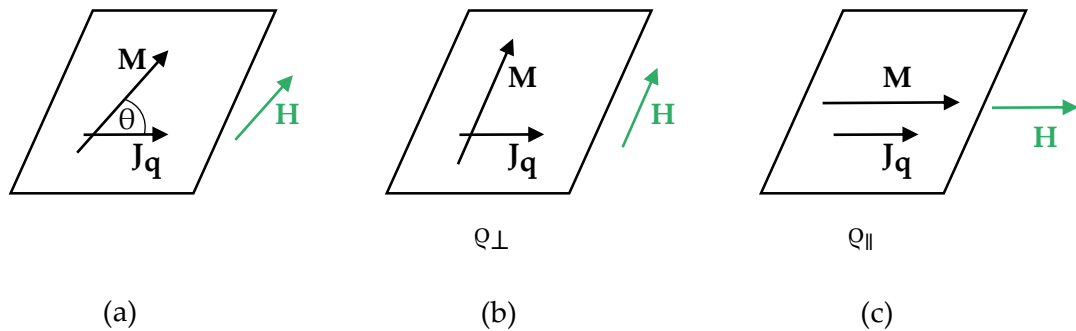
Figure 3.1.3.: AMR in a thin film (a) Arbitrary angle between the current direction and the mag-netization direction defined by the angle θ (b) perpendicular resistivity configura-tion (c) parallel resistivity configuration.

AMR describes the longitudinal electric resistivity of magnetically ordered materials de-pending on the magnetization direction with respect to the direction of the electrical cur-rent. It arises from spin-orbit interaction and can phenomenologically be described by a resistivity tensor for homogeneously magnetized materials. The tensor is a function of the magnetization and current direction relative to crystallographic axes [39]. A possible resistivity tensor [59] can be formulated using the transverse and longitudinal electrical resistivities $\rho_\perp$ and $\rho_\parallel$ for current directions perpendicular or parallel to the magnetization (see Fig. 3.1.3b and c) [60] with symmetry restrictions according to literature [61]. Under the assumption of magnetization in z-direction (see tensor structure) and using the resis-

tivity ρ_{H} representing the contribution from AMR in transversal direction, the resistivity tensor results in:

$$\rho_{ij} = \begin{pmatrix} \rho_\perp & \rho_{\mathrm{H}} & 0 \\ -\rho_{\mathrm{H}} & \rho_\perp & 0 \\ 0 & 0 & \rho_\parallel \end{pmatrix}. \tag{3.5}$$

For arbitrary orientations of the magnetization to the current direction, we introduce the angle θ between the current direction $\mathbf{J}$ and the direction of the magnetization $\mathbf{m}$ according to Fig. 3.1.3a. Using the resistivity tensor (3.5) and the relation between the electrical field strength $\mathbf{E}$ and ρ by Ohm's law, we obtain an expression for the resistivity as function of θ. It is reformulated due to convenient use in further calculations.

$$\begin{aligned} \rho &= \frac{\mathbf{E} \circ \mathbf{J}}{J^2} = \rho_\perp + (\rho_\parallel - \rho_\perp) \cos^2(\theta) \\ &= \frac{\rho_\parallel + 2\rho_\perp}{3} + (\rho_\parallel - \rho_\perp)\left(\cos^2(\theta) - \frac{1}{3}\right). \end{aligned} \tag{3.6}$$

Introducing the abbreviations of the average resistivity $\bar{\rho} = \frac{2}{3}\rho_\perp + \frac{1}{3}\rho_\parallel$ and the spontaneous resistance anisotropy $\Delta\rho = \rho_\parallel - \rho_\perp$ allows to formulate the AMR ratio.

$$AMR \equiv \frac{\rho - \bar{\rho}}{\bar{\rho}} = \frac{\Delta\rho}{\bar{\rho}}\left(\cos^2(\theta) - \frac{1}{3}\right). \tag{3.7}$$

The AMR ratio is the difference of the resistivity in saturation to the averaged value normalized to it [58]. The AMR shows a clear $\cos^2$-dependence.

In the following, we want to focus on AMR traces in (111)-textured thin films [62] which are assumed to be present in our samples due to the Pt thin film layers. The theory on describing this effect is rather lengthy and will be addressed in more detail in appendix A.2. The longitudinal resistivity can be expressed as follows:

$$\rho_{\mathrm{long}} = \rho_0 + \rho_1 m_{\mathrm{j}}^2 + \rho_2 m_{\mathrm{n}}^2 + \rho_3 m_{\mathrm{n}}^4 + \rho_4 m_{\mathrm{n}}^2 m_{\mathrm{j}}^2. \tag{3.8}$$

Depending on the geometry in which we are measuring, terms of Eq. (3.8) either vanish or persist, thus determining the resistivity behavior. The geometries are explained in the following chapter.

3.2. Angle Resolved Measurements

The characterization of SMR and AMR in our MLs is done by investigating the longitudinal resistivity of our samples. This value can be extracted from the measured longitudinal voltage V_{long} by use of the dimensions of our Hall bar sample structure (see chapter 2.2.1)

$$\rho_{\mathrm{long}} = \frac{V_{\mathrm{long}}}{I}\frac{b}{l}d, \tag{3.9}$$

using the parameters of the width of the center stripe b, the distance between the contacts l, the sample film thickness d and the applied dc current I along the Hall bar.

To study effects of SMR and AMR in our samples, we measure the magnetoresistance as a function of the magnetization orientation. In these so-called angle dependent magnetoresistance (ADMR) experiments, we determine the longitudinal resistivity (one can also record the transversal) while rotating the externally applied magnetic field $\mathbf{h} = \mathbf{H}/H$ at a fixed field amplitude H within three orthogonal rotation planes [49]. The magnetic field magnitude is sufficiently large to fully saturate the sample and its magnetization is thus always aligned parallel to the external magnetic field. Both, SMR and AMR have a characteristic behavior depending on the measurement geometry and can thus be extracted from the measured data. The geometries illustrated in Fig. 3.2.1 can be distinguished from each other by the plane in which the magnetic field is rotating. The planes are spanned by vectors pointing along characteristic directions of the Hall bar. This introduces a Cartesian coordinate system which is applicable onto our structures. The vectors are the unit vectors of the current direction $\mathbf{j}$ along the Hall bar, the surface normal $\mathbf{n}$ pointing out-of-plane (OOP) to the sample surface and the transverse direction $\mathbf{t} = \mathbf{n} \times \mathbf{j}$ across the Hall bar [51, 55]. The angle to characterize each measurement geometry classifies the plane, in which the field is rotating and are called α, β or γ for the respective geometries in-plane (IP), OOPJ and OOPT. α is allowing to rotate the field in the $\mathbf{n}$-$\mathbf{t}$-plane, IP to the sample. In OOPJ, β rotates the magnetic field in the $\mathbf{j}$-$\mathbf{t}$-plane. In OOPT, the external magnetic field is rotated by the angle γ in the $\mathbf{j}$-$\mathbf{n}$-plane.
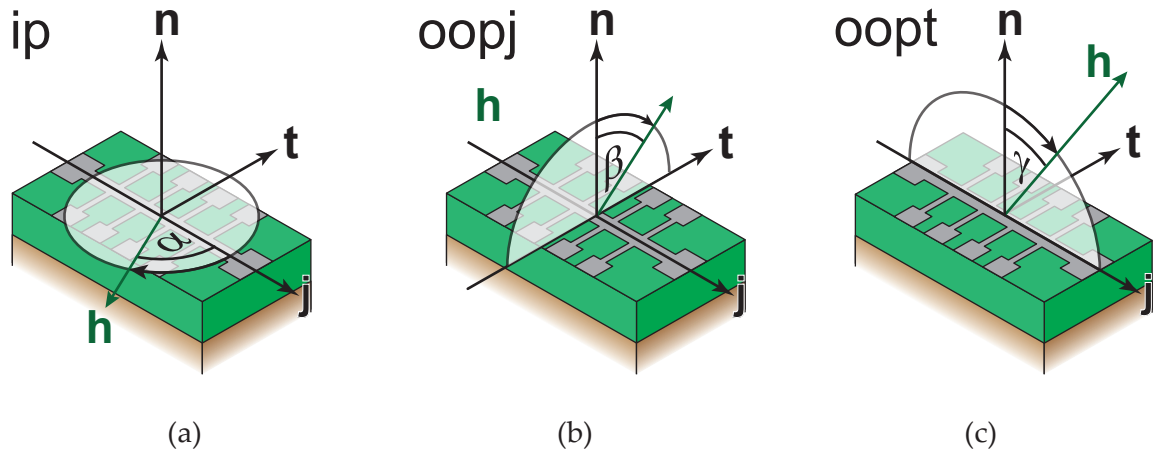

Figure 3.2.1.: Sketch of the rotation planes in the geometry (a) IP (b) OOPJ and (c) OOPT. The figure is taken from [42].

Having introduced the measurement geometries, the longitudinal resistivity modulations due to SMR given by Eq. (3.4) can be expressed:

$$\rho_{\text{long}}^{\text{SMR,IP}} = \rho_0^{\text{SMR}} + \rho_1^{\text{SMR}} \cos^2(\alpha) \,, \tag{3.10}$$

$$\rho_{\text{long}}^{\text{SMR,OOPJ}} = \rho_0^{\text{SMR}} + \rho_1^{\text{SMR}} \cos^2(\beta) , \tag{3.11}$$

$$\rho_{\text{long}}^{\text{SMR,OOPT}} = \rho_0^{\text{SMR}} + \rho_1^{\text{SMR}} . \tag{3.12}$$

In the same way, the longitudinal resistivities for AMR in (111)-textured thin films can be expressed for the respective field rotation by the use of (**??**) (in detail see appendix A.2)

$$\rho_{\text{long}}^{\text{AMR,IP}} = \rho_0^{\text{AMR}} + \rho_1^{\text{AMR}} \cos^2(\alpha) , \tag{3.13}$$

$$\rho_{\text{long}}^{\text{AMR,OOPJ}} = \rho_0^{\text{AMR}} + \rho_2^{\text{AMR}} \cos^2(\beta) + \rho_3^{\text{AMR}} \cos^4(\beta) , \tag{3.14}$$

$$\rho_{\text{long}}^{\text{AMR,OOPT}} = \rho_0^{\text{AMR}} + \rho_1^{\text{AMR}} \sin^2(\gamma) + \rho_2^{\text{AMR}} \cos^2(\gamma)$$
$$+ \rho_3^{\text{AMR}} \cos^4(\gamma) + \rho_4^{\text{AMR}} \cos^2(\gamma) \sin^2(\gamma) . \tag{3.15}$$

These equations allow to investigate SMR and AMR in (111)-textured thin films in our measured longitudinal resistivities. In IP configuration, SMR shows a $\cos^2$-behavior with maximal signal for magnetization orientations parallel to the direction of the current. AMR also shows a $180°$-symmetry but depending on the sign of ρ_1^{AMR}, a $\cos^2$-like or $\sin^2$-like behavior of the resistivity is given. In the first case, SMR and AMR are thus not discernible from each other in IP, in the second case, we can identify the respective magnetoresistance effect. In OOPJ configuration, SMR has a $\cos^2$-modulation of the resistivity with maximal signal for the magnetization parallel to the surface normal. AMR shows the same trace, but introduces a broadening of the maximal or minimal resistivity due to an additional $\cos^4$-term. In OOPT geometry, SMR exhibits a constant behavior as a function of the magnetic field orientation. In contrast, the AMR displays an angle dependence up to $\cos^4$ and also depending on the ratios between ρ_0^{AMR}, ρ_1^{AMR}, ρ_2^{AMR}, ρ_3^{AMR} and ρ_4^{AMR} a $90°$-symmetry due to the contribution of ρ_4. In summary, the SMR is completely included in the description of the AMR in (111) textured thin films. It is very likely, that both effects contribute to the magnetoresistance in our ML samples, but a separation of both effects by the rotational geometry and associated symmetry of the magnetoresistance is no longer possible, as compared to the magnetoresistance in yttrium iron garnet/Pt bilayers [45, 51].

3.2.1. Experimental Results

We are presenting angle dependent magnetoresistance data of a hybrid ML Ta(1.5)/Pt(4)/ Cu(2)/[Pt(0.75)/CoFe(1.0)/Ir(0.45)]$_7$/Ru(0.9)/CoFe(5)/Ru(2)/Ta(2) and its two separate parts, the ML Ta(1.5)/Pt(4)/Cu(2)/[Pt(0.75)/CoFe(1.0)/Ir(0.45)]$_7$/Ru(0.9)/Ta(2) and the FM Ta(1.5)/ Pt(4)/Cu(2)/Ru(0.9)/CoFe(5)/Ru(2)/Ta(2). During the ADMR measurement, the temperature is stabilized to avoid thermal drifts. The measurement procedure includes the recording of the longitudinal voltage V_{long} while applying a dc current of $500\,\mu\text{A}$ and a current-reversal method [63] to minimize thermal fluctuations and reduce noise. As previously discussed, a sufficiently high magnetic field is applied to fully saturate the hybrid ML and especially the FM. This allows for the assumption that the magnetization
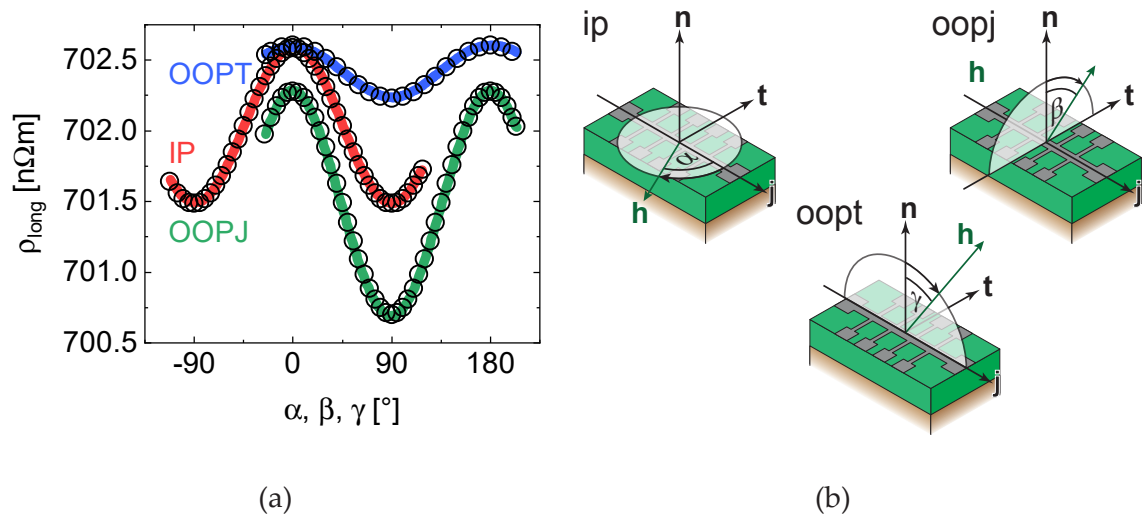
(a)   (b)

Figure 3.2.2.: Longitudinal resistivity of the ML (a) Longitudinal resistivity with respect to the
direction of the applied field. The behavior is fitted by a $\cos^2$ of the respective
angle (black circles). (b) ADMR rotation planes, adapted from [42].

is always aligned parallel to the externally applied magnetic field during the measure-
ment. For the hybrid ML and the FM a constant magnetic field of $3.5\,\mathrm{T}$ is applied during
the angle dependent measurement, for the ML a field of $1\,\mathrm{T}$ is sufficient to saturate the
magnetization.

The recorded data of the ML is depicted in Fig. 3.2.2. The angle dependent ρ_{long} is plot-
ted for the IP (red), OOPJ (green) and OOPT (blue) rotation plane. In all three rotation
planes, ρ_{long} exhibits a dependence on the magnetic field orientation. We also observe a
shift in the absolute angle independent value of the resistivity in every measuring geom-
etry, which we attribute to the sample remounting for each measurement geometry and
thus slight changes in the actual sample temperature. We take a look at the longitudinal re-
sistivity modulation by fitting the data to a $\cos^2$-trace of the respective characteristic angle
in order to prove the basic agreement with SMR and AMR signals (see exemplary in 3.2.2).
The respective fitting parameters describing the modulation amplitude are approximately
for the hybrid ML $\rho_{IP} = 0.74\,\mathrm{n\Omega\,m}$, $\rho_{OOPJ} = 0.68\,\mathrm{n\Omega\,m}$, $\rho_{OOPT} = -0.08\,\mathrm{n\Omega\,m}$, for the ML
$\rho_{IP} = 1.10\,\mathrm{n\Omega\,m}$, $\rho_{OOPJ} = 1.58\,\mathrm{n\Omega\,m}$, $\rho_{OOPT} = 0.38\,\mathrm{n\Omega\,m}$ and for the FM $\rho_{IP} = 0.95\,\mathrm{n\Omega\,m}$,
$\rho_{OOPJ} = 0.45\,\mathrm{n\Omega\,m}$, $\rho_{OOPT} = -0.51\,\mathrm{n\Omega\,m}$.

In all three measurement geometries, the ML shows a $180°$-symmetry with respect to the
field angle in Fig. 3.2.2. The data can be nicely reproduced with a $\cos^2$-fit indicated as
black circles. We here assume that SMR as well as AMR can contribute to the observed
magnetoresistance. For the SMR effect we expect to observe an angle dependence only in
the IP and OOPJ rotation planes (see Eq. (3.10) and (3.11)), with a $\cos^2$-dependence, and
a constant resistivity for the OOPT rotation plane (see Eq. (3.12)). In case of the AMR in
(111)-textured thin films, we expect to observe an angle dependence in all three orthog-
onal rotation planes (see Eq. (3.13), (3.14) and (3.15)) and in leading order, we receive

a $\cos^2$-dependence. Depending on the value of the prefactors ρ_i^{AMR}, in OOPT different 180°-symmetries may be obtained. In more detail and starting in the IP configuration, the 180°-symmetry with a maximum at 0° is predicted from both, SMR and AMR theory and can therefore not be used to separate these two contributions. Similarly, the OOPJ measurements with a maximum at 0° can be explained via the SMR as well as the AMR in (111)-textured thin films. In case of the AMR, higher order contributions seem to be reduced in magnitude. The last measurement geometry reveals also a 180°-symmetry with maximal signal at 0°. As the SMR reveals no modulation in this geometry, the change in resistivity can only be explained by the AMR effect with a dominant ρ_2^{AMR} contribution. It is important to emphasize that the amplitude of the $\cos^2$ angle dependence is the smallest in the OOPT rotation plane. This supports our assumption that $\rho_1^{\mathrm{AMR}}, \rho_2^{\mathrm{AMR}} > 0$. However, it is impossible to utilize the three orthogonal rotation planes to separate the SMR and AMR contributions, as the AMR for a (111)-texture exhibits an angle dependence in all three rotation planes. To check this conjecture one can utilize the amplitudes extracted from the $\cos^2$ fit and finds the amplitude in IP is equal to the amplitude in the OOPJ rotation plane minus the amplitude in the OOPT rotation plane.

As a next step, we look into the magnetoresistance of the FM sample. The ADMR is depicted in Fig. 3.2.3b and can be explained in the same way as for the ML sample. It reveals both, SMR and AMR dependencies in IP and OOPJ configuration. In OOPT geometry the 180°-symmetry is inverted to a maximum at 90° which is once again governed by the AMR in OOPT direction. The modulation amplitudes in IP can also be composed out of the ones of the OOPJ and OOPT geometry.

The hybrid ML (in Fig. 3.2.3c) shows the traces from SMR and AMR in IP and OOPJ and reveals clearly the special AMR type in OOPT with a 90°-symmetry, which can only be explained by the ρ_4^{AMR} term as discussed further below. The modulation amplitudes can be understood in the same way as explained for the FM sample.

In summary, the resistivity behavior from ADMR measurements in our sample can only be modeled by including the AMR description for (111)-textured ferromagnetic thin films. A separation of this AMR and the SMR is not possible by just using the ADMR measurements. The observed angle dependence nevertheless is consistent within three orthogonal rotation planes and fully compatible with AMR and SMR.

To further support the conjecture that the observed ADMR response in our samples can be solely explained by the AMR contribution, we now employ the full equations (3.13), (3.14) and (3.15) of the AMR in (111)-textured ferromagnetic thin films to quantitatively describe the results of the ML, FM and hybrid ML. In Fig. 3.2.3 the resistivity behavior of all three sample types with respect to the rotation geometry is shown. The data is fitted to the respective AMR behavior of Eq. (3.13), (3.14) and (3.15) for each orthogonal rotation plane. In our fits, we only allow ρ_0^{AMR} to change for each rotation plane due to the necessary remounting of the sample, while the values of the remaining ρ_i^{AMR} parameters are identical
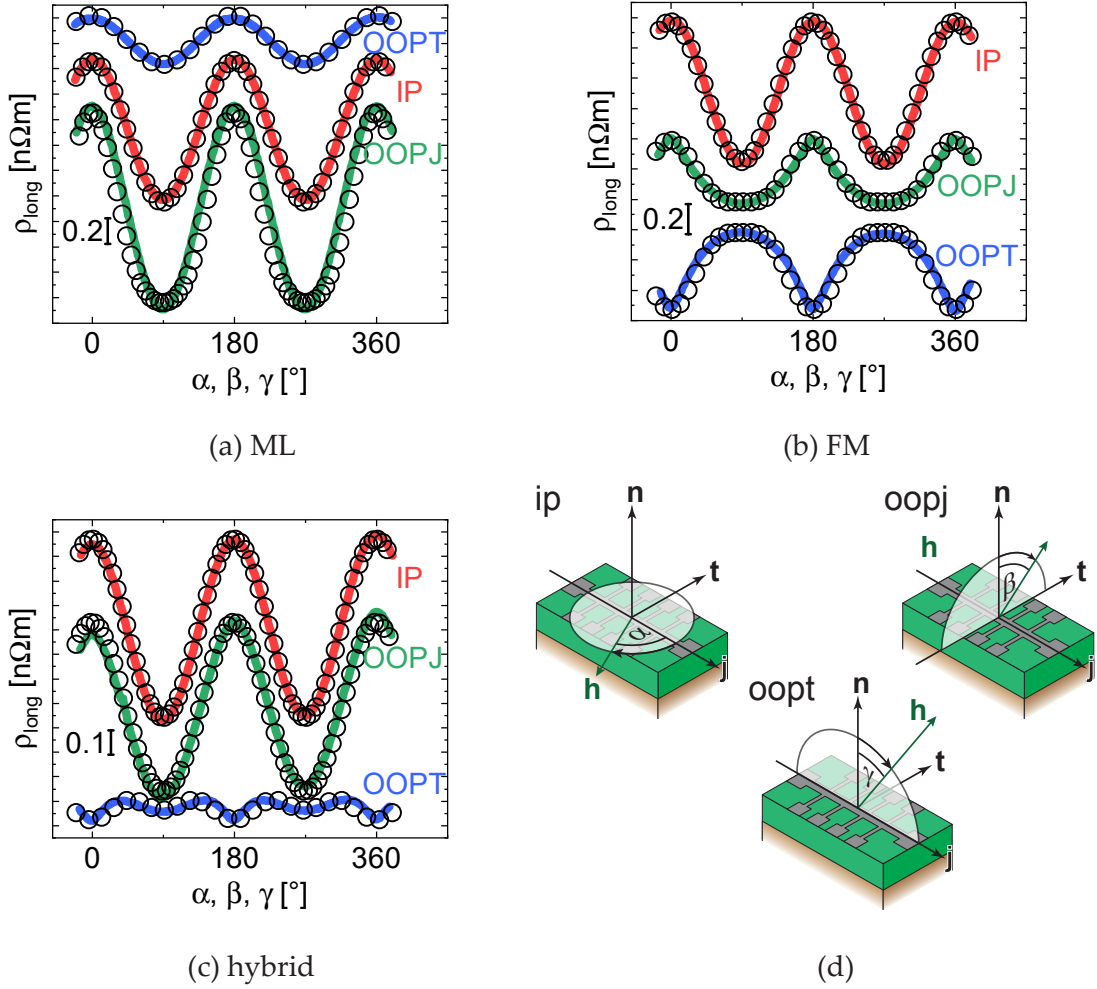
(a) ML

(b) FM

(c) hybrid

(d)

Figure 3.2.3.: Longitudinal resistivity fitted to the theory of an AMR in (111)-textured thin films (fit denoted as black circles). All fit parameters except ρ_0^{AMR} are identical for all three rotation planes. The resistivity is shifted vertically by the respective ρ_0^{AMR} for better visibility (a) ρ_{long} of the ML measured at $1\,\mathrm{T}$. (b) ρ_{long} of the FM measured at $3.5\,\mathrm{T}$. (c) ρ_{long} of the hybrid ML measured at $3.5\,\mathrm{T}$. (d) A scetch of the ADMR planes, the figure is adapted from [42].

for all three rotation planes. The results of this fit procedure are given in Tab. 3.2.1 for our three samples. We note that the curves are shifted by the fit parameter ρ_0^{AMR} for better visibility, in detail the ML resistivity by $\rho_0^{\mathrm{AMR}} = 701.12\,\mathrm{n\Omega\,m}$, the FM by $\rho_0^{\mathrm{AMR}} = 412.06\,\mathrm{n\Omega\,m}$ and the hybrid ML by $\rho_0^{\mathrm{AMR}} = 399.23\,\mathrm{n\Omega\,m}$.

Starting with the measured resistivities depicted in Fig. 3.2.3a, we can clearly distinguish, that the resistivity of the ML can be very well described via the AMR in (111)-textured thin films. However, as previously discussed, the ADMR measurements can be also well explained by the combined action of SMR and polycrystalline AMR, such that the use of the AMR model for (111)-textured ferromagnetic films is not justified. In contrast, the data of the FM and hybrid ML are perfectly described by the fit. Most importantly, they require additional ρ_i^{AMR} parameters only valid in the limit of (111)-texture to correctly describe the

modulation amplitude [nΩ m]	hybrid ML	ML	FM
ρ_1^{AMR}	0.73±0.00	1.11±0.01	0.92±0.02
ρ_2^{AMR}	0.59±0.01	0.50±0.01	0.00±0.02
ρ_3^{AMR}	0.10±0.02	1.00±0.01	0.41±0.02
ρ_4^{AMR}	0.34±0.01	1.00±0.00	0.89±0.02

Table 3.2.1.: Resistivity prefactors of Eq. (3.13), (3.14) and (3.15) with uncertainties. They prove the existence of the AMR in (111)-textured thin films in the hybrid ML, ML and FM.

ADMR behavior. The FM reveals this by broader modulations than a simple $\cos^2$-behavior originating from the ρ_2^{AMR} parameter which is visible in the decrease of this parameter value in Tab. 3.2.1. The hybrid ML needs a 90°-symmetry description in OOPT, which is caused by the ρ_4^{AMR} contribution.

Looking closer at the FM, in OOPJ and OOPT direction the maxima and minima at 90° and 270° are broader whereas the minimas and maximas at 0°, 180° and 360° are sharper. Comparing it to the rotational geometries sketched in Fig. 3.2.3d, at $\beta = 90°$ and $\gamma = 90°$ the magnetization is aligned IP to the film in contrast to an OOP alignment at 0°. This effect becomes less pronounced with increasing magnetic field and disappears approximately above an externally applied magnetic field of 5 T. The behavior for small magnetic fields underlines the IP easy-plane anisotropy character of CoFe [64] and indicates, that the applied field of 3.5 T was not enough to fully saturate the magnetization along the OOP direction. Using the value of the saturation magnetization of CoFe, one obtains for the thin film shape anisotropy a saturation field of 5 T, which is larger as the applied field of 3.5 T. The sharpening of minima and maxima at fields smaller than 5 T is also visible in a hybrid ML with a FM of a layer thickness of 20 nm compared to the currently investigated hybrid ML with 5 nm CoFe. In contrast, for the presented hybrid ML, the influence of the ML itself is comparable to the FM and therefore the trace of the IP anisotropy is suppressed. Consequently, the minima or maxima of the resistivity are not broadened. The exact values of the ρ_i^{AMR} parameters sensitively depend on the strength of the (111)-texturing. Especially, this texturing is different in the hybrid ML and the FM as in the first case, the thick CoFe layer is deposited onto the ML and in the second case, CoFe is deposited onto the seed layer. Additionally, this AMR behavior is assumed to be thickness dependent [62] and both CoFe-contributions, in the hybrid ML and the FM are of a few nm and thus in the region to be strongly influenced by interface scattering (scaling as $1/d$). Since a clear separation of the interface scattering effects and the AMR from a (111)-texture requires a systematic investigation of the thickness dependence, we refrain from comparing the extracted ρ_i^{AMR} parameters for each sample. Nevertheless, only this AMR description allows to understand the behavior of the hybrid ML in OOPT and the respective fits in OOPJ and OOPT rotation planes model the measured resistivities of the FM more precise than the one of the conventional AMR description. The fit is developed to the fourth order, as it already allows to model the data accurately. An expression up to second order is not sufficient and

higher orders need to be investigated to increase the precision of the fit. This is in contrast to present literature, as in [65] no ρ_4^{ARM}-term is included, which is definitely needed to model our data. In summary, the AMR(111)-model is sufficient to describe the resistivity behavior, nevertheless contributions from the SMR effect cannot be excluded.

This difficulty in separating between the two magnetoresistance effects has already been discussed in several other studies. One possibility to further disentangle between the two, apart from angle dependent measurements, is by investigating the sample at different temperatures [66]. As already reported for yttrium iron garnet/platinum heterostructures, a decrease in temperature results in a smaller SMR amplitude in general [67] whereas the conventional AMR effect amplitudes increase. A dominance in the respective temperature regimes can therefore allow to separate between SMR and conventional AMR. This might allow to draw conclusions also on the special AMR effect and the relation between SMR and AMR. Overall, for this material heterostructure further investigations are required.

3.2.2. Parallel Resistor Model

So far, we can relate the resistivity in each system FM, ML and hybrid ML to magnetoresistance effects. In order to explain the interplay between FM and ML in the hybrid ML, we introduce a parallel resistor model which describes the resistance of the hybrid ML as composition of a parallel circuit comprising of the resistance of the ML and the resistance of the FM

$$R_{\mathrm{hybrid}} = \left(\frac{1}{R_{\mathrm{ML}}} + \frac{1}{R_{\mathrm{FM}}} \right)^{-1} . \tag{3.16}$$

This model is applied on each measurement configuration IP, OOPJ and OOPT. The values of the inverse resistance $\frac{1}{R_{\mathrm{hybrid}}}$ are well deducible by adding up the values of the inverse resistance of the ML $\frac{1}{R_{\mathrm{ML}}}$ and the FM $\frac{1}{R_{\mathrm{FM}}}$. We obtain the exact values of the inverse resistance by deriving R from the resistivity ρ divided by the sample thickness d, since the geometry of the Hall bar is identical for all samples and only the total thickness of each layer is changing. To avoid to account twice for certain layers in the hybrid ML, we correct the sample thickness of the ML by subtracting the seed and cap layer thicknesses. Additionally, we assume the resitivity of the seed layer to be dominated by the resistivity of the $4\,\mathrm{nm}$ thick Pt layer. We also have to take into account that for the ML the field rotations were measured at $1\,\mathrm{T}$ as compared to the FM and hybrid ML measured at $3.5\,\mathrm{T}$. Taking a look at field resolved measurements of the ML we still see a small field dependence at fields above $1\,\mathrm{T}$ and we can assume the amplitudes in angle dependent measurements to be larger at $3.5\,\mathrm{T}$ compared to the actually measured $1\,\mathrm{T}$. But nevertheless, this deviations are less than $1\,\%$ and the values of the inverse resistances can be very well modeled with the parallel resistor concept.

We can also analyze the fractions of the inverse resistance of the FM or the ML compared

to the inverse resistance of the hybrid ML $\xi_i = \frac{\frac{1}{R_i}}{\frac{1}{R_{\text{hybrid}}}}$ for $i = \text{ML}, \text{FM}$. ξ_{ML} and ξ_{FM} are almost equal which allows to assume an equal contribution from ML and FM to the hybrid ML concerning magnetoresistance effects.
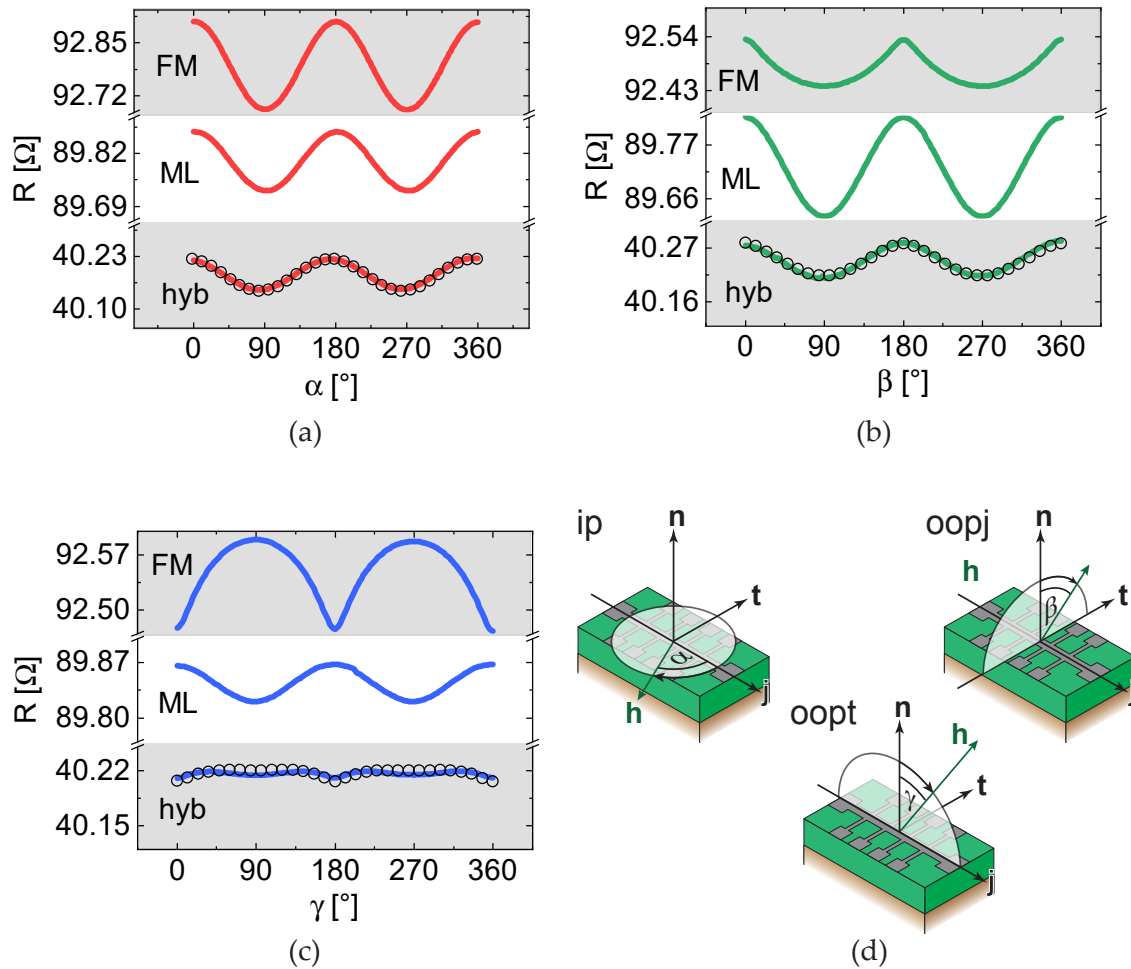

Figure 3.2.4.: Resistance R of FM, ML and hybrid ML marked on left side of respective graph. The resistance calculated via the (corrected) parallel resistor model is indicated as black circles at the resistance of the hybrid ML. (a) IP (b) OOPJ (c) OOPT (d) field rotation planes, figure adapted from [42].

A quantitative analysis is presented in the following, proving that the resistance behavior in the hybrid ML is indeed the sum of the ML and the FM. In Fig. 3.2.4 the resistance R of each sample in IP, OOPJ or OOPJ is depicted. Also the resistance calculated via the parallel resistor model and corrected by the thickness of the seed layer is indicated in Fig. 3.2.4 as black circles. As visible, the derived resistance is very well comparable to the measured resistance. In detail, in IP, the resistance with respect to the field angle α of the FM and ML show a $\cos^2(\alpha)$ signal. The sum of both signals has the same maximum and minimum

behavior which is visible in the resistance of the hybrid ML in IP. The smaller amplitude of the hybrid ML is well explained by the parallel resistor network. The exact values are well understood by Eq. (3.16) and indicated in Fig. 3.2.4 as black circles for the hybrid ML. In OOPJ, the $\cos^2(\beta)$ of the ML and the FM is imprinted to the hybrid ML and the amplitude development is also explained by the parallel resistor model. In OOPT, the model allows to understand the small 90°-symmetry of the hybrid ML. When adding the $\sin^2(\gamma)$ resistance of the FM to the $\cos^2(\gamma)$ signal of the ML, the modulation in the hybrid ML is nearly canceled. The slight existing modulation is deducible by comparison of the amplitudes of the FM and ML. The FM with its larger amplitude determines the overall modulation but the ML reduces the signal at its maxima. The cancelling out of the modulation is additionally explained by the model in Eq. (3.16) and visible in Fig. 3.2.4. Overall, the hybrid ML system can be very well understood being composed out of ML and FM and the parallel resistor model allows to prove this quantitatively by comparing the resistances of the three samples in Fig. 3.2.4 and qualitatively by using Eq. (3.16).

Finally, we employed ADMR measurements to check for a possible static coupling between the FM and the ML in our hybrid MLs. To this end, we fabricated an additional sample with a thicker spacer layer of $5\,\mathrm{nm}$ Ru between ML and FM as compared to the just presented hybrid ML with $0.9\,\mathrm{nm}$ Ru spacer layer. The other deposition parameters are kept the same. A thickness increase of the spacer layer should change the influence of the Ruderman-Kittel-Kasuya-Yosida (RKKY) interaction and thus reveal a static interlayer exchange coupling between FM and ML. This indirect interaction is mediated by conduction electrons and is dependent on the distance between the localized magnetic moments [68]. By analyzing the angle dependent measurements for both samples, no difference in resistivity amplitudes or modulation is visible. Thus we can exclude an influence of a static coupling. In Chapter 4 the dynamical coupling between ML and FM is investigated using propagating spin waves.

3.3. Field Resolved Measurements

Apart from investigating magnetoresistance effects depending on the field orientation, we can also investigate the magnetic field dependence of the resistance by changing the magnitude of the externally applied magnetic field. The results of a hybrid ML with stack sequence Ta(1.5)/Pt(4)/Cu(2)/[Pt(0.5)/CoFe(1.17)/Ir(0.7)]$_6$/Ru(5)/CoFe(20)/Ru(2)/Ta(2) are depicted in Fig. 3.3.1a. This sample is a hybrid ML with six repetitions of the trilayer and a FM layer of $20\,\mathrm{nm}$ thickness. The measurements are once again conducted in a temperature stabilized environment and the field is changed up to $|3.5\,\mathrm{T}|$ to fully saturate the sample at the beginning of the measurement. Thus we can assume for large magnetic field values that the magnetization of the sample is aligned parallel to the externally applied magnetic field. The magnetic field sweeps were carried out for three orthogonal orienta-

tions of the external magnetic field along the current direction (along **j**), OOP of the sample (along **n**) and transverse to the current direction in the film plane (along **t**) (see Fig. 3.2.1 for the definition of these directions for our Hall bar geometry). We record the longitudinal voltage as a function of the applied magnetic field magnitude and calculate the respective resistivities via Eq. (3.9). For the determination of the effective magnetoresistance MR we use the following scheme. MR is calculated by referencing the longitudinal resistivity depending on the applied magnetic field to the longitudinal resistivity at maximum field

$$MR = \frac{\rho_{\text{long}}(H) - \rho_{\text{long}}(H_{\text{max}})}{\rho_{\text{long}}(H_{\text{max}})} \, . \tag{3.17}$$

In Fig. 3.3.1a the down- (straight line) and up- (dotted line) sweep, so the decrease from positive to negative field magnitudes and vice versa, is depicted for our hybrid sample. Only for **H** $\parallel$ **n**, a difference between the two sweep directions is observed. For further understanding, we use the angle dependent longitudinal resistivities of a hybrid ML (taken from Fig. 3.2.3c) in Fig. 3.3.1b in the respective field geometry marked by the color of the frame.

The field resolved measurement allows to trace the magnetic moment inside the hybrid ML with respect to the applied field. We want to note some assumptions we can take, to simplify the following explanations. As already mentioned, the investigated hybrid ML has a large FM contribution and the FM itself possesses an IP easy-plane anisotropy. Additionally, we assume the saturation field of CoFe at approximately $2.5\,\text{T}$.

We want to begin the discussion with the MR for the magnetic field applied along the current direction **j**, displayed as black curve in Fig. 3.3.1a. The MR is symmetric around zero magnetic field, and for a positive magnetic field sign, two field regions can be identified, in which the MR behaves different. In the high field region from $3.5\,\text{T}$ to $0.03\,\text{T}$, the MR increases moderately while decreasing the field, thus coming from saturation. In the small field region from $0.03\,\text{T}$ to $0\,\text{T}$, the MR decreases abruptly. The high field region is explained by a magnetoresistance effect and we can extract the present alignment of the magnetic moments. As the MR does not change in the whole high field region, we can assume the entity of the magnetic moments to be in the same configuration as during saturation. Therefore, the magnetic moments are aligned parallel to **j**. In order to understand the transition to the small field region, we use the ADMR description in Fig. 3.3.1b. We need a rotation geometry, in which a field application parallel to **j** is possible, representing the magnetic moment direction in saturation. Consequently, we can use the IP and OOPT direction. An alignment of the magnetic moments in OOP direction is not likely, as the magnetization of the FM still wants to align IP due to the easy-plane anisotropy (and the FM dominates over the ML). We can thus exclude a description of the resistivity with the help of the OOPT direction. In contrast, in IP, moving the magnetic moments from **j** ($\alpha = 0°$) to **t** ($\alpha = 90°$), the longitudinal resistivity decreases and this rotation fulfills the anisotropy condition. In summary, in the small field region from $0\,\text{T}$ to $0.03\,\text{T}$, the mag-

netic moments are aligned parallel to **t**. They rotate inside the film plane to **j** at magnetic fields above $0.03\,\text{T}$. This is also consistent with an easy-plane anisotropy.
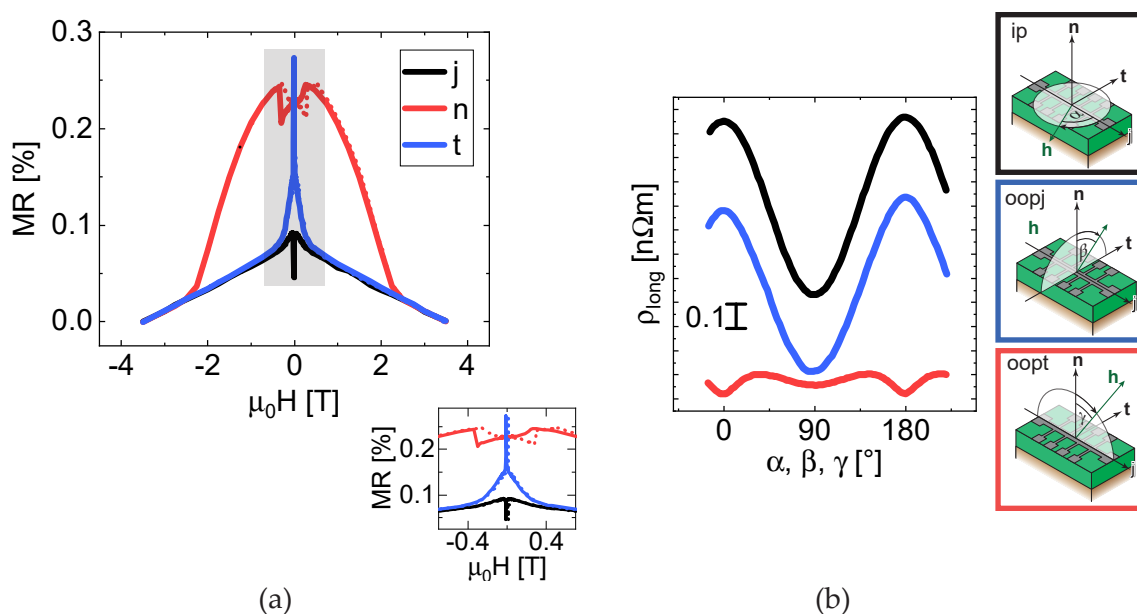

Figure 3.3.1.: MR of hybrid ML (a) MR in **j**, **t** and **n** direction. Dotted lines mark the up field sweep (only for **n** direction different to down sweep). Grey shaded area is zoomed in in figure on bottom. (b) Angle resolved measurement of hybrid ML and definition of field directions, framed with same color (figure adapted from [42]).

We move on to the measurement of the MR for the magnetic field applied in **n** direction. Here, three positive field regimes can be separated: The high field region from $3.5\,\text{T}$ to $2.5\,\text{T}$ with a moderate increase of MR while decreasing the field, the medium field region from $2.5\,\text{T}$ to $0.3\,\text{T}$ with a stronger increase of the MR and the small field region from $0.3\,\text{T}$ to $0\,\text{T}$ with a decrease in the MR. The zoom-in in Fig. 3.3.1a shows the hysteresis in the small field region in detail. The high and medium field region display a magnetoresistance effect. Starting in complete saturation, in the high field region, the magnetic moments are aligned parallel to **n**. In the medium field region, the FM is no longer fully saturated and the magnetic moments move away from the parallel alignment along the **n**-direction. Using the resistivity description in OOPT rotation, the resistivity would increase while moving away from the **n**-direction, whereas in OOPJ it would decrease. Thus, using the OOPT behavior, the increase in MR in the medium field region coming from saturation is explained by an alignment of the magnetic moments towards the **j** direction (so in Fig. 3.3.1b away from $\gamma = 0°$ towards $\gamma = 90°$). The change of the MR at $0.3\,\text{T}$ can indicate the saturation field of the ML. The small field region is explained by use of the ADMR measurements. We can in principle use the OOPJ and OOPT direction, as both involve an application of the magnetic field in **n** direction. Starting with OOPT, we can assume that the magnetic moments are aligned around $\gamma = 45°$ (on their way away from **n** to **j**), thus a decrease in the MR is obtained by rotating towards $\gamma = 90°$ (see Fig. 3.3.1b). In

the OOPJ rotation, we use the movement from $\mathbf{n}$ ($\beta = 0°$) to $\mathbf{t}$ ($\beta = 90°$), which shows a decrease of ρ_{long} in Fig. 3.3.1b. The breaking down of the magnetic moments to IP is again consistent with the easy-plane anisotropy. The hysteresis in this small field region displays the anisotropy inside the hybrid ML, whose anisotropy field needs to be overcome to reach the favorable configuration of the magnetic moments. For magnetic fields e.g. decreasing from positive magnitudes the anisotropy field hinders the alignment in $\mathbf{t}$ or $\mathbf{j}$ direction until a small negative field is applied to overcome the anisotropy field and vice versa for the other sweep direction. The relative contribution of the anisotropy in the MR signal can be estimated by the ratio of the decrease of the MR in the small field region compared to the maximal MR for all field regions. It is about $15\,\%$.

The third MR behavior to investigate is during the application of the field in $\mathbf{t}$-direction. Two positive field regions can be separated, the high field region from $3.5\,\text{T}$ to $0.3\,\text{T}$ with increasing MR while decreasing the field, and the small field region from $0.3\,\text{T}$ to $0\,\text{T}$ with a larger increase in MR. Both field regions exhibit a magnetoresistance effect. In the high field region, the magnetic moments are, analogue to the MR investigation in $\mathbf{j}$-direction, for the whole field region in saturation and thus aligned parallel to $\mathbf{t}$ from $3.5\,\text{T}$ to $0.3\,\text{T}$. In order to explain the small field region, we can use the IP or OOPJ ADMR description, as both include an application of the magnetic field in $\mathbf{t}$ direction. As a movement into the OOP direction is unfavorable due to the easy-plane anisotropy, we do not use the MR behavior in the OOPJ rotation. Instead, using the IP description, the longitudinal resistivity is increased by a movement of the magnetic moments from $\mathbf{t}$ ($\alpha = 90°$) to $\mathbf{j}$ ($\alpha = 0°$). The transition at again $0.3\,\text{T}$ can indicate the saturation field of the ML.

Overall, a magnetoresistance effect is visible for all three magnetic field orientations. The magnetic moments can rotate inside the film plane during an application of the magnetic field in the $\mathbf{j}$ and $\mathbf{t}$ direction. The forcing of the magnetic moments in OOP configuration is unfavorable and only achieved by applying a large enough magnetic field directly in $\mathbf{n}$ direction.

The magnetoresistance behavior is so far described by a simple picture of a homogeneous magnetization overall the whole sample, which rotates in the respective direction. But as investigated [69], in the small field range, the magnetization of our MLs decays into domains. Therefore, we want to revisit the MR in the small field region, where abrupt changes are visible. In our simple picture, a drastic difference in MR would be understood as a sudden jump of the magnetization direction. By help of an explanation with a formation of domains, the change in MR is modeled as an (in our measurement instantaneous) movement of the domain walls. The domain structure changes to an energetically favorable configuration. We can estimate the impact of domain formation on our hybrid ML by comparing the difference of the resistivity in angle dependent measurements for distinct field directions at small magnetic fields with the change in MR in Fig. 3.3.1a in the small field region. The relative resistivity difference obtained in ADMR measurements for field

sample type	approx. MR [%] in **j**-direction	approx. MR [%] in **n**-direction	approx. MR [%] in **t**-direction
FM_1	0.05	0.10	0.17
ML_1	0.02	0.01	0.22
ML_1+FM_1 (CoFe(5))	0.04	0.20	0.05
ML_2+FM_3 (CoFe(20))	0.09	0.25	0.27

Table 3.3.1.: Magnetoresistance MR of different samples in the respective measurement geometry.

rotations in the film plane is five times larger than the difference obtained in MR. Thus, we can assume that the domain formation definitely plays a role in the small field region.

The overall MR behavior in Fig. 3.3.1a is additionally very similar to a FM sample which we have also investigated during this thesis. This reinforces the assumption of the dominance of the FM over the ML. This dominance will be also visible in spin wave measurements in Chapter 4. An overview over MR values in different samples is given in Tab. 3.3.1. The respective samples are denoted in the appendix A.1 and include several MLs, a FM and two different hybrid MLs. The values of different MLs are similar. All values are rather small [62, 65], but the signals of hybrid MLs increase with increasing FM contribution. Direct relations between a hybrid ML and its single contributions from the FM layer and the ML are difficult to obtain. This is reasonable as for example the influence of SMR to AMR is complicated.

Compared to literature, the MR values of our samples are small. For instance, the AMR in MLs containing CoFeB exceeds the MR of our FM by approximately one order of magnitude [70]. The SMR signal in CoFeB heterostructures with similar NM-layer thicknesses is smaller than $0.1\,\%$ [57]. Consequently, a strict assignment of our data to only SMR or AMR effects should be handled with care.

4. Spin Wave Transport

Spin waves are a key issue in spintronics as they are closely related to the manipulation and transport of spins in small structures [53]. These elementary excitations of spins in magnetically ordered materials are a good candidate for alternative information technology mechanisms and are of high interest for researches since the 1950s. Well-known detection methods to investigate the ferromagnetic resonance (FMR) or heavily studied ways to control propagating spin waves manifest the importance of spin wave research [18]. In the following, we want to present two main investigations schemes of resonances in hybrid MLs. Starting with the introduction of basic theoretical concepts in Sec. 4.1 on magnetization dynamics in Sec. 4.1.1, FMR in Sec. 4.1.2 and spin wave resonance in Sec. 4.1.3, we present the analysis of measured resonances in magnetic field IP and OOP configuration. In IP geometry in Sec. 4.2, FMR in Sec. 4.2.1 and spin wave propagation in Sec. 4.2.2 is presented. The latter involves measurements and a simulation. After comparing IP FMR signals to IP spin wave resonance signals in Sec. 4.2.3, also the OOP configuration is investigated in Sec. 4.3 concerning the FMR in Sec. 4.3.1 and the spin wave resonance in Sec. 4.3.2.

4.1. Theoretical Concepts

We now present an overview over the magnetization dynamics of a homogeneous magnetized ferromagnet under the effects of an externally applied magnetic field $\mathbf{H}_0$. First, we assume that all single magnetic moments are coupled and precess phase-synchronized. Consequently, the magnetization can be seen as classical macrospin and its movement can be calculated via classical equations of motion [41]. In this context, we introduce the Landau-Lifshitz equation including Gilbert-damping in Sec. 4.1.1. We derive further equations to describe ferromagnetic resonances, like the Kittel equation in Sec. 4.1.2. Furthermore, we extend our discussion to non-uniformly precessing spin modes, namely propagating spin waves, as excitations at nonzero wave vectors in Sec. 4.1.3. Thereby, we introduce different spin modes of the traveling spin waves and a vector-network analyzer measurement process to detect them.

4.1.1. Magnetization Dynamics

We investigate thin film samples under the influence of an effective magnetic field $\mathbf{H}_{\text{eff}}$. For simplicity, only three most important components of the effective field are accounted, the

external field $\mathbf{H}_0$ pointing in $\mathbf{z}$ direction (coordinate system see Fig. 4.1.1), an anisotropy field $\mathbf{H}_{\text{ani}}$ induced by magnetization dynamics inside magnetic thin films and a demagnetizing field $\mathbf{H}_{\text{demag}}$

$$\mathbf{H}_{\text{eff}} = \mathbf{H}_0 + \mathbf{H}_{\text{ani}} - \mathbf{H}_{\text{demag}} \,. \tag{4.1}$$

The latter depends on the shape of the specimen. By accounting the entire solid state body with its volume V, a macrospin model is introduced

$$\mathbf{M} = 1/V \sum_{m_i \in V} \boldsymbol{\mu}_i \,, \tag{4.2}$$

with the magnetic moment $\boldsymbol{\mu}$. The magnetization $\mathbf{M}$ is therefore defined as the magnetic moment per volume and in an equilibrium situation, the direction of the magnetization points along the effective field. By deflecting the magnetic moment out of the equilibrium position, a torque $\mathbf{T}$ appears, pointing perpendicular to the magnetization direction and the effective field. In Fig. 4.1.1 it is marked as blue arrow

$$\mathbf{T} = \boldsymbol{\mu} \times \mu_0 \mathbf{H}_{\text{eff}} \,. \tag{4.3}$$

The torque causes a precessional motion around the direction of the effective magnetic field and without damping the movement would persist. We want to reformulate $\mathbf{T}$, therefore we connect the magnetic moment to the angular momentum $\mathbf{J}$. They are pointing antiparallel and the relation can be described via the gyromagnetic ratio $\gamma = \frac{g\mu_{\text{B}}}{\hbar}$ using the Landé-factor g and the Bohr magneton $\mu_{\text{B}} = \frac{e}{2m_{\text{e}}}\hbar$

$$\boldsymbol{\mu} = -\gamma \mathbf{J} \,. \tag{4.4}$$

The torque is additionally expressed as derivative of the angular momentum with respect to time $\mathbf{T} = \frac{\partial \mathbf{J}}{\partial t}$. By use of the just taken assumptions and by help of the macrospin model, Eq. (4.3) and Eq. (4.4) can be combined [71] to the Landau-Lifshitz equation [72]

$$\frac{d\mathbf{M}}{dt} = -\gamma(\mathbf{M} \times \mu_0 \mathbf{H}_{\text{eff}}) \,. \tag{4.5}$$

It describes a precession of the macroscopic magnetization around the effective field axis at an angular frequency $\omega = \gamma \mu_0 H_{\text{eff}}$.

To apply this equation of motion to real situations and allow the magnetization to align with the applied field after some time, losses have to be taken into account. They are represented by an additional torque towards the field axis with the phenomenological damping term α. The resulting Landau-Lifshitz-Gilbert equation [74] reads as follows

$$\frac{d\mathbf{M}}{dt} = -\gamma(\mathbf{M} \times \mu_0 \mathbf{H}_{\text{eff}}) + \frac{\alpha}{M_{\text{s}}}\left(\mathbf{M} \times \frac{d\mathbf{M}}{dt}\right), \tag{4.6}$$

using the saturation magnetization M_{s}. The first term describes the precession of the mag-
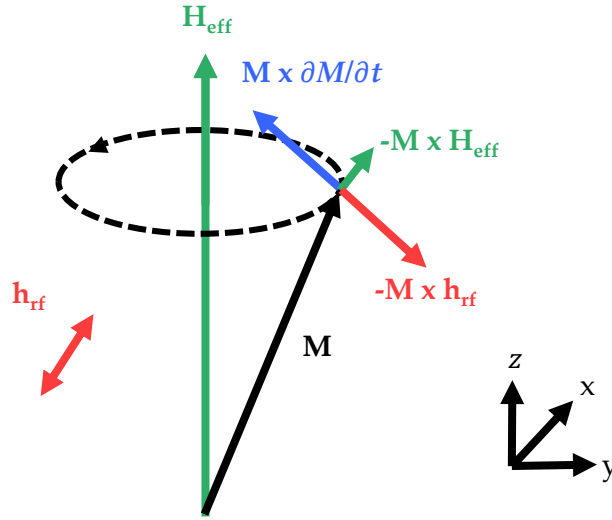
Figure 4.1.1.: The torque (green), induced by the effective magnetic field $\mathbf{H}_{\mathrm{eff}}$ (green), causes a tilting of the magnetization into a precessional motion (dotted line) around the effective field axis (green). The damping term (blue) allows a spiralizing motion towards the field axis. The oscillatory driving field (red) counteracts the damping torque and the movement is driven around the effective field axis (dotted line). The figure is adapted from [73].

netization around the effective field, whereas the second one accounts for damping. This equation expresses the dynamics of the magnetization in a time dependent effective field. Therefore, we modify the effective magnetic field Eq. (4.1) to $\mathbf{H}_{\mathrm{eff}} = \mathbf{H}_0 + \mathbf{H}_{\mathrm{ani}}(t) - \mathbf{H}_{\mathrm{demag}}(t)$.

The resulting damped motion of the precessing magnetization now spirals in towards the direction of the effective field. To counteract this process, one applies an oscillatory $\mathbf{h}_{\mathrm{rf}}$ field perpendicular to the effective field (in the x-y-plane, see Fig. 4.1.1) resulting in a sustained precessional motion. The effective field in Eq. (4.1) is once again changed to $\mathbf{H}_{\mathrm{eff}} = \mathbf{H}_0 + \mathbf{H}_{\mathrm{ani}}(t) - \mathbf{H}_{\mathrm{demag}}(t) + \mathbf{h}_{\mathrm{rf}}(t)$. Whenever the oscillatory frequency is equal to the resonance frequency of the precessing magnetization, the absorbed energy of the system is maximized. The characteristic resonance frequency ω_{res} depends on the time-averaged effective field $< \mathbf{H}_{\mathrm{eff}} >$ and the resonance condition can be specified to

$$\omega_{\mathrm{res}} = \gamma \mu_0 < \mathbf{H}_{\mathrm{eff}} > . \tag{4.7}$$

4.1.2. Ferromagnetic Resonance

Ferromagnetic resonance (FMR) describes the uniform precession mode of the entity of spins (magnetic moments). To find this resonance condition, according to Eq. (4.7), the effective magnetic field has to be analyzed. The demagnetizing field $\mathbf{H}_{\mathrm{demag}}$, caused by shape anisotropy, is characterized by the demagnetizing tensor N and thus the shape of the specimen [75]. For simplicity, the specimen is assumed as ellipsoid having its principal axis

z parallel to the external field direction $\mathbf{H}_0$ and therefore being magnetized in this direction. The demagnetizing field can be written as $\mathbf{H}_{\mathrm{demag}} = N\mathbf{M}$ with vanishing off-diagonal elements of the tensor N (due to the elliptical specimen shape) and diagonal elements N_i in x-, y- and z-direction [76]. Any other anisotropy contributions in $\mathbf{H}_{\mathrm{ani}}$ will be neglected here. The next step is to solve the Landau-Lifshitz-Gilbert Eq. (4.6) using an exponential ansatz for $\mathbf{M}$ and $\mathbf{h}_{\mathrm{rf}}$ [77], keeping in mind that the dynamics still happen in the x-y-plane, whereas the applied external field points in z-direction

$$\begin{pmatrix} h_{\mathrm{x}} \\ h_{\mathrm{y}} \end{pmatrix} = \chi^{-1} \begin{pmatrix} m_{\mathrm{x}} \\ m_{\mathrm{y}} \end{pmatrix} . \tag{4.8}$$

The magnetization is expressed as $\mathbf{M} = M_{\mathrm{s}} \cdot \mathbf{m}$ with its direction $\mathbf{m}$. The calculation of the unitless Polder susceptibility χ [77] is achieved by using the relation $\mathbf{m}M_{\mathrm{s}} = \chi\mathbf{h}_{\mathrm{rf}}$. Thus, the susceptibility is the linear response of the magnetization direction to the driving field $\mathbf{h}_{\mathrm{rf}}$ and can be solved by [78]

$$\chi = \frac{M_{\mathrm{s}}}{\det(\chi^{-1})} \begin{pmatrix} H_0 + M_{\mathrm{s}}(N_{\mathrm{y}} - N_{\mathrm{z}}) + \frac{i\alpha\omega}{\mu_0\gamma} & \frac{i\omega}{\mu_0\gamma} \\ -\frac{i\omega}{\mu_0\gamma} & H_0 + M_{\mathrm{s}}(N_{\mathrm{x}} - N_{\mathrm{z}}) + \frac{i\alpha\omega}{\mu_0\gamma} \end{pmatrix} . \tag{4.9}$$

The resonance condition is met whenever χ is maximized. We search for solutions to $\det(\chi^{-1}) = 0$, solved for either the external magnetic field H_0 or the frequency ω. The real part of the solution leads to the resonance field H_{res} or resonance frequency $f_{\mathrm{res}} = \frac{\omega_{\mathrm{res}}}{2\pi}$, whereas the imaginary part reveals the half-width at half-maximum (HWHM) linewidth of the magnetic field ΔH or the frequency $\Delta\omega$

$$\omega_{\mathrm{res}} = \mu_0\gamma\sqrt{[H_0 + M_{\mathrm{s}}(N_{\mathrm{x}} - N_{\mathrm{z}})][H_0 + M_{\mathrm{s}}(N_{\mathrm{y}} - N_{\mathrm{z}})]}, \tag{4.10}$$

$$\Delta H = \alpha \frac{\omega}{\mu_0\gamma} . \tag{4.11}$$

Equation (4.10) is called Kittel equation [75] and Eq. (4.11) displays the field linewidth as function of the frequency. Further expressions for the linewidth can be found in [78]. Conducting magnetic resonance experiments on thin films structures raises the need for further frequency-independent long-ranging magnetic inhomogeneities. This contribution H_{inh} is added to the HWHM field linewidth as inhomogeneous linewidth broadening [27]:

$$\Delta H = \alpha \frac{\omega}{\mu_0\gamma} + H_{\mathrm{inh}} . \tag{4.12}$$

Further magnetic anisotropies can be implemented by using an anisotropy field H_{ani} as summand in the effective magnetic field H_{eff}. This anisotropy field can originate from interfacial uniaxial out-of-plane anisotropies in magnetic thin films which cannot be separated from demagnetizing fields during an experiment. In this case, the saturation magnetization M_{s} is replaced by the effective magnetization $M_{\mathrm{eff}} = M_{\mathrm{s}} - H_{\mathrm{k}}$ with an out-of-plane

uniaxial anisotropy field H_k [79]. In-plane anisotropies are suppressed due to a constantly rotating material deposition during the sample fabrication.

In thin films, the FMR mode described by the Kittel equation (4.10) can be specified for the applied magnetic field orientation. The general formalism in Eq. (4.10) can be elaborated for IP and OOP field orientation by inserting the respective demagnetization factors. In IP configuration with either $N_x = 1$ or $N_y = 1$ and $N_z = 0$, the Kittel equation reads

$$\omega_{\mathrm{res}} = \mu_0 \gamma \sqrt{H_0 \cdot (H_0 + M_{\mathrm{s}})} \, . \tag{4.13}$$

In OOP configuration, with the only non-zero demagnetizing factor N_z, Eq. (4.10) takes the form

$$\omega_{\mathrm{res}} = \mu_0 \gamma (H_0 - M_{\mathrm{s}}) \, . \tag{4.14}$$

The replacement of the M_{s} by an effective magnetization in both equations is still required and accounts for anisotropy effects.

4.1.3. Spin Wave Resonance

So far, we presented a model to describe a system of uniformly moving macrospins with zero wave vector. We take one step further by characterizing excitations of a coupled spin system with nonzero wave vector. The system, the so-called spin waves or magnons, are now able to propagate. We enunciate the coupling between the spin waves as dipolar and exchange interactions, depending on the range of the interaction [80].

Exchange interactions must be taken into account for sample dimensions in the µm regime [81] and can be expressed via an exchange field H_{ex} with an exchange constant A and the wave vector k [82]

$$\mu_0 H_{\mathrm{ex}} = \frac{2A}{M_{\mathrm{s}}} k^2 \, . \tag{4.15}$$

Investigating thin films in the limit of long wavelengths moves them into the dipolar regime (compared to the exchange interaction regime) [83]. Here, only if the magnetization includes an OOP component, demagnetizing fields are present. For IP magnetized films two cases can be distinguished. The dipolar field component which is pointing OOP, is independent of the characteristic angle Φ. Φ is spanned between the magnetization direction and the propagation direction of spin waves along the wave vector $\mathbf{k}$. The other case describes the dipolar field component along IP, which reveals a $\sin^2(\Phi)$ behavior. In order to evaluate the spin wave propagation, we want to combine the effects of both exchange and dipolar interactions on spin waves. This is only analytically feasible by considering certain constraints. Firstly, we assume a tangentially magnetized thin film (with either $N_x = 1$ or $N_y = 1$) and secondly the dynamic magnetization is uniform throughout the film thickness d. This now allows to explicitly calculate the dispersion relation of dipolar-exchange spin waves [78].

The behavior of spin waves and their dispersion strongly depends on the orientation of the
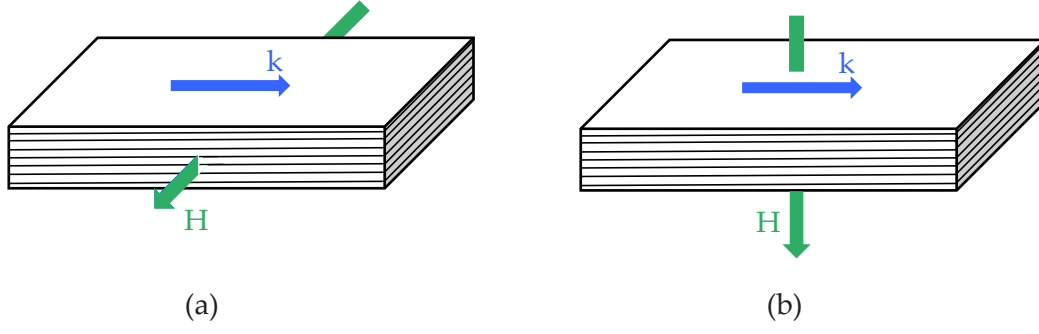
Figure 4.1.2.: Spin wave modes (a) DE mode: surface modes with wave vectors parallel to the sample surface and perpendicular to the external field. The external field is applied in the film plane. (b) FV mode: exists in the bulk of the sample. The wave vector is orientated parallel to the sample surface and perpendicular to the external field which is perpendicular to the sample surface.

wave vector k with respect to the magnetization direction M. Thus, several modes can be classified. All spin waves with magnetization direction OOP of the film and propagating IP of the film are called forward volume magnetostatic spin waves (FV) (see Fig. 4.1.2b). This mode dominates in the regime of sufficiently large wavelengths and is mainly present inside of the sample [84]. IP magnetized thin films can support surface and volume modes. In this work, we investigate Damon-Eshbach modes (DE), also called magnetostatic surface spin waves, that reveal a propagation direction perpendicular to the magnetization [37] (see Fig. 4.1.2a). The amplitude of the surface wave decays into the volume of the sample and the mode dominates at short wavelengths [85]. As introduced above, the characteristic angle of DE spin waves is $\Phi = \pi/2$. In order to investigate both IP and OOP magnetized films, the measurements are performed in FV and DE configuration.

In order to describe the magnetic response of propagating spin waves, the Polder susceptibility derived in Eq. (4.9) can be transformed into the regime of nonzero wave vectors [86]. It involves slightly different field definitions, which need the film thickness d and the exchange field in Eq. (4.15)

$$H_{\mathrm{x}}^{\mathrm{dip}} = M_{\mathrm{s}} \frac{1 - e^{-kd}}{kd}\,, \tag{4.16}$$

$$H_{\mathrm{y}}^{\mathrm{dip}} = M_{\mathrm{s}} \left(1 - \frac{1 - e^{-kd}}{kd}\right) \sin^2(\Phi)\,. \tag{4.17}$$

The inverse spin wave susceptibility depending on the wave vector k then reads [78]:

$$\chi_k^{-1} = \begin{pmatrix} H_0 + H_{\mathrm{ex}} + H_{\mathrm{x}}^{\mathrm{dip}} + \frac{i\alpha\omega}{\mu_0\gamma} & -\frac{i\omega}{\mu_0\gamma} \\ \frac{i\omega}{\mu_0\gamma} & H_0 + H_{\mathrm{ex}} + H_{\mathrm{y}}^{\mathrm{dip}} + \frac{i\alpha\omega}{\mu_0\gamma} \end{pmatrix}. \tag{4.18}$$

As for solving the susceptibility in the FMR case, the determinant $\det\!\left(\chi_k^{-1}\right)$ is set to zero.

The real part provides the wave vector dependent spin wave resonance [78, 87]

$$\omega_{\mathrm{k}} = \mu_0 \gamma \sqrt{(H_0 + H_{\mathrm{ex}} + H_{\mathrm{x}}^{\mathrm{dip}})(H_0 + H_{\mathrm{ex}} + H_{\mathrm{y}}^{\mathrm{dip}})}, \tag{4.19}$$

well-known as the Kalinikos-Slavin equation. Using the imaginary part of the solution to $\det(\chi_k^{-1}) = 0$ results in the spin wave linewidths for e.g. the frequency linewidth as function of the field

$$\Delta\omega_k = \alpha\mu_0\gamma\left(H_0 + H_{\mathrm{ex}} + \frac{1}{2}(H_{\mathrm{x}}^{\mathrm{dip}} + H_{\mathrm{y}}^{\mathrm{dip}})\right). \tag{4.20}$$

Various parameters can be deduced using Eq. (4.19) and Eq. (4.20). From the dispersion relation in Eq. (4.19), the spin wave group velocity can be extracted

$$v_{\mathrm{g}} = \frac{\partial\omega_{\mathrm{k}}}{\partial k}. \tag{4.21}$$

Using the frequency linewidth defined in Eq. (4.20), we obtain the spin wave lifetime

$$\tau_{\mathrm{k}} = \frac{1}{\Delta\omega_{\mathrm{k}}} \tag{4.22}$$

and the spin wave propagation length

$$l_{\mathrm{k}} = \tau_{\mathrm{k}} \mid v_{\mathrm{g}} \mid. \tag{4.23}$$

The latter can be expressed normalized to the spin wave wavelength $\lambda = \frac{2\pi}{k}$.

In this thesis an all-electrical concept to investigate propagating spin waves is used, whose setup is depicted in Fig. 4.1.3. The thin film sample is connected to a vector network analyzer (VNA) and is put into a static external magnetic field oriented according to the desired measurement geometry. On top of the ML sample two parallel antennas are placed which are designed as CPW antennas (see chapter 2.2.2). They are fabricated onto the surface of the ML sample, both connected to the ports of the VNA and ground, being able to excite and detect spin waves. One port of the VNA sends an ac current through the first antenna, inducing a magnetic field and thus exciting a spin wave propagating away from the antenna. Parts of the spin wave travel towards the second antenna and generate an electric response being measured of the VNA in port two. The VNA extracts the magnitude and phase of the signal in the form of a matrix with four scattering or S-parameters. The components of the matrix S_{ij} are defined as the ratio of the complex incident voltage V_i^{in} at port i to the output voltage V_j^{out} at port j [88]. Magnitude and phase are included in the complex voltage parameter $S_{ij} = \frac{V_i}{V_j} = \frac{|V_i|}{|V_j|}e^{i(\phi_i - \phi_j)}$ [89]. Diagonal S-parameters S_{11} and S_{22} display the reflection of the signal at the respective port, while off-diagonal elements S_{12} and S_{21} represent the transmission of the signal for e.g. S_{12} from port two to port one.
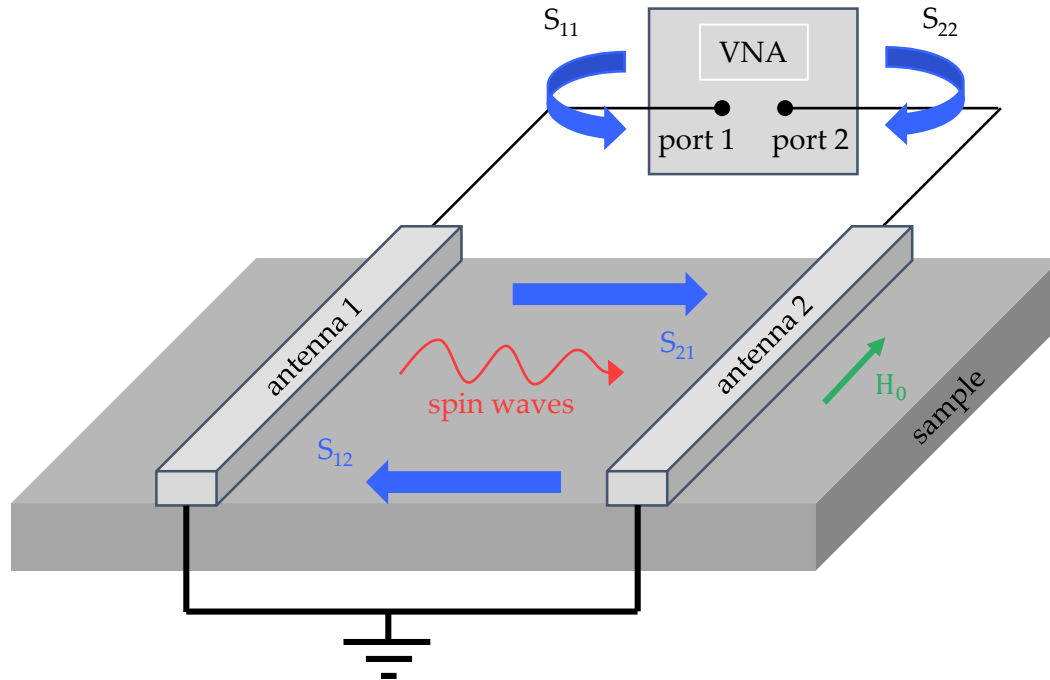
Figure 4.1.3.: Schematic measurement setup of a VNA detection of propagating spin waves in presence of an externally applied field H_0. The sample (grey) with two antennas (light grey) is connected to the VNA and grounded. The VNA excites spin waves (red) in port one which propagate to the second antenna. They are detected at port two. Whether to extract the reflection or the transmission depends on the recorded S-parameters (blue). The depicted magnetic field (green) is orientated perpendicular to the wave vector of the spin wave in order to measure in DE geometry. The figure is adapted from [88].

4.2. Spin Waves in In-plane Magnetized Magnetic Multilayers

After having introduced several theoretical concepts, we investigate the hybrid ML Ta(1.5)/Pt(4)/Cu(2)/[Pt(0.5)/CoFe(1.17)/Ir(0.7)]$_6$/Ru(5)/CoFe(20)/Ru(2)/Ta(2) by means of ferromagnetic and spin wave resonance in IP field configuration. Both techniques enable the extraction of magnetic parameters and allow to understand the propagation characteristics of spin waves. We already investigated the charge transport in this hybrid ML in Sec. 3.3 and extend our discussion now to spin transport. This sample is a hybrid ML with a relatively thick FM layer (20 nm) compared to the ML. We start with an IP investigation of the FMR in Sec. 4.2.1 and discuss the propagating spin wave resonance in Sec. 4.2.2. The latter includes an analysis of the measured resonances and a corresponding simulation. In Sec. 4.2.3 the FMR and spin wave resonance are compared to each other.

4.2.1. Ferromagnetic Resonance

The IP FMR analysis of this plain hybrid ML sample allows to determine the magnetic properties of this sample, in particular the magnetic damping and anisotropies. Thereby, we record the resonance modes at zero wave vector as a function of the frequency and the

externally applied magnetic field. All measurements are performed at room temperature and the real part of the obtained FMR of the thin film is depicted in Fig. 4.2.1a. The data is background corrected via the model of derivative-divide (DD, d_D/dH) [90].

In the IP configuration, we use the elaborated Kittel Eq. (4.13), revealing a square root dependence between resonance frequency and field. This is visible in the resonance mode in Fig. 4.2.1a. The slope of the resonance curve is characterized by the Landé-factor g. For the application of the Kittel equation (4.13), we need to assume a present macro spin (see beginning of Sec. 4.1) and that the magnetization is aligned parallel to the direction of the externally applied magnetic field. In contrast, the formalism may not be used in the case of domain formation. To avoid the non-alignment of the magnetization, the FMR spectroscopy measurements are started after full saturation of the thin films.

We want to analyze the IP Kittel mode in Fig. 4.2.1a further. It is well pronounced reaching over the whole depicted frequency and field range. The kink below zero field displays the mirroring of the positive resonance mode to negative field magnitudes. For hybrid MLs two resonance modes are expected, one for the ML and one for the FM. But in Fig. 4.2.1a only one mode is distinguishable with a rather broad linewidth. Analyzing Eq. (4.13) allows to assign the saturation fields of ML and FM as value of the field separating the ML and FM mode. Their values are supposed to be different, thus we would assume to detect the two different modes. As only one mode is visible, we conclude to only see the more pronounced FM mode, whereas the ML mode is coincident within the FM mode linewidth and the ML mode is of smaller signal intensity. The reduced resonance signal of the ML is explained by damping. In IP, the effect of two-magnon-scattering is present, which is suppressed in OOP due to non-existing dispersion branches. The ML resonance is weakened in IP and included in the broad FM linewidth. Consequently, the ML resonance cannot be resolved.
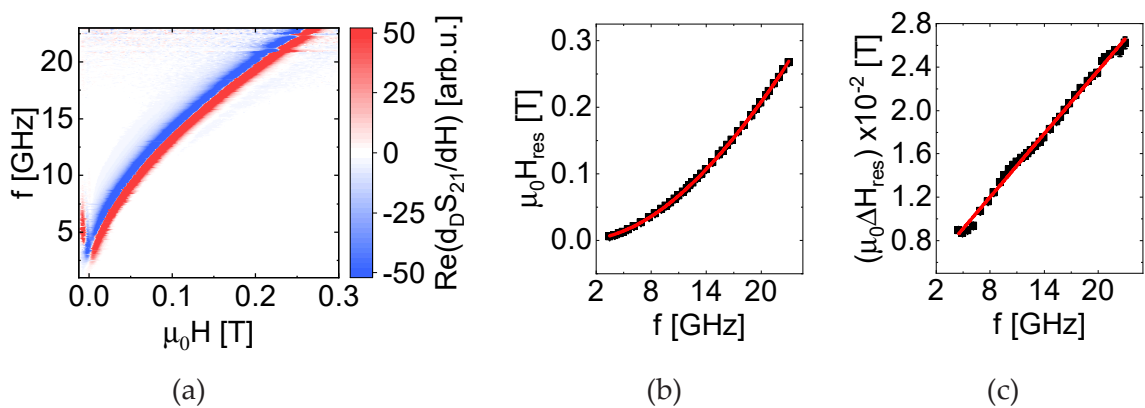

(a)   (b)   (c)

Figure 4.2.1.: FMR in IP configuration and analysis (a) FMR depending on the magnetic field and frequency. (b) The Kittel equation is applied. The error bars of the resonance field are within the size of the data symbols. (c) The resonance linewidth of the FMR as function of the frequency is depicted and fitted, with error bars smaller than the symbol size.

By help of the IP FMR, several material parameters can be extracted, quantifying the magnetization dynamics in the hybrid ML. We use the Kittel Eq. (4.13) and substitute the saturation magnetization by an effective magnetization and an uniaxial anisotropy field $M_s = M_{\text{eff}} + H_k$ [27]. Fitting this to the resonance field as function of the frequency (see Fig. 4.2.1b) allows to determine the Landé-factor $g = 2.096 \pm 0.043$ and the effective magnetization $\mu_0 M_{\text{eff}} = 2.017 \pm 0.087$ T. The Landé-factor has a reasonable value compared to that of a free electron $g = 2.0023$ and ferromagnets in general $g \approx 2$ [71]. The positive value of the effective magnetization allows to define the FM, as dominating signal of the hybrid ML, as IP easy-plane system [79]. The value and the suppression of the ML resonance is comparable with other hybrid MLs of similar constitution [31]. The magnetic field resonance linewidth in Fig. 4.2.1c is fitted by Eq. (4.12) and leads to the parameters $\alpha = (1.422 \pm 0.023) \cdot 10^{-2}$ and $\mu_0 H_{\text{inh}} = 0.428 \pm 0.019$ T. $\mu_0 H_{\text{inh}}$ is attributed to an additional linewidth broadening due to magnetic inhomogeneities [91]. As no skyrmions are anticipated in the CoFe, the present damping simply displays the damping of the spin dynamics in the FM. Due to the magnetic texturing in the ML, an additional damping can appear, which affects the spin waves. The Gilbert damping value is smaller compared to a similar composed hybrid ML with seven repetitions (compare to [31]). Overall, the in general rather small α allows to investigate propagating spin waves at all.

4.2.2. Spin Wave Propagation

We move on to an analysis of the propagation of spin waves with non-zero wave vector. We present spin wave propagation in DE geometry. In this regard, we investigate the measured spin wave resonance, simulate the resonance and compare the results.

Measurements

The spin wave resonance of the hybrid ML is measured with respect to field and frequency. Therefor, we structure the plain samples, used for FMR, to waveguides usable for spin wave spectroscopy (see Sec. 2.2.2). The measurement setup is discussed in Sec. 4.1.3 and frequencies from 0 GHz to 40 GHz, as well as magnetic field from -0.1 T to at least 0.8 T are applied. The obtained data is background corrected (DD) and its real part is depicted in Fig. 4.2.2a. Several less pronounced modes are visible below 15 GHz whereas at higher frequencies only one broader mode is evident. The sample is measured in IP configuration thus we can observe the DE spin wave mode.

The analysis of the spin wave resonance frequency in DE configuration allows to extract material parameters similar to the Kittel fit application on the FMR. The spin wave resonance in Fig. 4.2.2b extracted from Fig. 4.2.2a is fitted by the dispersion relation provided by the Kalinikos-Slavin Eq. (4.19) by use of the adapted saturation magnetization $M_s = M_{\text{eff}} + H_k$. Additionally anisotropy contributions are governed by a demagnetiza-
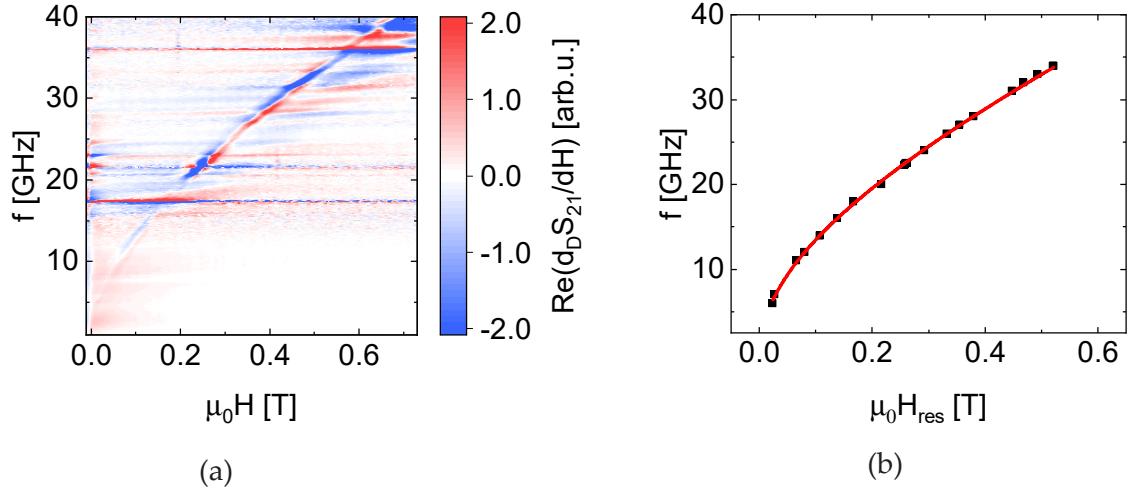
Figure 4.2.2.: Spin wave resonance in IP and analysis (a) Real part of the measured IP spin wave resonance which is background corrected. (b) The Kalinikos-Slavin fit in DE geometry is applied to the spin wave resonance.

tion field H_{demag} [92]. Thus, the Kalinikos-Slavin equation transforms to

$$\omega_{\text{k}} = \mu_0 \gamma \sqrt{(H_0 + H_{\text{demag}} + H_{\text{k}} + H_{\text{x}}^{\text{dip}})(H_0 + H_{\text{demag}} + H_{\text{y}}^{\text{dip}})} \,. \tag{4.24}$$

In order to obtain the demagnetization field and the wave vector by fitting Eq. (4.24) to the spin wave resonance, we need to assume a value for the saturation magnetization and insert the sample film thickness. We use a saturation magnetization of $\mu_0 M_{\text{s}} = 2.35\,\text{T}$ and the total film thickness dominated by the thickness of the FM layer. The extracted values for the saturation magnetization of the FMR and spin wave resonance should be identical, as the samples are deposited on the same run. The herein used M_{s} can be deduced from the effective magnetization extracted by FMR, as M_{s} of the spin wave resonance is corrected by H_{k}. Additionally, as the waveguide is of a width of only $2\,\mu\text{m}$, modes due to the geometrical confinement of the propagating spin waves have to be taken into account [27]. They are implemented in Eq. (4.24) by a modification of the wave vector [93]. Nevertheless, the value of the saturation magnetization is comparable to the value extracted by the FMR with corrections by the small uniaxial anisotropy field. In conclusion, we obtain $\mu_0 H_{\text{demag}} = 0.005 \pm 0.008\,\text{T}$ and the mainly excited wave vector $k = 0.985 \pm 0.004\,\mu\text{m}^{-1}$. This wave vector will be evaluated in the context of the simulation.

We can calculate the propagation length by use of the extracted parameters from the Kittel fit in Eq. (4.13), the Kalinikos-Slavin fit in Eq. (4.19) and the spin wave linewidth in Eq. (4.20). These equations enable calculating the group velocity in Eq. (4.21) depending on the applied magnetic field as well as the spin wave lifetime τ_{k} in Eq. (4.22) and the spin wave propagation length l_{k} in Eq. (4.23). The latter two are depicted in Fig. 4.2.3 where τ_{k} serves for the calculation of l_{k}/λ. The propagation length is very well comparable to hybrid MLs

with seven repetitions of the trilayer. By instance, at a magnetic field of $0.1\,\mathrm{T}$, we obtain $l_\mathrm{k} = 2.5\,\mu\mathrm{m}$ which fits very well into the data of [31]. Nevertheless, it is an overall rather small value (compared to [27]) and might be caused by the ML interfaces and the related two-magnon scattering.
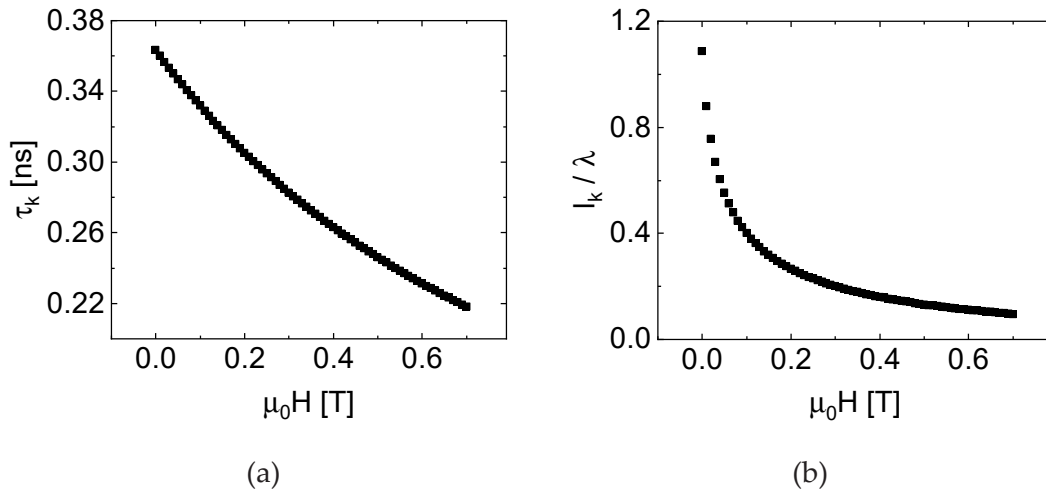

(a)   (b)

Figure 4.2.3.: Spin wave analyis in DE configuration (a) The spin wave lifetime is depicted with respect to the applied magnetic field. (b) The spin wave propagation length normalized to the spin wave wavelength is shown depending on the applied magnetic field.

DE spin waves are able to overcome the reciprocity of spin waves given by the reciprocity theorem of electromagnetism [88]. By comparison of measurements of the scattering parameters S_{12} and S_{21} at positive and negative field magnitude, we can analyze the reciprocity of the two CPW antennas. Thereby, we compare the spin waves traveling in opposite directions determined by S_{ij} concerning their resonance field and intensity. We obtain a reciprocity in the resonance field as the magnitude of the negative resonance field corresponds to the positive one. This is traced back on an antenna reciprocity. But we receive an non-reciprocity in the transmission amplitude which is due to a non-reciprocal excitation efficiency of the antenna. In detail, when the propagation direction of the DE mode spin wave is reversed, the antenna excitation efficiency is also changed. A non-reciprocal wave propagation as reason for the non-reciprocity in the transmission amplitude is not likely. The effect of a reversed spin wave propagation direction would be a shifting spin wave from one film surface to the other [94]. But as the CoFe is assumed to be drastically thinner than the wavelength of the spin wave, the spin wave cannot penetrate into the CoFe and change to other film surfaces. Nevertheless in summary, the antenna itself is deduced as reciprocal, whereas its excitation efficiency is non-reciprocal.

Simulation

We simulate the propagating spin wave resonance in DE-geometry by use of the wave vector dependent susceptibility in Eq. (4.18) combined with the exchange field (4.15) and the field definitions (4.16) and (4.17). The comparison to the recorded transmission S-parameter is possible, as apart from background transmissions through the CPW and field-independent parameters, S_{21} is direct proportional to the susceptibility [27].

A first intuition of the resonance mode is given in Fig. 4.2.4. $\chi(k, f, H)$ is derived from the field dependent component of the inverse susceptibility in Eq. (4.18). This one diagonal entry is inverted and integrated over positive finite k to cancel out the explicit dependence on the wave vector. The real part of the resulting DE resonance mode at varying frequency and field is depicted in Fig. 4.2.4. The used parameters are taken from a $20\,\text{nm}$ thick CoFe thin film with an exchange stiffness constant $A = 20\,\text{pJ}\,\text{m}^{-1}$ [28]. The values of the saturation magnetization, Gilbert damping α and Landé-factor are taken from the extracted fit parameters of the FMR in IP configuration (see Sec. 4.2.1). The field and frequency relation of the mode can be described by the Kalinikos-Slavin Eq. (4.19) as already done with the measured DE resonance in Sec. 4.2.2.

The so far developed simulation displays only the theoretically predicted spin wave mode. To elaborate the model, we introduce adaptions depending on the CPW antenna structure by implementing a wave vector efficiency of the antenna in Fig. 4.2.5a and a structure induced phase change in Fig. 4.2.5b. Both parts are addressed in detail in the following.

The antenna efficiency $\eta(k)$ is deduced via the Karlqvist equations [95, 96] which describe the magnetic field in the cross section plane of the antenna, assuming its width is much larger than its thickness. We analyze the field parallel to the driving field h_{rf} which couple together most efficiently [88]. η is modeled by a Fourier transformed convolution of multiple Dirac delta functions with a rectangle function

$$\eta(k) \propto |\,\mathfrak{F}\Big([\Pi(x + w_{\text{cc}}) * \delta(x)] - [\Pi(x + w_{\text{gr}}) * \delta(x - d_{\text{gap}})] - [\Pi(x + w_{\text{cc}}) * \delta(x + d_{\text{gap}})]\Big)\,|\,. \quad (4.25)$$

The rectangle function is defined by the dimensions of the CPW antenna, in detail the width of the centerconductor w_{cc} and the width of the left and right ground plane of the antenna w_{gr} and Π is based on the Karlqvist equations. The Dirac delta function is specified by the distance between the centerconductor and the ground planes d_{gap} and its sign depends on the direction of the current flow [97]. We receive an expression for the antenna efficiency with respect to the wave vector $\eta(k)$ in Fig. 4.2.5a. The maximal efficiently excited k can be extracted to $k = 1.4\,\mu\text{m}$. We use this CPW antenna design as it excites spin waves near the FMR and also at higher wave vectors with a sufficiently large efficiency. This enables adequate propagation lengths for traveling spin waves. Nevertheless, as seen in Fig. 4.2.3b, the spin wave propagation length is small in general compared to other magnetic material
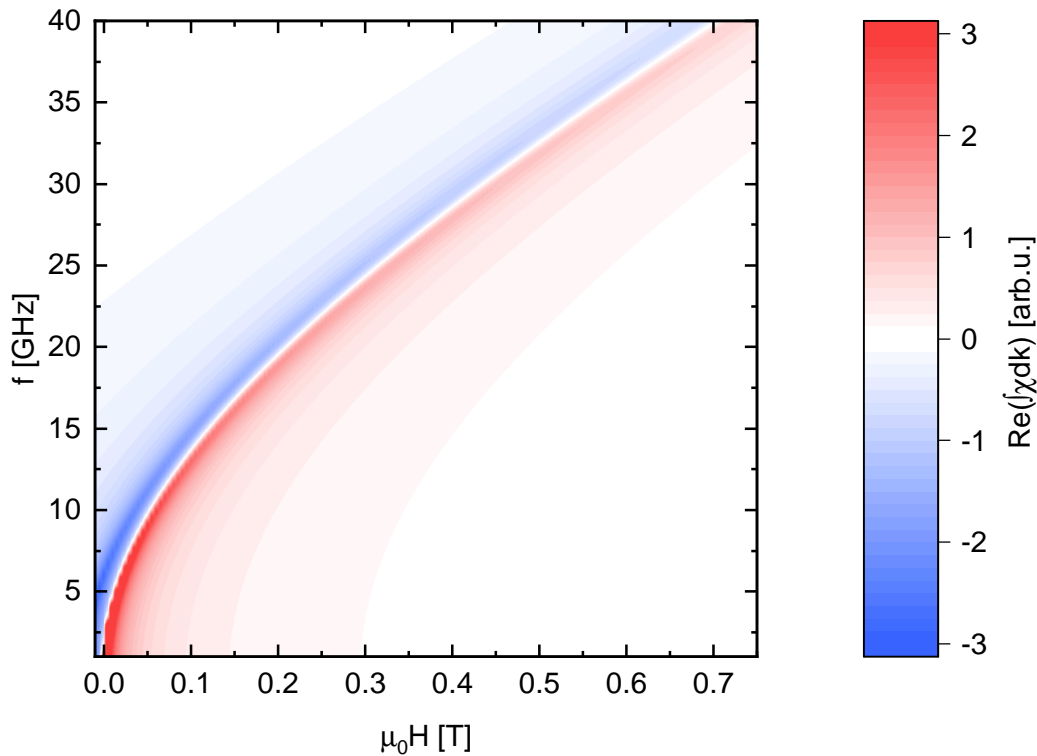
Figure 4.2.4.: Simulation of the IP spin wave resonance. The real part of the susceptibility integrated over the wave vector is depicted.

systems but comparable to hybrid MLs.

The wave vector obtained via the antenna efficiency is close to the one extracted by the analysis of the spin wave resonance in Sec. 4.2.2. The deviation between the two values is explainable as the antenna efficiency to extract the mainly excited wave vector uses the theoretical dimensions inserted in the design of the CPW antenna. During the fabrication process, the actual widths of the antenna are highly likely to change slightly and thus the sample antenna is not a perfect copy of the designed structure. This affects the theoretically predicted wave vector.

Further adaptions to the simulation are done by introducing a phase delay $\phi(k) = \sin(k \cdot \delta)$ due to the propagation of spin waves depending on the wave vector. It is attributed to the finite size between the antennas δ [98] and can be simply understood by tracing the propagation path of a spin wave. Being excited at one antenna, it travels to the second antenna for detection but can be cut off depending on the relation between its propagation length and the separation between the antennas. This introduces a change of phase depicted in Fig. 4.2.5b. The red shaded area marks an imaginable linear relation between ϕ and k and it is present as the sin-behavior of the phase delay is hard to distinguish.

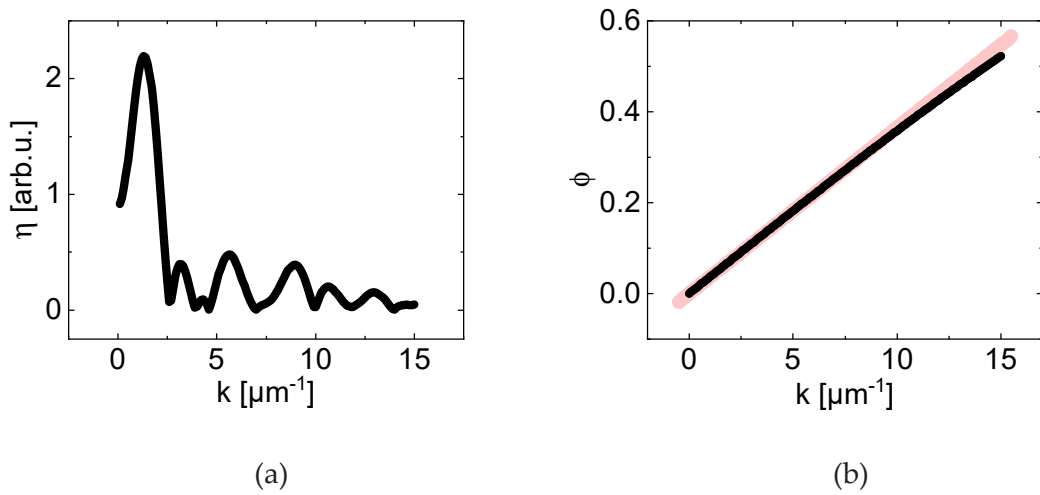The final susceptibility $\chi^*(f, H)$ to model the measurement is obtained by weighting χ in

(a)

(b)

Figure 4.2.5.: Adaptions to the simulation (a) The excitation efficiency η as function of the wave vector. (b) The phase delay ϕ due to the propagation of the spin wave as function of the wave vector. The red shaded area marks a linear relation between ϕ and k.

Fig. 4.2.4 with η and ϕ and integrating it over k to cancel out its dependence on the wave vector

$$\chi^*(f, H) = \int_k \eta(k)^2 \cdot \phi(k) \cdot \chi(k, f, H) dk . \tag{4.26}$$

The antenna efficiency is squared, as it affects $\chi(k, f, H)$ two times, once while exciting the spin wave and once while detecting it. The resonance χ^* is background corrected following the derivative-divide model in the same way the actual measurement is treated. The real part of the result is depicted in Fig. 4.2.6a. The introduced oscillations compared to the not-weighted susceptibility in Fig. 4.2.4 are due to the terms $\eta(k)$ and $\phi(k)$. Oscilations at above 0.1 T are induced by $\eta(k)$, at smaller fields they are caused by $\phi(k)$. The Mathematica code to this simulation is given in the appendix in Sec. A.5. The resonance mode models the measurement (see Fig. 4.2.2a) well. The resonance magnetic fields and frequencies are well comparable. The broadening of the simulated resonance for small fields is coincident with the appearance of several resonance modes in the measurement in this field range. A detailed discussion of the comparability of the simulation and the measurement is given in the following.

In order to evaluate the simulation more precise, a slice at 24 GHz of the simulated resonance and the measured spin wave resonance is depicted in Fig. 4.2.6b. The grey shaded field range marks the visible most pronounced resonances in the respective frequency-field-plots. The height of the peak does not provide any information as the units of the susceptibility or S-parameter are not correlated. Nevertheless, the field of the peaks and their width can be compared. The simulation shows a clear peak and dip in the resonance for increasing fields between approximately 0.25 T and 0.35 T. The measurement includes field dependent background noise which hinders a clear distinguishing of the resonance.
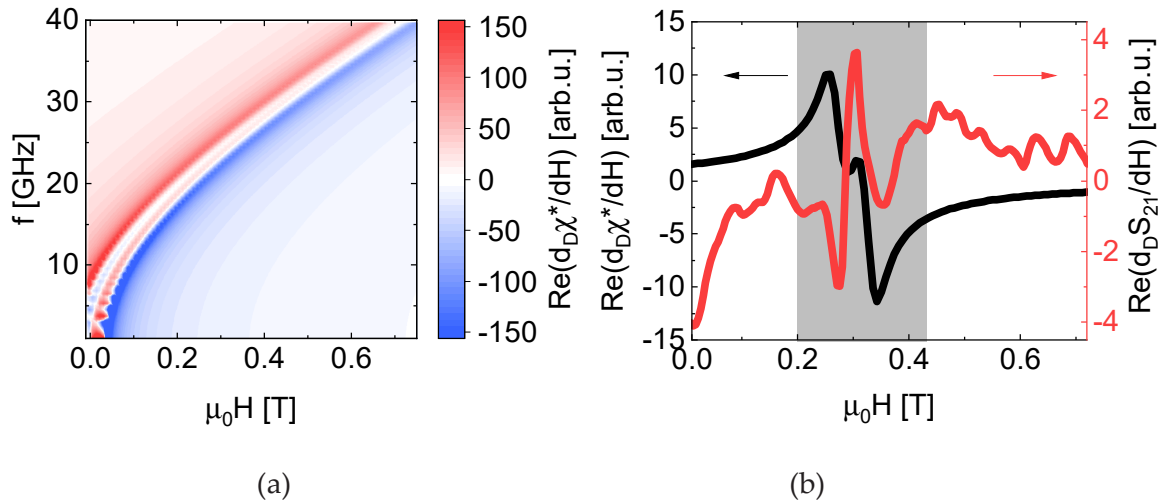
Figure 4.2.6.: Final simulation of the resonance mode in DE geometry and comparison (a) Simulation of the resonance mode in DE geometry including the antenna efficiency and a phase delay. The weighted susceptibility is background corrected and the real part is shown. (b) Comparison at $24\,\mathrm{GHz}$ between the simulated resonance (black) and the measured resonance (red).

It is approximately in the same field range as the simulation. The broadening provides information about the damping present in the hybrid ML system and thus is estimated correctly in the simulation. The inverted behavior of dip and peak in the measurement is attributed to the internal complex evaluation of the VNA compared to the straight forward data processing of the simulation data. The oscillations induced by $\eta(k)$ and $\phi(k)$ are a preliminary possibility to reproduce the not straight behavior of the measured resonance. Additionally, the measurement might include not only one resonance but can have several resonances overlying. Especially in the field range of $0.35\,\mathrm{T}$ to $0.45\,\mathrm{T}$ there might be a second resonance which overlaps with the main resonance.

In summary, the model of the DE resonance represents the actual measurement well. Additionally it reinforces the assumption taken in the analysis of the FMR that in IP field configuration the ML resonance is suppressed and the hybrid ML can be modeled as CoFe layer of a $20\,\mathrm{nm}$ thickness.

4.2.3. Comparison FMR and Spin Wave Resonance

If we compare the linewidth of the FMR mode and spin wave mode, we can compare the effect of damping in the two systems. The linewidth of the spin wave resonance depending on the frequency is taken by Lorentz fitting and extracting the FWHM field value. It is depicted in Fig. 4.2.7.

Two regions can be identified, the first up to $15\,\mathrm{GHz}$ and the second above $20\,\mathrm{GHz}$. This classification is simply due to the lacking visibility of the spin wave resonance mode in Fig. 4.2.2a in the intermediate frequency range and thus the FMR linewidth is also not depicted
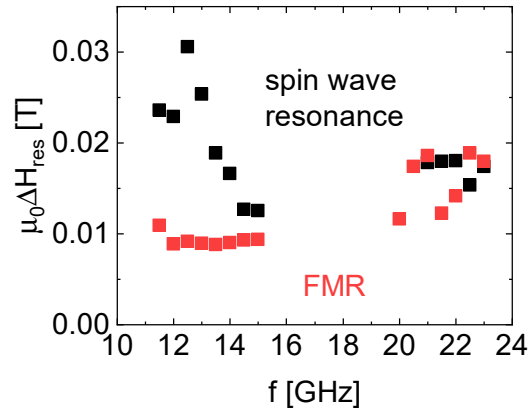
Figure 4.2.7.: Linewidth of the spin wave resonance and FMR.

in this regime. The extraction of precise linewidth values has to be handled with care as either several resonances are coincident or the present resonance smears out. Nevertheless, a trend is visible. For small frequencies, the linewidth of the spin wave in Fig. 4.2.2a exceeds the one of the FMR in Fig. 4.2.1a and for high frequencies the values of the linewidth are approaching each other. The linewidth of the spin wave resonances is expected to be wave vector dependent (see Eq. 4.20). Therefore, a difference in the linewidth of FMR and spin wave resonance is anticipated. Conclusively, for small frequencies, this means the damping for traveling spin waves can be comparable to zero wave vector resonances and the difference in the linewidths is still explainable. As the same material is investigated for spin waves and FMR, the same damping effects are likely to have an effect. Additionally, as slightly visible in Fig. 4.2.2, for small frequencies several spin wave resonances are visible. This can explain the broader linewidth due to overlapping resonances and shows the propagation of several spin waves. Their frequency is fixed by the microwave source, namely the VNA, but several spin waves with differing wave vectors can superimpose. For high frequencies, this effect is suppressed, thus only one most pronounced spin wave resonance is visible, revealing the same damping as in the FMR mode.

4.3. Spin Waves in Out-of-plane Magnetized Magnetic Multilayers

Apart from investigations in IP configuration, the hybrid ML Ta(1.5)/Pt(4)/Cu(2)/[Pt(0.5)/CoFe(1.17)/Ir(0.7)]$_6$/Ru(5)/CoFe(20)/Ru(2)/Ta(2) is also investigated in OOP. The FMR in Sec. 4.3.1 allows to receive deeper insight in the magnetic properties of the hybrid ML and is compared to the results obtained in IP configuration. The propagating spin wave resonance is characterized as FV mode in Sec. 4.3.2.

4.3.1. Ferromagnetic Resonance

In similar fashion to the IP analysis, the FMR signal of the hybrid ML in OOP configuration in Fig. 4.3.1a can be analyzed.
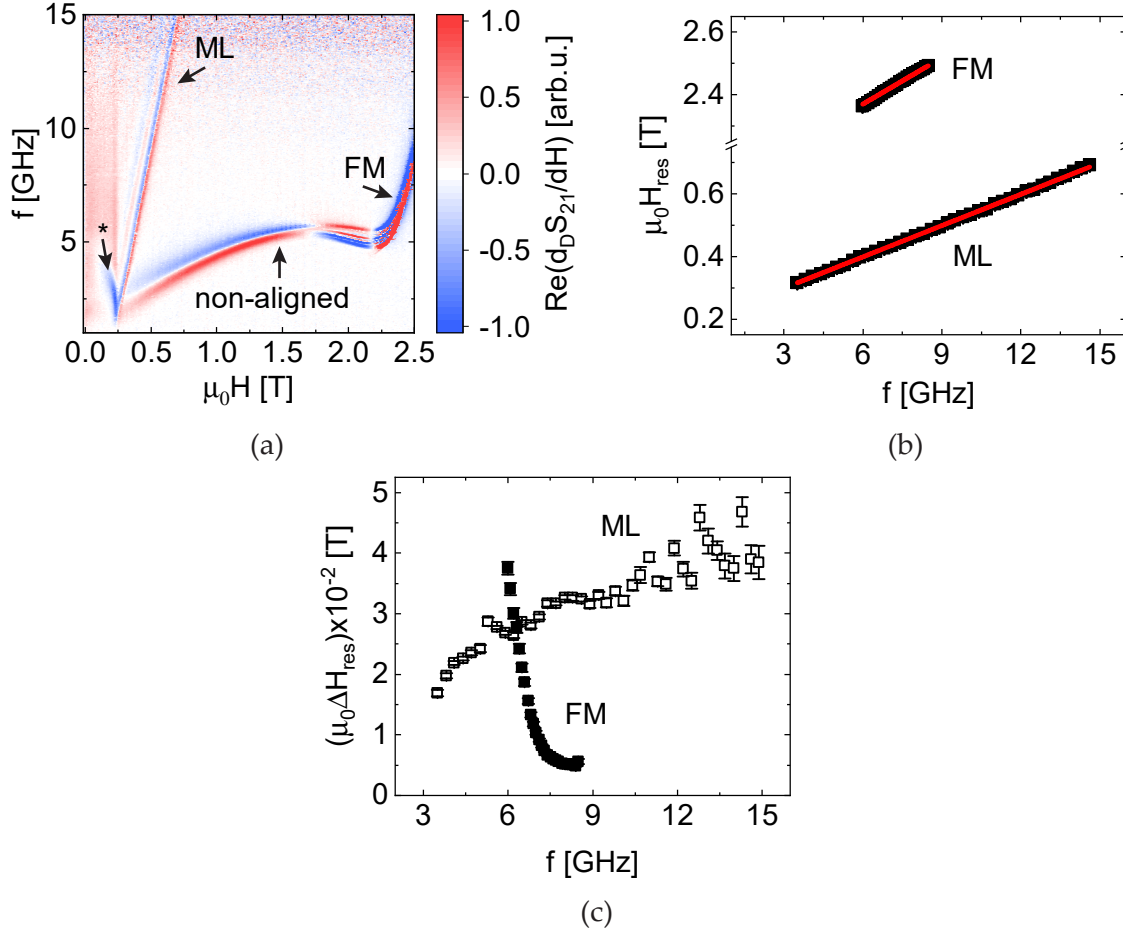

Figure 4.3.1.: OOP FMR (a) Real part of background corrected measured OOP FMR. The respective resonance modes are labeled. (b) The ML and FM FMR mode is fitted by the Kittel equation. The error bars are smaller than the symbol size. (c) The linewidth of the ML and FM resonance.

The OOP resonances show both, the ML mode at fields from $0.2\,\text{T}$ to $0.8\,\text{T}$ over all depicted frequencies and the FM mode at field magnitudes above $2.2\,\text{T}$. Both can be very well described by the OOP Kittel Eq. (4.14) as linear dependence of the resonance frequency on the field and with its slope determined by g. The part of the FM mode at fields around $2.2\,\text{T}$ shows no perfect linear relation between frequency and field. We assume here, the magnetization does not follow perfectly the external field and exclude the appearing of domain formation. The magnetic field of $2.2\,\text{T}$ also coincides with the beginning of the saturation of the FM, thus allowing a not perfect alignment until the field increases. If the FM would decay into domains, presumably there would be no ferromagnetic resonance visible, as the resonance oscillations cancel each other out. The mode reaching from $0.3\,\text{T}$

to $2.2\,\mathrm{T}$ at frequencies smaller than $6\,\mathrm{GHz}$ is called non-aligned mode and would meet with the FM mode at zero frequency ideally. This deviation is explainable with a not perfect alignment of the thin film sample in OOP orientation. This mode only appears in OOP configuration below a certain magnetic field where the magnetization is no longer aligned with the external field [99, 100]. The small most left mode (labeled as "*" in Fig. 4.3.1a) below $0.2\,\mathrm{T}$ is a hint for skyrmion formation. It is addressed as dynamic precession of the magnetic moments in the quasi-uniform background with existing skyrmions in it [31]. The saturation magnetization once again allows to explain the field position of resonances at zero frequency. The ML with a saturation magnetization of approximately $0.2\,\mathrm{T}$ and the FM with $2.2\,\mathrm{T}$ are well separated modes, which is in contrast to the IP measurement. The visibility of the ML mode (weather to measure in IP or OOP) can be understood by enhanced two-magnon damping effects appearing in the ML in IP. Therefore, the ML is broadened to such an extent that it is no longer visible. In OOP, the two-magnon scattering is suppressed, resulting in the visibility of the ML resonance.

A qualitative analysis of the resonances is done in the following. The linear correlation between resonance field and frequency is described by Eq. (4.14) and is visible in the left small-field ML mode and slightly in the most right FM mode starting above $2.2\,\mathrm{T}$. The slope of each mode is once again determined by the Landé-factor. The room-temperature measurements are conducted at such high magnetic fields trying to achieve a full alignment of the magnetization to the externally applied field and thus an application of the Kittel formalism. By help of this Kittel Eq. (4.14) applied on the FMR modes (see Fig. 4.3.1b) the effective magnetization and the Landé-factor can be extracted. For the FM resonance mode, we obtain values of $\mu_0 M_{\mathrm{eff}} = 2.073 \pm 0.004\,\mathrm{T}$ and $g = 1.442 \pm 0.013$. The effective magnetization is close to the one of other hybrid MLs [31], a g-factor smaller than 2 is unphysical. Both parameters have to be treated with care as the frequency range, in which the FM mode exists, is small. It is cut off due to the limited maximally applicable field of the electromagnet and the Kittel fit is only reasonable in the region of the linear relation between resonance field and frequency. Especially the Landé-factor which represents the slope of the mode is heavily affected by the small amount of sample points. Additionally, the maximal applied field might not have saturated the FM completely and a perfect alignment of the sample in OOP is also not assured. Therefore, we use the effective magnetization and Landé-factor extracted from the IP Kittel fit application. The values also describe well the FM resonance in OOP configuration. As in IP the FM mode prevails, the extracted reasonable $\mu_0 M_{\mathrm{eff}}$ and g can be also used in the OOP measurement. The Landé-factor of the ML mode is well comparable to other MLs with 6 repetitions of the trilayer and the effective magnetization is near the expected value ($g = 2.140 \pm 0.006$ and $\mu_0 M_{\mathrm{eff}} = 0.199 \pm 0.001\,\mathrm{T}$) [31]. The deviation can be a hint for the influence of the FM onto the ML. Analyzing the magnetic field resonance linewidth of both modes (see Fig. 4.3.1c) shows a very small linewidth for the ML in the order of $10\,\mathrm{mT}$ and for the FM of down to $1\,\mathrm{mT}$. This let us assume a small damping and low inhomogeneity amount in the thin film.

Especially, the FM linewidth in OOP is smaller compared to IP. A reason is the suppressed two-magnon scattering in OOP, which is the reason for the enhanced damping in IP.

4.3.2. Spin Wave Propagation

In OOP configuration, spin waves propagating in the film plane excite FV resonances. They are present in our hybrid ML at field magnitudes above $2.2\,\mathrm{T}$ and small frequencies. Its background corrected real part is depicted in Fig. 4.3.2 and cut off at high fields and frequencies above $16\,\mathrm{GHz}$ due to a limited magnetic field of the measurement setup. Below $2.2\,\mathrm{T}$, the mode disappears which is confirmed by applying another background correction method. This divide slice technique avoids the canceling out of signal that is constant in frequency. Several resonances are pronounced and the strongest is visible at highest fields. All modes reveal a small linewidth and further analysis is done by extracting the resonance field. No modes are visible at smaller field. Because the FV mode is observed at magnetic fields that exceed the expected field range for skyrmion formation in the ML (max. $200\,\mathrm{mT}$, see [69]), we do not expect to observe any impact of skyrmion formation on spin wave propagation in the investigated range of magnetic fields.
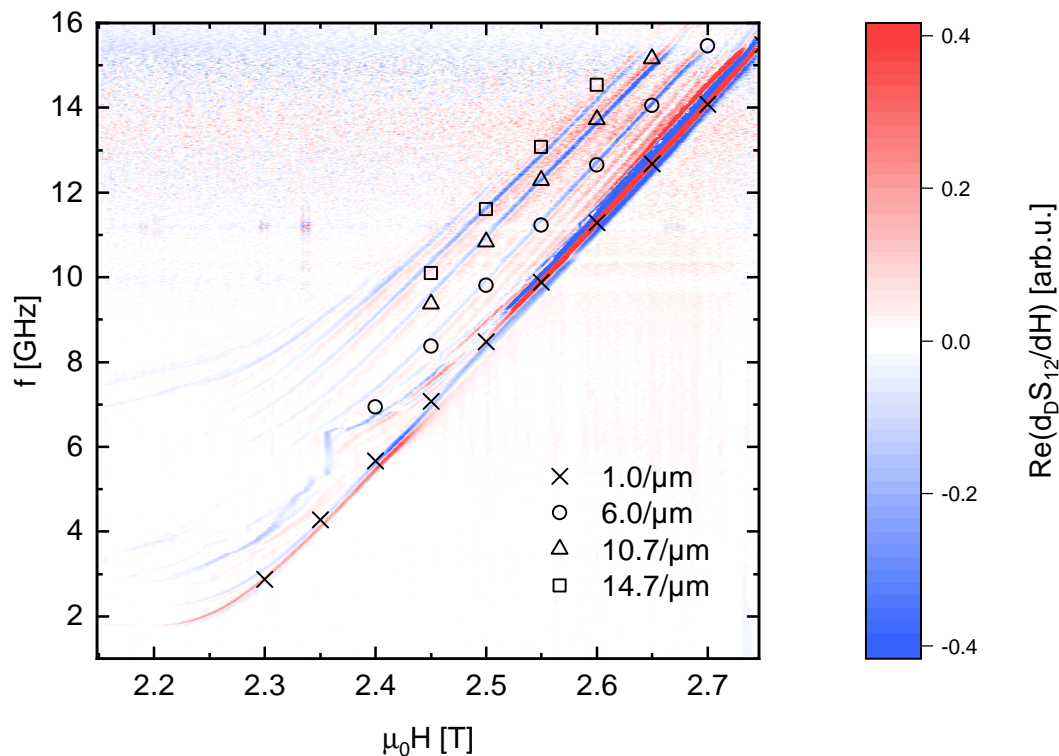

Figure 4.3.2.: Real part of measured OOP spin wave resonance with background correction. The symbols show the fit by Kalinikos-Slavin for the respective wave vector.

The analysis of the spin wave resonance frequency with respect to the field in Fig. 4.3.3a is done by use of the Kalinikos-Slavin equation. The Eq. (4.19) is adapted to the FV geometry and simplified [38]

$$\omega_{\mathrm{k}} = \gamma\mu_0 \sqrt{H_0 - M_{\mathrm{s}}\left(H_0 - M_{\mathrm{s}}\left(1 - \frac{1 - e^{-kd}}{kd}\right)\right)}. \tag{4.27}$$

In order to explain the quantity of the resonances, we use the antenna excitation efficiency in Fig. 4.2.5a. $\eta(k)$ predicts several wave vectors at which an increased efficiency is present. In Fig. 4.3.2, four most pronounced resonances are fitted by Eq. (4.27). The most pronounced resonance at a wave vector of approximately $1\,\mu\mathrm{m}$ is also the global maximum of $\eta(k)$. The local maxima in $\eta(k)$ above $1\,\mu\mathrm{m}$ are of smaller excitation efficiency compared to the first one and of broader linewidth. Three of them can be reproduced by the visible spin wave resonances, the remaining three maxima are either close to other maxima or rather broad. This might result in the less visibility of their respective spin wave resonance. Overall, the quantity and wave vectors of the spin wave resonances extracted by Eq. (4.27) are well explained by the excitation efficiency of the antenna $\eta(k)$.

To extract magnetic parameters in detail, the most pronounced resonance modes in Fig. 4.3.2 is analyzed. The resonance field with the largest amplitude of the magnitude of the transmission is extracted and fitted by the Kalinikos-Slavin Eq. 4.27. The saturation magnetization is once again adapted for anisotropies by introducing an effective magnetization $\mu_0 M_{\mathrm{eff}} = 2.070 \pm 0.001\,\mathrm{T}$ and we use the theoretically predicted and in IP approved dominantly excited wave vector k. The fit in Fig. 4.3.3a is only reasonable by using the Landé-factor obtained by the FMR in IP, not the value obtained by the Kittel fit of the FM mode in OOP. The effective magnetization is reproducible by both, the FMR and spin wave resonance. The resulting analysis is depicted in Fig. 4.3.3a. The linewidth of the spin wave resonances of a few mT are displayed in Fig. 4.3.3b to demonstrate the very sharp resonances and thus ideally the small damping. As the wave vector is not kept constant during this measurement, the linewidth does not necessarily correlate with the spin wave damping, but can simply display the change in k. Applying a fit to the resonance linewidths is not reasonable due to the small amount of data points.

Analogue to the IP measurement, the parameters show no influence of the ML but display the dominance of CoFe in the hybrid ML. In order to gain deeper insight into the magnetic parameters, especially the correct Landé-factor, a measurement up to higher field magnitudes is required which allows to measure the full resonance. As we assume no skyrmion formation in the field range of the observed FV mode, further investigations with another hybrid ML might offer to investigate spin wave resonances along with skyrmion formation. The hybrid ML should have a thinner FM layer, to increase the influence of the ML. As we assume the present FV mode to be caused by the FM, the ML resonance (intensity) might by simply suppressed. Therefore, enhancing the ML contribution might allow to also investigate the ML resonance. As seen in the OOP FMR, the ML resonances are
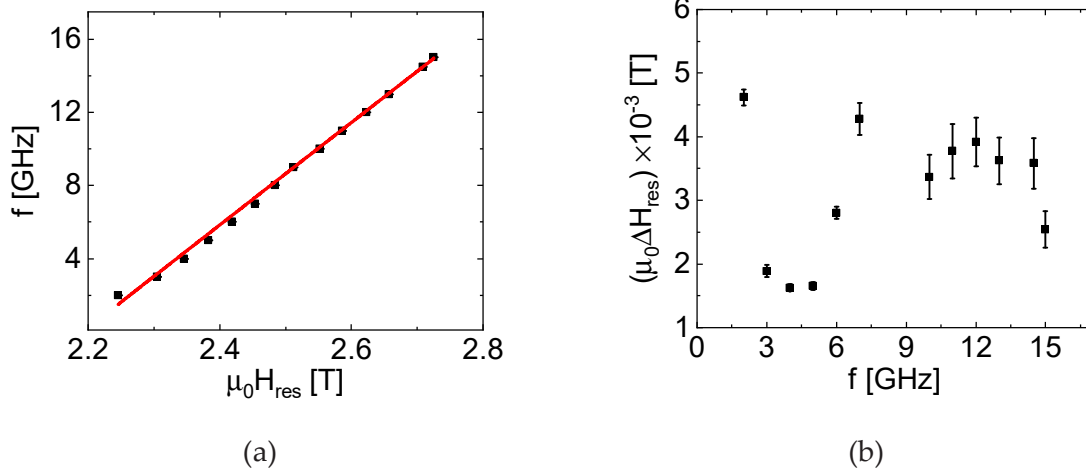
(a)   (b)

Figure 4.3.3.: Spin wave resonance analysis in OOP (a) The resonance of the spin wave is fitted by the Kalinikos-Slavin equation in FV geometry. (b) The linewidth of the FV spin wave resonance.

typically located at smaller magnetic fields than the FM. Consequently, a hybrid ML with thinner FM might show ML FV resonances at smaller fields and thus in a magnetic field region with possible skyrmion formation.

5. Summary

This thesis focuses on the investigation of hybrid multilayers and their building blocks, the ferromagnet (FM) and the multilayer (ML). The complex constitution of the heterostructures enables a variety of special electronic and magnetic characteristics, that we analyzed in the context of charge and spin wave transport. In the following, the main findings are summarized and future experiments are mentioned.

Charge Transport

The transport of charge inside a hybrid ML with a comparable thickness of ML and FM, as well as inside its single elements FM and ML, is investigated by studying magnetoresistance effects. In all three sample types, contributions of the spin Hall magnetoresistance (SMR) and the anisotropic magnetoresistance (AMR) are detected by means of measurements dependent on the orientation of the magnetic field. The assumption that these measurements in three orthogonal rotation planes are not usable to clearly separate SMR and AMR contributions are confirmed by the amplitude of the resistivity modulations. Additionally, we can solely explain the resistivity response in our hybrid ML by employing the AMR description of ferromagnetic thin film samples with a texturing in (111)-orientation and cubic crystal symmetry. The resistivity behavior of the hybrid ML and the FM can only be completely modeled by including the AMR description in textured thin films, the ML can also be described in this model. It is astonishing that also the primitive FM needs the elaborated form of the AMR, as this has not been investigated extensively so far [62]. The modeling of the resistivity response by the texture induced AMR allows to obtain ρ_i^{AMR}-parameters, describing the modulation of the resistivity depending on the direction of the applied magnetic field. Since a clear separation of the interface scattering effects and the AMR due to a (111)-texturing requires a systematic investigation of the thickness dependence of our samples, we refrain from comparing the extracted ρ_i^{AMR}-parameters for each sample. As an additional result obtained during these measurements, we determined the thin film shape anisotropy of $Co_{25}Fe_{75}$ (CoFe) to be higher than in bulk material. After having explained the magnetoresistance effects in each sample on its own, we discussed how to link the FM and ML systems to receive the resistivity response of the hybrid ML system. This was achieved by usage of a parallel resistor model and is qualitatively as well as quantitatively well in agreement with our experimental results. This finding supports the assumption that there is no static interlayer exchange coupling between ML and FM in a hybrid ML system, excluding further magnetic coupling effects.

Deeper insight into the configuration of magnetic moments inside a hybrid ML with a 20 nm thick FM layer, thus more dominant than the ML contribution, is received by conducting magnetic field magnitude resolved measurements. The magnetic moments rotate inside the film plane from an orientation parallel to the current direction and transverse to it and vice versa. Only by application of the magnetic field in an out-of-plane (OOP) direction to the film plane, the magnetic moments can be forced in OOP direction. This underlines the in-plane (IP) easy-plane anisotropy character of the hybrid ML and thus the anisotropy characteristics of the CoFe thin film. Thereby, the dominance of the FM over the ML in the hybrid system is proven. The magnetic field dependent measurement also enables an extraction of the magnetoresistance value. The values of all three sample types are rather small compared to literature [57, 62, 65, 70]. Direct relations between the magnetoresistance of a hybrid ML and its single contributions from the FM and the ML are difficult to make. This is most likely caused by the complicated influence of both SMR and AMR in our samples. However, we found comparable values in the magnetoresistance for our MLs, showing that the observations are general for our sample structures. Due to the rather small signals, a strict and explicit relation of our resistivity behavior to SMR or AMR contributions should be handled with care and we refrained from doing so in this thesis.

Spin Wave Transport

We extended our investigation of the hybrid ML to the transport of spin waves inside it. The present sample is characterized by a thick FM layer of 20 nm. We analyzed the obtained ferromagnetic resonance (FMR) and spin wave resonance spectra with respect to the external magnetic field and microwave frequency. In both measurement geometries, IP and OOP, magnetization properties can be deduced allowing to understand the relation between FM and ML in the hybrid ML. In IP orientation, the FM resonance prevails as the ML resonance is weakened due to two-magnon-scattering and thus is not resolved in the measurement. The magnetic properties as e.g. the IP easy-plane anisotropy are comparable to similar hybrid MLs except for a smaller damping [31]. The spin wave resonance in Damon-Eshbach (DE) geometry reveals a most efficiently excited wave vector consistent with the value defined via the design of the antenna. The behavior of the resonance is very well simulated by the susceptibility of a CoFe thin film being as thick as the FM in the hybrid ML. The model is further expanded by weighting the susceptibility by an antenna efficiency and an induced phase change. The simulation results are very well comparable to the measured resonance and prove the dominance of the FM over the ML in the hybrid ML. The FMR and spin wave resonance provide the parameters to calculate the spin wave propagation length. The generally small value [27] is comparable to hybrid MLs of similar constitution [31] and might be limited by scattering effects. Additionally, the spin wave resonance measurement allows to study the antenna non-reciprocal excitation efficiency. Comparing the FMR and spin wave resonance, the number of spin wave resonances exceeds the one of the FMR for small frequencies. At higher frequencies, this difference is

suppressed and the damping in both systems is comparable. The several spin waves differ by their wave vector fixed by the microwave source and can be superimposed.

In OOP configuration, the FMR of the ML and FM are visible both with small linewidths, thus allowing us to assume a small damping and low inhomogeneity amount in the thin film. The FM resonance reveals a not perfect alignment in OOP. An additional mode at small magnetic fields provides a hint for skyrmion formation. The lower intensity of the ML resonance compared to the FM resonance underlines the assumption that in IP the visible mode is dominated by the FM. The FM mode is difficult to analyze due to a small number of data points besides a potentially not fully saturated FM and a not perfectly aligned sample. Nevertheless, the FM mode can be described by the magnetic parameters extracted in the IP FMR measurement. The ML mode reveals magnetic parameters comparable to MLs of similar constitution [31]. Investigating the spin wave resonance in OOP, the forward-volume (FV) mode is well pronounced and of interestingly high quantity. Nevertheless, because the resonance is observed at magnetic fields that exceed the expected field range for skyrmion formation in the ML, we do not anticipate to observe any impact of skyrmion formation. The FV modes reveal a small linewidth and analogue to the IP measurement, the parameters show no influence of the ML, but display the dominance of the FM in the hybrid ML.

Outlook

In this thesis, we manage to investigate hybrid MLs with FMR modes giving a hint on skyrmion formation. We are also able to move the spins inside the hybrid ML by applying electrical current. This manipulation paves the way to spintronic applications as skyrmion-based memory and logic devices. The consequent next step is to apply a charge current and study the changing magnetic texture in detail. As the addressed skyrmions are of small size in our hybrid MLs, magnetic optical techniques are not usable. Alternative methods are presented in the following, allowing to create, manipulate and detect single skyrmions [19]. In that regard, a well employed method is the examination of the spin-orbit torques (SOTs). So far, SOTs are investigated in magnetic heterostructures in principle, but only in less complex ML structures with fewer repetitions or fewer heavy-metal layers compared to our samples [101, 102]. A suitable technique to characterize the SOT is a harmonic Hall voltage measurement [103] which is feasible with our already fabricated Hall bar structures. The appearing magnetization reversals due to the SOT can furthermore be investigated by magnetic force microscopy, visualizing the current-induced domain wall motion [104]. Several application-relevant aspects are already highly investigated, as a usage of current pulses to avoid thermal instability by decreasing the device size [105]. The presented measurement techniques to investigate the SOT and thus control skyrmions are inevitable to take a step closer to an implementation of hybrid MLs in applications. Nevertheless, our material system is not yet fully characterized in order to exploit its full potential.

Concerning the charge transport in hybrid MLs, we had to employ the AMR description in (111)-textured ferromagnetic thin films to understand especially the resistivity behavior of the hybrid ML. But the FM is also better described by the use of the textured AMR model than by the conventional polycristalline AMR description. So far, we expanded the textured AMR up to the fourth order, which is sufficient to describe the resistivity with suitable accuracy. Lower order fits are not adequate which is in contrast to the present literature [62]. To increase the precision, higher order terms can be included, but this enhances the complexity of the fit. The influence of higher orders on the resistivity has to be studied and a trade-off between precision and simplicity of the fit has to be found. As hardly any studies on the AMR in textured thin films exist, this topic needs further investigation. Several sample parameters can be changed to examine their influence on the magnetoresistance effect and to obtain a maximal impact, as the Co and Fe ratio in the alloy or an implementation of different FM metals. To overcome the difficulty in separating between the magnetoresistance effects, angle dependent measurements at different temperatures may help. A dominance in the conventional AMR and SMR in different temperature regimes has already been observed for other heterostructures [66] and might also allow to draw a conclusion about the special AMR appearance compared to the SMR in our hybrid MLs.

The spin wave transport in our system should receive further investigation in the OOP measurement configuration. For the present hybrid ML with a rather thick FM layer of $20\,\text{nm}$, measurements at higher magnetic field magnitudes are needed to record the complete resonance. Also, a change of the hybrid ML may be interesting. Decreasing the thickness of the FM and thus allowing to reduce its dominance, might lead to spin wave resonances induced by the ML at smaller magnetic fields. They could then be linked to skyrmion formation. Additionally, as our presented sample structure already involves dc current contacts, an investigation of propagating spin waves in this context and their dependence on dc current is feasible.

Nevertheless, our presented hybrid MLs systems are now better understandable and are definitely a promising candidate to serve as building blocks for a new generation of storage and logic devices.

A. Appendix

In the following, additional information on the theory, methods and the simulation mentioned in this thesis is given. It starts with an overview over the investigated samples in Sec. A.1 and further details on the derivation of the AMR in (111)-orientated textured thin films in Sec. A.2. Following are details on the lithography process of laser writing in Sec. A.3 and electron beam writing in Sec. A.4. The appendix is concluded with the simulation code on IP spin wave resonances in Sec. A.5.

A.1. Sample Overview

In this thesis, several different samples are investigated as hybrid MLs, MLs and FMs. Herein listed is a short description and the stack sequence of the samples.

sample type	stack sequence
ML$_1$	Ta(1.5)/Pt(4)/Cu(2)/[Pt(0.75)/CoFe(1.0)/Ir(0.45)]$_7$ /Ru(0.9)/Ta(2)
FM$_1$ (consisting of seed layer, spacer layer, FM, cap layer)	Ta(1.5)/Pt(4)/Cu(2)/Ru(0.9)/CoFe(5)/Ru(2)/Ta(2)
ML$_1$ + FM$_1$	Ta(1.5)/Pt(4)/Cu(2)/[Pt(0.75)/CoFe(1.0)/Ir(0.45)]$_7$ /Ru(0.9)/CoFe(5)/Ru(2)/Ta(2)
ML$_1$ + FM$_2$ (thicker spacer layer)	Ta(1.5)/Pt(4)/Cu(2)/[Pt(0.75)/CoFe(1.0)/Ir(0.45)]$_7$ /Ru(5)/CoFe(5)/Ru(2)/Ta(2)
ML$_2$ + FM$_3$ (different trilayer and thicker FM)	Ta(1.5)/Pt(4)/Cu(2)/[Pt(0.5)/CoFe(1.17)/Ir(0.7)]$_6$ /Ru(5)/CoFe(20)/Ru(2)/Ta(2)
ML$_3$	Ta(1.5)/Pt(4)/Cu(2)/[Pt(0.5)/CoFe(1.1)/Ir(0.45)]$_5$ /Ta(1.5)
ML$_4$	Ta(1.5)/Pt(4)/Cu(2)/[Pt(0.75)/CoFe(1.1)/Ir(0.45)]$_7$ /Ru(1.5)

Table A.1.1.: Overview of samples used in this thesis.

Samples ML$_1$, FM$_1$ and ML$_1$+FM$_1$ are analyzed in Chapter 3, ML$_2$+FM$_3$ is used in Chapters 3 and 4. The remaining two MLs ML$_3$ and ML$_4$ are shortly mentioned in Chapter 3.

A.2. AMR in (111)-Textured Thin Films

In the following, AMR behavior in thin films textured in fcc (111)-direction is explained. We start with using Ohm's law and expressing components of the electrical field strength by components of the charge density

$$E_i = \sum_{k=1}^{3} \rho_{ik} j_k \,.$$ (A.1)

The tensor ρ_{ik} relates the charge current density j_k and the corresponding electric field E_i and is called resistivity. Its components can be expressed by direction cosines β_i of the charge current density

$$\rho = \sum_{i,k=1}^{3} w_{ik} \beta_i \beta_k \,.$$ (A.2)

The prefactors w_{ik} of the now developed expression are functions of the direction cosines of the magnetization of the MO with respect to the crystallographic axes. Assuming a cubic crystal symmetry, the prefactors have to satisfy symmetry conditions with respect to the magnetization direction cosines [106][107]. Keeping this in mind, we can derive a resistivity tensor up to fourth order. The process is in more detail shown in the SI of reference [62] and summarized in the following.

In order to apply an expression for the resistivity as function of direction cosines of the magnetization to a textured polycrystalline thin film, we firstly have to transform the main textured crystal orientations into a basis frame of a single crystal. This basis frame can be defined via unit vectors spanned for a thin film textured in (111)-direction. It is a set of orthogonal vectors applied on an arbitrary oriented crystal with current applied in the (111)-plane

$$\hat{j} = \begin{pmatrix} 1/\sqrt{2} \cdot \cos\phi + 1/\sqrt{6} \cdot \sin\phi \\ -1/\sqrt{2} \cdot \cos\phi + 1/\sqrt{6} \cdot \sin\phi \\ -2/\sqrt{6} \cdot \sin\phi \end{pmatrix} \,,$$ (A.3)

$$\hat{n} = \begin{pmatrix} 1/\sqrt{3} \\ 1/\sqrt{3} \\ 1/\sqrt{3} \end{pmatrix} \,,$$ (A.4)

$$\hat{t} = \begin{pmatrix} 1/\sqrt{6} \cdot \cos\phi - 1/\sqrt{2} \cdot \sin\phi \\ 1/\sqrt{6} \cdot \cos\phi + 1/\sqrt{2} \cdot \sin\phi \\ -2/\sqrt{6} \cdot \cos\phi \end{pmatrix} \,.$$ (A.5)

Relative to the new coordinate system spanned by $\hat{j}$, $\hat{n}$ and $\hat{t}$, the magnetization direction cosines are defined:

$$m_x = m_j \cdot (1/\sqrt{2} \cdot \cos\phi + 1/\sqrt{6} \cdot \sin\phi) + m_t \cdot (1/\sqrt{6} \cdot \cos\phi - 1/\sqrt{2} \cdot \sin\phi) + m_n \cdot 1/\sqrt{3}, \quad \text{(A.6)}$$

$$m_y = m_j \cdot (-1/\sqrt{2} \cdot \cos\phi + 1/\sqrt{6} \cdot \sin\phi) + m_t \cdot (1/\sqrt{6} \cdot \cos\phi + 1/\sqrt{2} \cdot \sin\phi) + m_n \cdot 1/\sqrt{3}, \quad \text{(A.7)}$$

$$m_z = m_j \cdot (-2/\sqrt{6} \cdot \sin\phi) + m_t \cdot (-2/\sqrt{6} \cdot \cos\phi) + m_n \cdot 1/\sqrt{3}. \quad \text{(A.8)}$$

Next is to define the cubic resistivity tensor up to fourth order in magnetization in our case for ferromagnetic materials (see e.g. up to 5th order in reference [108])

$$\rho_{\text{cubic}}^{\text{4th}} = \begin{pmatrix} \rho_{11} & \rho_{12} & \rho_{13} \\ \rho_{21} & \rho_{22} & \rho_{23} \\ \rho_{31} & \rho_{32} & \rho_{33} \end{pmatrix} \quad \text{(A.9)}$$

with

$$\begin{aligned}
\rho_{11} &= A + Cc \cdot m_x^2 + F \cdot m_x^4 + G \cdot m_y^2 m_z^2, \\
\rho_{12} &= B \cdot (-m_z) + Dc \cdot m_x m_y + Ec \cdot (-m_z^3) + H \cdot m_x m_y m_z^2, \\
\rho_{13} &= B \cdot m_y + Dc \cdot m_x m_z + Ec \cdot m_y^3 + H \cdot m_x m_y^2 m_z, \\
\rho_{21} &= B \cdot m_z + Dc \cdot m_x m_y + Ec \cdot m_z^3 + H \cdot m_x m_y m_z^2, \\
\rho_{22} &= A + Cc \cdot m_y^2 + F \cdot m_y^4 + G \cdot m_x^2 m_z^2, \\
\rho_{23} &= B \cdot (-m_x) + Dc \cdot m_y m_z + Ec \cdot -m_x^3 + H \cdot m_x^2 m_y m_z, \\
\rho_{31} &= B \cdot (-m_y) + Dc \cdot m_x m_z + Ec \cdot -m_y^3 + H \cdot m_x m_y^2 m_z, \\
\rho_{32} &= B \cdot m_x + Dc \cdot m_y m_z + Ec \cdot m_x^3 + H \cdot m_x^2 m_y m_z, \\
\rho_{33} &= A + Cc \cdot m_z^2 + F \cdot m_z^4 + G \cdot m_x^2 m_y^2.
\end{aligned} \quad \text{(A.10)}$$

As the current direction varies from grain to grain in the crystal with respect to the crystallographic axes, the resistivity is not valid for the entity of the crystal so far. Averaging over all crystal orientations solves this problem. The obtained result is the longitudinal resistivity ρ_{long}. We further use the constraint $m_j^2 + m_t^2 + m_n^2 = 1$ to simplify additionally

$$\begin{aligned}
\rho_{\text{long}} &= \frac{1}{2\pi} \int_{\phi=0}^{2\pi} \left(\hat{j} \circ \rho_{\text{cubic}}^{\text{4th}} \circ \hat{j} \right) d\phi \\
&= \frac{1}{36} \Big(36A + 18Dc + 10F + G + 2H + 2 \cdot (-15Dc + 8F + 2G + H) \cdot m_n^2 \\
&\quad - (22F + G + 8H) \cdot m_n^4 - 4 \cdot (6Dc + 2F - G + H + (4 \cdot (F + G) - H) \cdot m_n^2) \cdot m_t^2 \\
&\quad - 6Cc \cdot (-3 + m_n^2 + 2m_t^2) \Big).
\end{aligned}$$

$$\text{(A.11)}$$

Equation (A.11) is further simplified by joining the prefactors of each magnetization projection

$$\rho_{\text{long}} = \rho_0 + \rho_1 m_j^2 + \rho_2 m_n^2 + \rho_3 m_n^4 + \rho_4 m_n^2 m_j^2, \quad \text{(A.12)}$$

with the coefficients

$$
\begin{aligned}
\rho_0 &= \frac{1}{36}\left(36A + 6Cc - 6Dc + 2F + 5G - 2H\right), \\
\rho_1 &= \frac{1}{9}\left(3Cc + 6Dc + 2F - G + H\right), \\
\rho_2 &= \frac{1}{18}\left(3Cc - 3Dc + 4F - 8G + 5H\right), \\
\rho_3 &= \frac{1}{12}\left(-2F + 5G - 4H\right), \\
\rho_4 &= \frac{1}{9}\left(4F + 4G - H\right).
\end{aligned}
\tag{A.13}
$$

Depending on the respective measurement geometries, these prefactors can be specified. For each geometry the vector of $\mathbf{m}$ can be expressed in terms of projections onto the coordinate system:

$$
\mathbf{m}_{\mathrm{IP}} = \begin{pmatrix} m_{\mathrm{j}} \\ m_{\mathrm{t}} \\ m_{\mathrm{n}} \end{pmatrix} = \begin{pmatrix} \cos(\alpha) \\ \sin(\alpha) \\ 0 \end{pmatrix},
\tag{A.14}
$$

$$
\mathbf{m}_{\mathrm{OOPJ}} = \begin{pmatrix} m_{\mathrm{j}} \\ m_{\mathrm{t}} \\ m_{\mathrm{n}} \end{pmatrix} = \begin{pmatrix} 0 \\ \sin(\beta) \\ \cos(\beta) \end{pmatrix},
\tag{A.15}
$$

$$
\mathbf{m}_{\mathrm{OOPT}} = \begin{pmatrix} m_{\mathrm{j}} \\ m_{\mathrm{t}} \\ m_{\mathrm{n}} \end{pmatrix} = \begin{pmatrix} \sin(\gamma) \\ 0 \\ \cos(\gamma) \end{pmatrix}.
\tag{A.16}
$$

Inserting this in Eq. (A.12) allows to define the expected expressions for each measurement geometry:

$$
\rho_{\mathrm{long}}^{\mathrm{IP}} = \rho_0 + \rho_1 \cos^2(\alpha),
\tag{A.17}
$$

$$
\rho_{\mathrm{long}}^{\mathrm{OOPJ}} = \rho_0 + \rho_2 \cos^2(\beta) + \rho_3 \cos^4(\beta),
\tag{A.18}
$$

$$
\rho_{\mathrm{long}}^{\mathrm{OOPT}} = \rho_0 + \rho_1 \sin^2(\gamma) + \rho_2 \cos^2(\gamma) + \rho_3 \cos^4(\gamma) + \rho_4 \cos^2(\gamma) \sin^2(\gamma).
\tag{A.19}
$$

A.3. Laser Lithography Parameters

Before fabricating Hall bar samples, we conducted several tests to optimize the laser lithography process. The aim was to achieve as small as possible written structures with sufficient precision in a most efficient fabrication procedure. We developed the fabrication such as the fine conducting lines of the Hall bar are of reasonable appearance. We could solve the breaking of fine structures as well as reducing the amount of impurities on the substrate. The writing process itself is improved concerning the writing precision and time. Thus, in order to fabricate Hall bars (see Sec. 2.2.1), the following steps are taken:

cleaning	- Aceton $120\,\mathrm{s}$, level 9 - Aceton $120\,\mathrm{s}$, level 9 - IPA $60\,\mathrm{s}$, level 9 - IPA $60\,\mathrm{s}$, level 9
prebake	$120\,°\mathrm{C}$, $300\,\mathrm{s}$
adhesion promoter "TI Prime"	- spin coating 4000rpm, $20\,\mathrm{s}$ - bake $120\,°\mathrm{C}$, $120\,\mathrm{s}$ - cooling with nitrogen gun
photoresist "AZ MIR 701"	- $170\,\mathrm{\mu l}$ - spin coating 6000rpm, $60\,\mathrm{s}$ - bake $90\,°\mathrm{C}$, $90\,\mathrm{s}$
laserwriter	- laser power to focus $120\,\mathrm{\mu W}$ - exposure energy $90\,\mathrm{mJ\,cm^{-2}}$ - focus offset $2\,\mathrm{V}$ - substrate height $0.514\,\mathrm{mm}$ - spot size: high resolution, attenuation: high reduction - project settings: maximal velocity $10\,\mathrm{mm\,s^{-1}}$, maximal acceleration $500\,\mathrm{mm\,s^{-2}}$, maximal jerk $5000\,\mathrm{mm\,s^{-3}}$, PWM spacing $20\,\mathrm{nm}$, blending activated, blend tolerance $0.2\,\mathrm{\mu m}$ - writing laser settings (allows for cross check of set parameters): current threshold $31\,\mathrm{mA}$, maximal power $70\,\mathrm{\mu W}$ to $150\,\mathrm{\mu W}$, maximal current $95\,\mathrm{mA}$
bake	$110\,°\mathrm{C}$, $90\,\mathrm{s}$
developer "AZ 726 MIF"	- $60\,\mathrm{s}$, constant movement - cleanse with H_2O two times
sputter deposition	
lift-off	- Aceton $70\,°\mathrm{C}$, approx. $5\,\mathrm{min}$ - blow with pipette - if needed: ultrasonic bath at max level 2 - clean with IPA

A.4. Electron Beam Lithography Parameters

For fabrication of smaller structures than needed for Hall bars, electron beam writing was used. The writing parameters are taken from already existing recipes at the institute. The following steps are needed to take for the fabrication of markers, of the hybrid ML stripe in the center and of antennas with contact pads. The final structures are presented in detail in Sec. 2.2.2.

cleaning	- Aceton $120\,\mathrm{s}$, level 9 - Aceton $120\,\mathrm{s}$, level 9 - IPA $60\,\mathrm{s}$, level 9 - IPA $60\,\mathrm{s}$, level 9
electron beam lithography resist "PMMA 33%" (AR-P 617.08)	- $30\,\mathrm{\mu l}$ - spin coating 4000rpm, $60\,\mathrm{s}$ - bake $170\,°\mathrm{C}$, $120\,\mathrm{s}$

electron beam writing	- base dose $6.5 \, \mathrm{C \, m^{-2}}$
	- beam current increases with size of structure
	- multipliers: contact pads 0.7, multilayer strip 1.0, markers and antennas 1.0
develop "AR600-56"	- $120 \, \mathrm{s}$, constant movement
	- cleaning with IPA $30 \, \mathrm{s}$
sputter deposition	
developer "AZ 726 MIF"	- $60 \, \mathrm{s}$, constant movement
	- cleanse with H_2O two times
sputter deposition	
lift-off	- Aceton $70 \, \mathrm{°C}$, approx. $15 \, \mathrm{min}$
	- blow with pipette
	- if needed: ultrasonic bath at max level 1
	- clean with IPA

A.5. In-plane Spin Wave Resonance Simulation

Herein presented is the Mathematica code of the simulation of the DE resonance mode of a $20 \, \mathrm{nm}$ thick CoFe thin film.

In-plain spin wave resonance simulation

```
ClearAll["Global`*"];
```

Introduce constants and parameters; define also dimensions of CPW antenna:

```
parameters = {μ0 → 4 π 10^-7, μB → 9.27400968 × 10^-24, ℏ → 1.05457173 × 10^-34,
    A → 20, μ0Ms → 2.1, d → 20, α → 1.4 * 10^-2, g → 2.023, ϕ → π / 2};
```

```
parametersCPW1 = {widthcc → 1.8, widthgr → 0.9, gap → 0.75};
```

A: exchange constant [$\mathrm{pJm^{-1}}$]

μ0Ms: saturation magnetization [T]

d: film thickness [nm]

α: damping parameter

g: Landé-factor

ϕ: angle between IP field and spin wave propagation direction

μ0H: externally applied magnetic field [T]

f: frequency [GHz] via $\omega = 2\pi f$

k: wave vector [$\mu \mathrm{m^{-1}}$]

widthcc, widthgr, gap [µm]

Introduce definitions:

```
γ = g μB / ℏ;
```

```
dist = widthcc / 2 + widthgr / 2 + gap;
```

Define fields in T:

```
Bxdip = μ0Ms * ((1 - e^(-k*d*10³)) / (k * d * 10³));
Bydip = μ0Ms * (1 - ((1 - e^(-k*d*10³)) / (k * d * 10³))) Sin[ϕ]²;
Bex = 2 * A * k² / (μ0Ms / μ0);
```

Invert inverted susceptibility and take first element of it:

```
Susceptibility[f_, μ0H_, k_] =
  Inverse[{{(μ0H / μ0) + (Bex / μ0) + (Bxdip / μ0) + (i * α * ω / (μ0 * γ)), -i * ω / (μ0 * γ)},
      {i * ω / (μ0 * γ), (μ0H / μ0) + (Bex / μ0) + (Bydip / μ0) + (i * α * ω / (μ0 * γ))}}][[
    1, 1]] /. {ω → 2 π * 10⁹ * f};
```

Integrate over all wave vectors:

```
IntSusceptibility[f2_, μ0H2_] := NIntegrate[Susceptibility[f2, μ0H2, k] /. parameters,
  {k, 0, 30}, MinRecursion → 8, WorkingPrecision → 10]
```

Antenna efficiency of CPW-antenna (source: L. Liensberger):

a) First, define HeavisidePi:

```
g[x_, w_] := HeavisidePi[x / w] ;
```

b) Define antenna:

```
h[x_] =
  Convolve[g[y, widthcc], DiracDelta[y - 0], y, x] + (* center conductor *)
   0.5 Convolve[g[y, widthgr], -DiracDelta[y - dist], y, x] + (* left ground plane *)
   0.5 Convolve[g[y, widthgr], -DiracDelta[y + dist], y, x] (* right ground plane *);
```

c) Fourier Transform this antenna configuration:

```
j1[x_] = h[x] /. parametersCPW1;

Antennaefficiency1[k_] = √(2 Pi) Abs[FourierTransform[j1[x], x, k]];
```

Change of propagation phase (source: Wang, Chen et al., Nano Res. 2020):

```
Phi[k_] = Sin[k * dist] /. parametersCPW1;
```

Final susceptibility as product of antenna efficiency (squared due to two antennas) and susceptibility:

```
WeightedSusceptibility[k_, f_, μ0H_] = Simplify[
   Antennaefficiency1[k] * Antennaefficiency1[k] * Susceptibility[f, μ0H, k] * Phi[k]];

WeightedSusceptibility[k, f, μ0H] /. parameters;

Int[f0_, μ0H0_] := NIntegrate[WeightedSusceptibility[k, f0, μ0H0] /. parameters,
  {k, 0, 30}, MinRecursion → 8, WorkingPrecision → 10]
```

Bibliography

[1] International Olympic Committee, *Olympic Charter: In Force As From 17 July 2020*, International Olympic Committee, Ed., Switzerland, 2020.

[2] H. Gündel, J. Glaser, and P. Angerer, *Arbeiten und gesund bleiben: K.O. durch den Job oder fit im Beruf*. Springer Berlin, 2014.

[3] C. Moreau-Luchaire *et al.*, "Additive interfacial chiral interaction in multilayers for stabilization of small individual skyrmions at room temperature", *Nature nanotechnology*, vol. 11, no. 5, pp. 444–448, 2016. DOI: `10.1038/NNANO.2015.313`.

[4] G. E. Moore, "Cramming More Components Onto Integrated Circuits", *Proceedings of the IEEE*, vol. 86, no. 1, pp. 82–85, 1998. DOI: `10.1109/JPROC.1998.658762`.

[5] M. M. Waldrop, "The chips are down for Moore's law", *Nature*, vol. 530, no. 7589, pp. 144–147, 2016. DOI: `10.1038/530144a`.

[6] Binasch, Grünberg, Saurenbach, and Zinn, "Enhanced magnetoresistance in layered magnetic structures with antiferromagnetic interlayer exchange", *Physical review. B, Condensed matter*, vol. 39, no. 7, pp. 4828–4830, 1989. DOI: `10.1103/physrevb.39.4828`.

[7] F. Hellman *et al.*, "Interface-induced phenomena in magnetism", *Reviews of Modern Physics*, vol. 89, no. 2, 2017. DOI: `10.1103/RevModPhys.89.025006`.

[8] C. Chappert, A. Fert, and F. N. van Dau, "The emergence of spin electronics in data storage", *Nature materials*, vol. 6, no. 11, pp. 813–823, 2007. DOI: `10.1038/nmat2024`.

[9] N. F. Mott, "Electrons in transition metals", *Advances in Physics*, vol. 13, no. 51, pp. 325–422, 1964. DOI: `10.1080/00018736400101041`.

[10] A. Hoffmann, "Spin Hall Effects in Metals", *IEEE Transactions on Magnetics*, vol. 49, no. 10, pp. 5172–5193, 2013. DOI: `10.1109/tmag.2013.2262947`.

[11] F. Bloch, "Zur Theorie des Ferromagnetismus", *Z. Physik (Zeitschrift f. Physik)*, vol. 61, no. 3-4, pp. 206–219, 1930. DOI: `10.1007/BF01339661`.

[12] T. Skyrme, "A unified field theory of mesons and baryons", *Nuclear Physics*, vol. 31, pp. 556–569, 1962. DOI: `10.1016/0029-5582(62)90775-7`.

[13] N. Nagaosa and Y. Tokura, "Topological properties and dynamics of magnetic skyrmions", *Nature nanotechnology*, vol. 8, no. 12, pp. 899–911, 2013. DOI: `10.1038/NNANO.2013.243`.

[14]   S. Mühlbauer *et al.*, "Skyrmion Lattice in a Chiral Magnet", *Science (New York)*, vol. 323, no. 5916, pp. 915–919, 2009. DOI: `10.1126/science.1166767`.

[15]   A. Fert, V. Cros, and J. Sampaio, "Skyrmions on the track", *Nature nanotechnology*, vol. 8, no. 3, pp. 152–156, 2013. DOI: `10.1038/nnano.2013.29`.

[16]   J. Zang, V. Cros, and A. F. Hoffmann, *Topology in magnetism*, ser. Springer series in solid-state sciences, 0171-1873. Cham, Switzerland: Springer, 2018, vol. volume 192.

[17]   D. Maccariello *et al.*, "Electrical detection of single magnetic skyrmions in metallic multilayers at room temperature", *Nature nanotechnology*, vol. 13, no. 3, pp. 233–237, 2018. DOI: `10.1038/s41565-017-0044-4`.

[18]   T. Sebastian, K. Schultheiss, B. Obry, B. Hillebrands, and H. Schultheiss, "Micro-focused Brillouin light scattering: imaging spin waves at the nanoscale", *Frontiers in Physics*, vol. 3, p. 1589, 2015. DOI: `10.3389/fphy.2015.00035`.

[19]   J. Sampaio, V. Cros, S. Rohart, A. Thiaville, and A. Fert, "Nucleation, stability and current-induced motion of isolated magnetic skyrmions in nanostructures", *Nature nanotechnology*, vol. 8, no. 11, pp. 839–844, 2013. DOI: `10.1038/NNANO.2013.210`.

[20]   R. Tomasello, E. Martinez, R. Zivieri, L. Torres, M. Carpentieri, and G. Finocchio, "A strategy for the design of skyrmion racetrack memories", *Scientific reports*, vol. 4, p. 6784, 2014. DOI: `10.1038/srep06784`.

[21]   W. Kang *et al.*, "Voltage Controlled Magnetic Skyrmion Motion for Racetrack Memory", *Scientific reports*, vol. 6, p. 23 164, 2016. DOI: `10.1038/srep23164`.

[22]   A. Fert, N. Reyren, and V. Cros, "Magnetic skyrmions: advances in physics and potential applications", *Nature Reviews Materials*, vol. 2, no. 7, 2017. DOI: `10.1038/natrevmats.2017.31`.

[23]   X. Zhang, M. Ezawa, and Y. Zhou, "Magnetic skyrmion logic gates: conversion, duplication and merging of skyrmions", *Scientific reports*, vol. 5, p. 9400, 2015. DOI: `10.1038/srep09400`.

[24]   G. Höhler *et al.*, Eds., *Magnetic Heterostructures*, ser. Springer Tracts in Modern Physics. Berlin, Heidelberg: Springer, 2008. DOI: `10.1007/978-3-540-73462-84`.

[25]   D. L. Mills and J. A. C. Bland, *Nanomagnetism: Ultrathin films, multilayers and patterned media*, ser. Contemporary concepts of condensed matter science v. 1. Amsterdam and Oxford: Elsevier, 2006.

[26]   L. Flacke, "Spin-Pumping and Spin Wave Damping in Co25Fe75 Thin-Film Heterostructures", Master's Thesis, Technische Universität München, Garching, May 2018.

[27]   L. Flacke *et al.*, "High spin-wave propagation length consistent with low damping in a metallic ferromagnet", *Applied Physics Letters*, vol. 115, no. 12, p. 122 402, 2019. DOI: `10.1063/1.5102132`.

[28] H. S. Körner *et al.*, "Magnetic damping in poly-crystalline Co25Fe75 : Ferromagnetic resonance vs. spin wave propagation experiments", *Applied Physics Letters*, vol. 111, no. 13, p. 132 406, 2017. DOI: `10.1063/1.4994137`.

[29] A. V. Svalov *et al.*, "Study of the effect of the deposition rate and seed layers on structure and magnetic properties of magnetron sputtered FeNi films", *Vacuum*, vol. 119, pp. 245–249, 2015. DOI: `10.1016/j.vacuum.2015.05.037`.

[30] A. J. Lee, A. S. Ahmed, S. Guo, B. D. Esser, D. W. McComb, and F. Yang, "Epitaxial Co50Fe50(110)/Pt(111) films on MgAl2O4(001) and its enhancement of perpendicular magnetic anisotropy", *Journal of Applied Physics*, vol. 125, no. 18, p. 183 903, 2019. DOI: `10.1063/1.5093503`.

[31] M. Yaqoob, "Magnetization Dynamics and Magnetic Skyrmions in Thin Film Multilayer and Hybrid Systems", Master's Thesis, Technische Universität München, Garching, April 2021.

[32] R. Gross, *Annual Report 2017*, Garching, 2017.

[33] MicroChemicals, "Substrate Preparation", in *Basics of Microstructuring*.

[34] MicroChemicals, "Softbake", in *Basics of Microstructuring*.

[35] MicroChemicals, "Lift-off", in *Basics of Microstructuring*.

[36] H.-G. Rhee, "Direct Laser Lithography and Its Applications", in *Lithography*, M. Wang, Ed., InTech, 2010. DOI: `10.5772/8167`.

[37] Y. Xu, D. D. Awschalom, and J. Nitta, Eds., *Handbook of Spintronics*. Dordrecht: Springer Netherlands, 2014. DOI: `10.1007/978-94-007-7604-3`.

[38] V. Vlaminck and M. Bailleul, "Spin-wave transduction at the submicrometer scale: Experiment and modeling", *Physical Review B*, vol. 81, no. 1, 2010. DOI: `10.1103/PhysRevB.81.014425`.

[39] F. L. Zeng *et al.*, "Intrinsic Mechanism for Anisotropic Magnetoresistance and Experimental Confirmation in CoxFe1-x Single-Crystal Films", *Physical review letters*, vol. 125, no. 9, pp. 1–7, 2020. DOI: `10.1103/PhysRevLett.125.097201`.

[40] W. Thomson, "XIX. On the electro-dynamic qualities of metals:—Effects of magnetization on the electric conductivity of nickel and of iron", *Proceedings of the Royal Society of London*, vol. 8, pp. 546–550, 1857. DOI: `10.1098/rspl.1856.0144`.

[41] R. Gross and A. Marx, *Festkörperphysik*, 3rd ed. De Gruyter, 2018. DOI: `10.1515/9783110559187`.

[42] M. Althammer, "Pure spin currents in magnetically ordered insulator/normal metal heterostructures", *Journal of Physics D: Applied Physics*, vol. 51, no. 31, p. 313 001, 2018. DOI: `10.1088/1361-6463/aaca89`.

[43] M. Julliere, "Tunneling between ferromagnetic films", *Physics Letters A*, vol. 54, no. 3, pp. 225–226, 1975. DOI: `10.1016/0375-9601(75)90174-7`.

[44] G. E. W. Bauer, E. Saitoh, and B. J. van Wees, "Spin caloritronics", *Nature materials*, vol. 11, no. 5, pp. 391–399, 2012. DOI: `10.1038/nmat3301`.

[45] H. Nakayama *et al.*, "Spin Hall Magnetoresistance Induced by a nonequilibrium Proximity Effect", *Physical review letters*, vol. 110, no. 20, p. 206 601, 2013. DOI: `10.1103/PhysRevLett.110.206601`.

[46] M. I. Dyakonov and V. I. Perel, "Current-induced spin orientation of electrons in semiconductors", *Physics Letters A*, vol. 35, no. 6, pp. 459–460, 1971. DOI: `10.1016/0375-9601(71)90196-4`.

[47] J. Sinova, S. O. Valenzuela, J. Wunderlich, C. H. Back, and T. Jungwirth, "Spin Hall effects", *Reviews of Modern Physics*, vol. 87, no. 4, pp. 1213–1260, 2015. DOI: `10.1103/revmodphys.87.1213`.

[48] J. Fischer, "Spin Hall magnetoresistance in antiferromagnetic NiO and alpha-Fe2O3", Master's Thesis, Technische Universität München, Garching, August 2017.

[49] S. Geprägs *et al.*, "Spin Hall magnetoresistance in antiferromagnetic insulators", *Journal of Applied Physics*, vol. 127, no. 24, p. 243 902, 2020. DOI: `10.1063/5.0009529`.

[50] M. Weiler *et al.*, "Experimental Test of the Spin Mixing Interface Conductivity Concept", *Physical review letters*, vol. 111, no. 17, p. 176 601, 2013. DOI: `10.1103/PhysRevLett.111.176601`.

[51] M. Althammer *et al.*, "Quantitative study of the spin Hall magnetoresistance in ferromagnetic insulator/normal metal hybrids", *Physical Review B*, vol. 87, no. 22, 2013. DOI: `10.1103/PhysRevB.87.224401`.

[52] W. Limmer *et al.*, "Advanced resistivity model for arbitrary magnetization orientation applied to a series of compressive- to tensile-strained (Ga,Mn)As layers", *Physical Review B*, vol. 77, no. 20, 2008. DOI: `10.1103/PhysRevB.77.205210`.

[53] Y.-T. Chen *et al.*, "Theory of spin Hall magnetoresistance", *Physical Review B*, vol. 87, no. 14, 2013. DOI: `10.1103/PhysRevB.87.144411`.

[54] J. Fischer *et al.*, "Spin Hall magnetoresistance in antiferromagnet/heavy-metal heterostructures", *Physical Review B*, vol. 97, no. 1, 2018. DOI: `10.1103/PhysRevB.97.014417`.

[55] W. Limmer *et al.*, "Angle-dependent magnetotransport in cubic and tetragonal ferromagnets: Application to (001)- and (113)A-oriented (Ga,Mn)As", *Physical Review B*, vol. 74, no. 20, 2006. DOI: `10.1103/PhysRevB.74.205205`.

[56] R. Ramos *et al.*, "Observation of the spin Seebeck effect in epitaxial Fe3O4 thin films", *Applied Physics Letters*, vol. 102, no. 7, p. 072 413, 2013. DOI: `10.1063/1.4793486`.

[57] J. Kim, P. Sheng, S. Takahashi, S. Mitani, and M. Hayashi, "Spin Hall Magnetoresistance in Metallic Bilayers", *Physical review letters*, vol. 116, no. 9, p. 097 201, 2016. DOI: `10.1103/PhysRevLett.116.097201`.

[58] R. Gross and A. Marx, "Spinelektronik: Vorlesungsskript zur Vorlesung im SS 2004", Garching, April 2004.

[59] A. P. Cracknell, "Symmetry Properties of the Transport Coefficients of Magnetic Crystals", *Physical Review B*, vol. 7, no. 5, pp. 2145–2154, 1973. DOI: `10.1103/PhysRevB.7.2145`.

[60] H. Ebert, A. Vernes, and J. Banhart, "Magnetoresistance, Anisotropic", in *Encyclopedia of Materials: Science and Technology*, Elsevier, 2001, pp. 5079–5083. DOI: `10.1016/B0-08-043152-6/00882-2`.

[61] W. H. Kleiner, "Space-Time Symmetry of Transport Coefficients", *Physical Review*, vol. 142, no. 2, pp. 318–326, 1966. DOI: `10.1103/PhysRev.142.318`.

[62] A. Philippi-Kobs, A. Farhadi, L. Matheis, D. Lott, A. Chuvilin, and H. P. Oepen, "Impact of Symmetry on Anisotropic Magnetoresistance in Textured Ferromagnetic Thin Films", *Physical review letters*, vol. 123, no. 13, p. 137 201, 2019. DOI: `10.1103/PhysRevLett.123.137201`.

[63] K. Ganzhorn *et al.*, "Spin Hall magnetoresistance in a canted ferrimagnet", *Physical Review B*, vol. 94, no. 9, 2016. DOI: `10.1103/PhysRevB.94.094401`.

[64] S. Banerjee, J. Rowland, O. Erten, and M. Randeria, "Enhanced Stability of Skyrmions in Two-Dimensional Chiral Magnets with Rashba Spin-Orbit Coupling", *Physical Review X*, vol. 4, no. 3, 2014. DOI: `10.1103/PhysRevX.4.031045`.

[65] A. Kobs and H. P. Oepen, "Disentangling interface and bulk contributions to the anisotropic magnetoresistance in Pt/Co/Pt sandwiches", *Physical Review B*, vol. 93, no. 1, 2016. DOI: `10.1103/PhysRevB.93.014426`.

[66] S. Geprägs *et al.*, "Static magnetic proximity effects and spin Hall magnetoresistance in Pt/Y3Fe5O12 and inverted Y3Fe5O12/Pt bilayers", *Physical Review B*, vol. 102, no. 21, 2020. DOI: `10.1103/PhysRevB.102.214438`.

[67] S. Meyer, M. Althammer, S. Geprägs, M. Opel, R. Gross, and S. T. B. Goennenwein, "Temperature dependent spin transport properties of platinum inferred from spin Hall magnetoresistance measurements", *Applied Physics Letters*, vol. 104, no. 24, p. 242 411, 2014. DOI: `10.1063/1.4885086`.

[68] M. Opel, "Vorlesungsskript Magnetismus: 6. Die Austauschwechselwirkung", Garching, 2004/2005.

[69] L. Flacke *et al.*, *Robust formation of nanoscale magnetic skyrmions in easy-plane thin film multilayers with low damping*.

[70] M. Li *et al.*, "Effect of a CoFeB layer on the anisotropic magnetoresistance of Ta/CoFeB/MgO/NiFe/MgO/CoFeB/Ta films", *Journal of Magnetism and Magnetic Materials*, vol. 439, pp. 17–21, 2017. DOI: `10.1016/j.jmmm.2017.04.079`.

[71] J. M. D. Coey, *Magnetism and magnetic materials*. Cambridge and New York: Cambridge University Press, 2009.

[72] L. Landau and E. Lifshits, "On the Theory of the Dispersion of Magnetic Permeability in Ferromagnetic Bodies: reprinted from Phys. Zeitsch. der Sow. 8, pp. 153-169 (1935)", *Ukr. J. Phys.*, vol. 53, pp. 14–22, 2008.

[73] C. Lüthi, "Coupled Magnetization Dynamics in Ferrimagnet/Ferromagnet and Chiral Magnet/Ferromagnet Heterostructures", Master's thesis, Technische Universität München, Garching, June 2020.

[74] T. L. Gilbert, "Classics in Magnetics: A Phenomenological Theory of Damping in Ferromagnetic Materials", *IEEE Transactions on Magnetics*, vol. 40, no. 6, pp. 3443–3449, 2004. DOI: `10.1109/TMAG.2004.836740`.

[75] C. Kittel, "On the Theory of Ferromagnetic Resonance Absorption", *Physical Review*, vol. 73, no. 2, pp. 155–161, 1948.

[76] J. A. Osborn, "Demagnetizing Factors of the General Ellipsoid", *Physical Review*, vol. 67, no. 11-12, pp. 351–357, 1945. DOI: `10.1103/PhysRev.67.351`.

[77] D. Polder, "On the theory of ferromagnetic resonance", *The London, Edinburgh, and Dublin Philosophical Magazine and Journal of Science*, vol. 40, no. 300, pp. 99–115, 1949. DOI: `10.1080/14786444908561215`.

[78] M. Weiler, "Magnetization Dynamics and Spin Torques in Exchange-Coupled Spin Systems", Habilitationsschrift, Technische Universität München, Garching, December 2019.

[79] J. M. Shaw *et al.*, "Perpendicular Magnetic Anisotropy and Easy Cone State in Ta/Co60Fe20B20/MgO", *IEEE Magnetics Letters*, vol. 6, pp. 1–4, 2015. DOI: `10.1109/LMAG.2015.2438773`.

[80] H. Schultheiß, "Kohärenz und Dämpfungsverhalten von Spinwellen in magnetischen Mikrostrukturen", Dissertations Schrift, Technische Universität Kaiserslautern, Kaiserslautern, June 2010.

[81] H. T. Nembach, J. M. Shaw, C. T. Boone, and T. J. Silva, "Mode- and Size-Dependent Landau-Lifshitz Damping in Magnetic Nanostructures: Evidence for Nonlocal Damping", *Physical review letters*, vol. 110, no. 11, p. 117 201, 2013. DOI: `10.1103/PhysRevLett.110.117201`.

[82] H. T. Nembach, J. M. Shaw, M. Weiler, E. Jué, and T. J. Silva, "Linear relation between Heisenberg exchange and interfacial Dzyaloshinskii–Moriya interaction in metal films", *Nature Physics*, vol. 11, no. 10, pp. 825–829, 2015. DOI: `10.1038/NPHYS3418`.

[83] Marco Madami, *Dynamical Properties*, 4/20/2016.

[84] R. W. Damon and H. van de Vaart, "Propagation of Magnetostatic Spin Waves at Microwave Frequencies in a Normally–Magnetized Disk", *Journal of Applied Physics*, vol. 36, no. 11, pp. 3453–3459, 1965. DOI: 10.1063/1.1703018.

[85] R. W. Damon and J. R. Eshbach, "Magnetostatic Modes of a Ferromagnet Slab", *J. Phys. Chem. Solids*, no. 19, pp. 308–320, 1961.

[86] B. A. Kalinikos and A. N. Slavin, "Theory of dipole-exchange spin wave spectrum for ferromagnetic films with mixed exchange boundary conditions", *Journal of Physics C: Solid State Physics*, no. 19, pp. 7013–7033, 1986.

[87] J. Stigloher *et al.*, "Snell's Law for Spin Waves", *Physical review letters*, vol. 117, no. 3, p. 037 204, 2016. DOI: 10.1103/PhysRevLett.117.037204.

[88] A. Golovin, "All-Electrical Spin Wave Spectroscopy", Bachelor's Thesis, Technische Universität München, Garching, July 2019.

[89] L. Liensberger, "Spin-Orbit Torques and Magnetization Dynamics in Non-collinear Magnets", Master's Thesis, Technische Universität München, Garching, October 2017.

[90] H. Maier-Flaig *et al.*, "Note: Derivative divide, a method for the analysis of broadband ferromagnetic resonance in the frequency domain", *Review of scientific instruments*, vol. 89, no. 7, p. 076 101, 2018. DOI: 10.1063/1.5045135.

[91] R. D. McMichael, D. J. Twisselmann, and A. Kunz, "Localized Ferromagnetic Resonance in Inhomogeneous Thin Films", *Physical review letters*, vol. 90, no. 22, p. 227 601, 2003. DOI: 10.1103/PhysRevLett.90.227601.

[92] L. Liensberger, L. Flacke, D. Rogerson, M. Althammer, R. Gross, and M. Weiler, "Spin-Wave Propagation in Metallic Co25Fe75 Films Determined by Microfocused Frequency-Resolved Magneto-Optic Kerr Effect", *IEEE Magnetics Letters*, vol. 10, pp. 1–5, 2019. DOI: 10.1109/LMAG.2019.2918755.

[93] Z. Duan, I. N. Krivorotov, R. E. Arias, N. Reckers, S. Stienen, and J. Lindner, "Spin wave eigenmodes in transversely magnetized thin film ferromagnetic wires", *Physical Review B*, vol. 92, no. 10, 2015. DOI: 10.1103/PhysRevB.92.104424.

[94] M. Nakayama, K. Yamanoi, S. Kasai, S. Mitani, and T. Manago, "Thickness dependence of spin wave nonreciprocity in permalloy film", *Japanese Journal of Applied Physics*, vol. 54, no. 8, p. 083 002, 2015. DOI: 10.7567/JJAP.54.083002.

[95] O. Karlqvist, "Calculation of the magnetic field in the ferromagnetic layer of a magnetic drum", *Tekn. Hogskol. Handl.*, vol. 86, no. 27, 1954.

[96] T. J. Silva, C. S. Lee, T. M. Crawford, and C. T. Rogers, "Inductive measurement of ultrafast magnetization dynamics in thin-film Permalloy", *Journal of Applied Physics*, vol. 85, no. 11, pp. 7849–7862, 1999. DOI: 10.1063/1.370596.

[97] D. Rogerson, "Spinwellenpropagation in Kobalt-Eisen-Dünnschichtfilmen", Bachelor's Thesis, Technische Universität München, Garching, September 2018.

[98] H. Wang *et al.*, "Nonreciprocal coherent coupling of nanomagnets by exchange spin waves", *Nano Research*, 2020. DOI: `10.1007/s12274-020-3251-5`.

[99] C. He *et al.*, "Spin-torque ferromagnetic resonance measurements utilizing spin Hall magnetoresistance in W/Co40Fe40B20/MgO structures", *Applied Physics Letters*, vol. 109, no. 20, p. 202 404, 2016. DOI: `10.1063/1.4967843`.

[100] I. Barsukov *et al.*, "Field-dependent perpendicular magnetic anisotropy in CoFeB thin films", *Applied Physics Letters*, vol. 105, no. 15, p. 152 403, 2014. DOI: `10.1063/1.4897939`.

[101] J. Yu *et al.*, "Spin orbit torques and Dzyaloshinskii-Moriya interaction in dual-interfaced Co-Ni multilayers", *Scientific reports*, vol. 6, p. 32 629, 2016. DOI: `10.1038/srep32629`.

[102] K.-F. Huang, D.-S. Wang, H.-H. Lin, and C.-H. Lai, "Engineering spin-orbit torque in Co/Pt multilayers with perpendicular magnetic anisotropy", *Applied Physics Letters*, vol. 107, no. 23, p. 232 407, 2015. DOI: `10.1063/1.4937443`.

[103] M. Hayashi, J. Kim, M. Yamanouchi, and H. Ohno, "Quantitative characterization of the spin-orbit torque using harmonic Hall voltage measurements", *Physical Review B*, vol. 89, no. 14, 2014. DOI: `10.1103/PhysRevB.89.144425`.

[104] L. Caretta *et al.*, "Fast current-driven domain walls and small skyrmions in a compensated ferrimagnet", *Nature nanotechnology*, vol. 13, no. 12, pp. 1154–1160, 2018. DOI: `10.1038/s41565-018-0255-3`.

[105] M.-H. Tsai, P.-H. Lin, K.-F. Huang, H.-H. Lin, and C.-H. Lai, *Spin-orbit-torque MRAM: from uniaxial to unidirectional switching*.

[106] W. Döring, "Die Abhängigkeit des Widerstandes von Nickelkristallen von der Richtung der spontanen Magnetisierung", *Annalen der Physik*, vol. 424, no. 3, pp. 259–276, 1938. DOI: `10.1002/andp.19384240306`.

[107] R. R. Birss, *Symmetry and magnetism*, 2. ed., ser. Series of monographs on selected topics in solid state physics. Amsterdam: North-Holland Publ., 1966, vol. 3.

[108] T. McGuire and R. Potter, "Anisotropic Magnetoresistance in Ferromagnetic 3d Alloys", *IEEE Transactions on Magnetics*, vol. 11, no. 4, pp. 1018–1038, 1975. DOI: `10.1109/TMAG.1975.1058782`.

Acknowledgments

Without the help of numerous people, the time and working at the WMI would have not been that joyful. Therefore, I want to thank:

Prof. Dr. Rudolf Gross for giving me the opportunity to complete my Master's thesis at the WMI and the pleasant mentor talk.

Dr. Matthias Althammer as one of my two supervisors for offering me this thesis. Thank you for the permanent help with theory, the constant help with the fabrication in numerous labs and the insightful data discussions. Thank you for your time in extended meetings, answering questions at any time and motivating in the weekly meetings. I would also like to thank you for the proof-reading of this thesis and for the always open door.

Prof. Dr. Mathias Weiler as my second supervisor for also offering me this thesis. Thank you for the permanent support in understanding the theory behind the experiments, the enlightening data discussions and the patient help with the simulation. Thank you for always being interested in all of my measurement results, for raising up new questions in the weekly meetings and for the proof-reading of this thesis. Of course, I would like to thank you for the always open virtual door.

My advisor Luis Flacke for being the best, constant help I could have wished for during this year. You not only patiently answered all my questions at every time, but you also gave me valuable advice in the lab, endlessly assisted with data processing, repeatedly gave IT support and on top of that polished up the lunches with funny conversations. It was a pleasure to spend time with you.

PD Dr. Hans Hübl, Dr. Stephan Geprägs and Dr. Matthias Opel for their valuable scientific input whenever needed and for showing interest in my work.

Janine Gückelhorn, Lukas Liensberger and Manuel Müller for help in several labs whenever the fabrication or measurement situation seemed to be no longer salvageable.

All master students at the WMI, especially Korbinian Rubenbauer, Philipp Krüger, Monika Scheufele, Ramona Stumberger and Christopher Waas. You created a working atmosphere to share questions, frustration and chocolate (ordering is intentional). Thank you for always making me laugh.

The whole staff at the WMI for creating this friendly and productive atmosphere.

Last, but not least, my family for your constant support and interest in my studies.